A LOW-COST MPPT MULTIPLE-INPUT POWER CONVERTER FOR HOME APPLICATIONS IN ISOLATED AREAS

A THESIS SUBMITTED IN PARTIAL FULFILMENT OF THE REQUIREMENTS

FOR THE DEGREE OF MASTER OF ENGINEERING (ELECTRICAL AND ELECTRONIC ENGINEERING) AT THE
UNIVERSITY OF CANTERBURY

BY PHU HUU PHAN

UNIVERSITY OF CANTERBURY

2017

ABSTRACT

The focus of this research is to design and build a low-cost maximum power point tracking (MPPT) multiple-input-single-output power converter system for low power grid-isolated applications. The design of this power converter concentrated on searching for a suitable topology that integrates multiple renewable power sources, each with their own MPPT requirements and with the lowest cost of components. With good power conversion efficiency, the converter provides power to a dc load output and is also able to appropriately charge an energy storage battery. In addition to the main functional blocks, all protections required are equipped with the converter, including under voltage lock-out (UVLO), over voltage protection (OVP), cycle-by-cycle current limit, and battery over charge and over discharge prevention.

The development and implementation of the converter was divided by different steps. The initial phase searched for, analyzed, and proposed the most suitable topology in terms of power delivery, cost, and feasibility. The non-isolated full-bridge was chosen for the power conversion topology for each channel with its own analogue controller. An interfacing circuit was designed to work with those full-bridge controllers for integrating MPPT control signals, constant output voltage control signals, and constant charging current control signals, from a microcontroller, a single output voltage feedback loop, and a single output current feedback loop, respectively. After a specification of the design had been selected, the detailed design and calculation of circuits was carried out. Simulations were also conducted to confirm the operation of the converter, including the start-up sequences, output load response, battery charging modes, and the transient between operation modes. The converter was then transferred to PCB design with two versions, a 2-layer and 4-layer board. A comparison was made for choosing the appropriate option among the designs regarding board size, cost, and performance. The final physical converter was formed by soldering components on the manufactured 170mm x 130mm 4-layer PCB, and programming of the microprocessor. The final step was the characterisation of the converter with standard power supplies and renewable energy source emulators, in the laboratory environment.

Results show that the converter functions as per the design specifications. With the input source of a solar photovoltaic panel, a micro wind/hydro turbine, or both, the converter can work with solely a dc load or with a dc-bus connected battery (where the converter provides a three-stage charging profile). The smooth and fast transiting between operation modes of MPPT, constant output voltage, and constant charging current were recorded without any abnormal behavior. The MPPT functions separately with each input source with high accuracy and fast response to the input conditions. Depending on the state of the output, the converter automatically switches to either constant output voltage or constant charging current mode when the total available input power is higher than the output load demand. For each of these operation modes, the converter also achieves a fast response to the input sources voltage and output load variations.

With a designed capability of 2 kW maximum total power conversion, the converter is able to work with a wide range of input voltage (from 16 V to 60 V) for both input sources while its nominal output voltage is set at around 27 V for working with a nominal 24 V lead-acid battery. The peak power conversion efficiency of 95.3 % was recorded at 400 W of total input power when the turbine source voltage was 54 V (dc value after the rectifier) and the solar photovoltaic source voltage was 24 V. The operating temperature of the converter appeared to be higher than expected at some components, with a peak of 68.3 °C recorded on the gate driver chips. However, this issue could be mitigated by adding more heat sink components or modifying the design on a new revision.

With under $60 USD of total component cost (slightly above $55 for pre-manufactured components and materials, and about $3 for the PCB), the converter is shown to be a low-cost converter regarding its power capability while supporting multiple input sources which may have a wide range of nominal power outputs. This makes the converter more applicable in isolated areas of developing countries.

TABLE OF CONTENTS

ACKNOWLEDGMENTS

I wish to acknowledge my gratitude to all those who helped and supported me in this thesis. First and foremost, I would like to thank Assoc. Prof. Paul Gaynor and Dr Alan Wood for their thoughtful guidance, advice, and encouragement. I have much enjoyed learning not only their knowledge but also their outstanding way of thinking.

Thanks are also extended to technical staff members: Mr Edsel Villa and Mr Ken Smart for their technical assistance throughout the project; Mr David Healy for his assistance with the mechanical setting; and Mr Philipp Hof for his assistance with programming the microprocessors.

Finally but not least important, I would thank my whole family for their education, advice, support and tolerance. Not forgetting anyone, would like to give special thanks to my wife, mum, dad, and my parents-in-law. Without them, I would never reach this far.

GLOSSARY

AC (ac): Alternating current

ADC: Analog to Digital converter

CAES: Compressed air energy storage

DAC: Digital to Analog converter

DC (dc): Direct current

DSP: Digital signal processing

ECC: Electrically connected circuit

EMC: Electromagnetic compatibility

FPGA: Field-programmable gate array

ICs: Integrated circuits

INC: Incremental conductance

MICs: Multiple input converters

MISO: Multiple-input single-output

MOSFET: Metal-Oxide Semiconductor Field-Effect Transistor

MPP: Maximum power point

MPPT: Maximum power point tracking

NMOS: N-Channel Metal-Oxide Semiconductor Field-Effect Transistor

OVP: Over voltage protection

P&O: Perturb and Observe

PCB: Printed circuit board

PHS: Pumped hydro storage

PMOS: P-Channel Metal-Oxide Semiconductor Field-Effect Transistor

PV: Photovoltaic

PWM: Pulse width modulation

RMS: Root mean square

TB: Turbine

UVLO: Under voltages lock out

TABLE OF FIGURES

TABLE OF TABLES

CHAPTER 1 INTRODUCTION

1.1. ELECTRICITY IN RURAL/ISOLATED AREAS

A lot of people in remote areas in many countries are still living without electricity because of the unavailability of a local power network or grid and the inability to purchase expensive off-grid electric power generation systems. It is estimated that globally, more than 1.2 billion people are still without access to electricity [1]. Due to the lack of electricity, there are numerous difficulties for basic requirements such as lighting, radio and television, refrigerators, and computers. The absence of electricity also obstructs education, health services, and industrial activities [2].

Improving electrical network has improved the education environment and medical services significantly [3, 4]. Electricity is the basic need that can encourage educated people to stay in the rural/isolated areas, which will increase the quality of schools and hospitals [5]. Clearly, the presence of teachers and doctors in these regions, people are able to access higher education level and health care services. With the availability of electricity, schools can have better teaching equipment, people can access to many sources of knowledge, and hospitals are able to run 24h emergency services [5]. Another advantage of having electricity is avoiding burning fuels for cooking and lighting, which reduces the impact on household's health [6]. With the electric pump, people are able to access to clean water that considerably improves their health levels [7].

There is a relationship between the inhabitants of a dwelling’s welfare, and energy consumption. If their income increases, there will be more options for them when using energy. On the other side, household welfare can be improved significantly when using modern electrical appliances [8]. A study has shown that the average household's well-being was extended by using limited diesel power systems for a few hours a day in comparison with the local conventional methods [9]. The results also indicated that utilizing micro/mini-hydro grids can produce sustainable welfare benefits [3].

1.2. MULIPLE INPUT RENEWABLE ENERGY SYSTEM

Despite the lack of power grids in most of isolated areas, there are often plentiful renewable energy resources which can be used to generate electricity. Recently, researchers have focused on systems that combine multiple sources of renewable energies, which is called a hybrid renewable energy system [10]. The reliability and cost of energy have improved owing to the availability of many sources of energy to support each other in a cost-effective way [11]. For example, when solar energy is not available at night, wind source can be a suitable support. Depending on local conditions of the areas that might offer many renewable energy sources, choosing the sources with lower costs associated with them is preferable. In addition, if storage batteries are being used, battery life can be increased in comparison to single source systems [10].

Based on the electricity generation technologies, different systems are available and applicable for rural areas, such as solar, wind, hydro, biomass, and wave. The combination of renewable power sources such as PV or wind, with a fossil fuel based power source provides more energy on demand capability, but is less sustainable and is potentially more expensive to purchase, run, and maintain. Thus, by altering the power sources to primarily renewable energy resources, electricity generation will be available for different periods of time for different natural conditions and environments, such as for islands, plains areas, and mountainous regions [12].

The annual electricity consumption of 1000 kWh per year per capita has been identified as the boundary for basic life conditions and improved survival [13]. If these renewable energy resources can be harvested and converted to around 350 Wh for a dwelling per day, it would be enough to provide for basic electricity needs (such as lighting and battery charging) and improve living standards [14].

1.3. MAXIMIZING THE USE OF RENEWABLE ENERGY

Considerable research efforts have been applied to studying methods that can convert a useful amount of available renewable energy into electrical power, and techniques to improve the efficiency of that conversion. Maximum Power Point Tracking (MPPT) is one of the standard controlling techniques used in photovoltaic (PV) solar panel systems to maximize the input power to the converter by self-adjusting the load. However, almost all of these methods are optimized for a single effective power source. Also, most of these converters are connected to a power grid or are used as an auxiliary backup power supply. Many isolated areas lack power grids [1], and therefore, dependence on one renewable source is not a reliable method to maintain a stable power supply. Gathering energy from multiple renewable resources and utilizing some form of energy storage appears to be a preferable solution in rural or remote areas. For these reasons, there is the need for a multiple-input-single-output power converter that utilizes a MPPT algorithm for each of the input sources which can also meet the combined needs of load demand and energy storage.

To increase the use of renewable energy sources in remote and isolated areas, especially in developing countries, reducing cost while maintaining high conversion efficiency is one of the most important factors. A good MPPT algorithm and a high-efficiency power converter are essential requirements to improve the utility of energy converters. The second way to improve overall system cost lies in the components of the converter. The removal of expensive components helps to minimize cost and can improve the system reliability, such as avoiding galvanically isolated current sensors and the replacement of high-end microprocessors by long-term stable analogue circuits.

1.4. RESEARCH OBJECTIVE

The aim of this thesis is to develop a low-cost MPPT multiple-input power converter for home applications in isolated areas. The converter must be suitable for most of the common small scale renewable energy systems, and be able to support two types of inputs such as wind/micro-hydro turbine and PV. The design must be able to satisfy MPPT requirements for each input source and do this with the lowest cost of components without sacrificing power conversion efficiency. Besides generating power to a dc output, the converter must also able to appropriately charge an energy storage battery.

1.5. THESIS OUTLINE

The design and development of a low-cost MPPT multiple-input-single-output power converter is presented in this thesis. This includes the search for a suitable topology and circuitry that integrates multiple sources to a single output. Once the structure and components are selected, the details functional circuits of the converter are designed and simulated by various software tools. The design is then transferred to PCB layout. When the PCB is fabricated, components are mounted onto it, and the microprocessor is programmed for a complete converter. Testing is carried out in the laboratory environment to confirm the operation of the converter in all application conditions.

This thesis includes six chapters. Chapter 1 presents the background of using electricity in isolated/rural areas and the aim of this project. Chapter 2 gives descriptions of systems that use renewable energy and could be used in a remote off-grid home application, basic details of these systems, and the comparisons between power conversion topologies and functional blocks. The proposed topology for implementation and other functional circuits are also undertaken in this chapter. The detail of circuits used, design and calculations, and simulations are shown in Chapter 3. Chapter 4 covers PCB layout, including two options of 2-layer and 4-layer design. The investigation and comparison between these versions are made for the final PCB of the converter. Test results of the converter are presented and discussed in Chapter 5, including all scenarios that can be expected to happen in real applications. Chapter 6 presents conclusions and comments on further developments of the converter.

2.1. MAXIMUM POWER POINT

2.1.1. Photovoltaic solar panels

Important characteristics of a solar PV cell are shown in Figure 2-1 [15]. The operation of the PV cell for any defined and fixed amount of insolation will be at a certain point along the curved red line (I-V curve), and the value of output power will be defined at a point along the blue line (V-P curve). The left-most point of the graph is the Short Circuit Current (I_{SC}), the point at which the cell is operated with a short circuit load (V = 0 V). Conversely, the right-most point on the graph is the Open Circuit Voltage (V_{OC}), where the panel is operated with an open circuit load (I = 0 A). There is a point on the I-V Curve where the maximum power output is positioned and this point is designated as the Maximum Power Point (MPP). The voltage and current at this point are called as V_{MPP} and I_{MPP}.

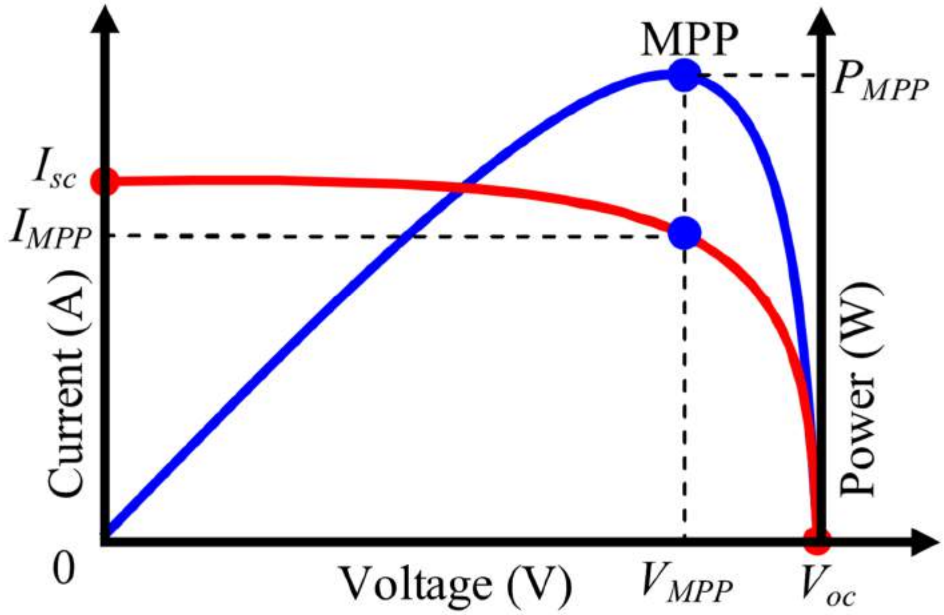

Figure 2-1. The V-I and V-P characteristics of a solar PV cell [15]

Temperature and different isolation levels (light intensity) are the two most important factors that strongly affect the characteristics of solar panels [16]. As a result, the MPP of individual solar panels vary significantly during the day being influenced by time of day (position of the sun and time of year), amount of cloud cover, and temperature. Therefore, it is essential to track the MPP in all conditions to ensure the maximum power can be extracted if required.

2.1.2. Wind/hydro turbines

Figure 2-2 shows the power-speed characteristics of a 3-kW, three-blade horizontal axis wind turbine with a rotor diameter of 4.5m [17]. These curves can be obtained by wind turbine tests or calculated during the design phase by manufacturers. At a given wind speed (μ), the operating point of the wind turbine is determined by the intersection between the turbine torque-speed characteristic and the load torque-speed characteristic [17]. There is a maximum power point at a given value of wind speed. For example, as identified in Figure 2-2, at a wind speed of 5 m/s, the maximum power the turbine can generate is about 500 W at a rotational speed of 500 rpm. The rotational speed and generated power decrease when drawing higher current at the turbine output. If the load reduces from the maximum power point, then the generated power drops and the rotation speed of the turbine increases. When the wind speed changes, the power-speed curve also varies accordingly. However, under varying wind speed conditions the shape of the characteristics curve essentially remains the same, which includes a maximum power point at a certain turbine speed (that is, just one global maxima).

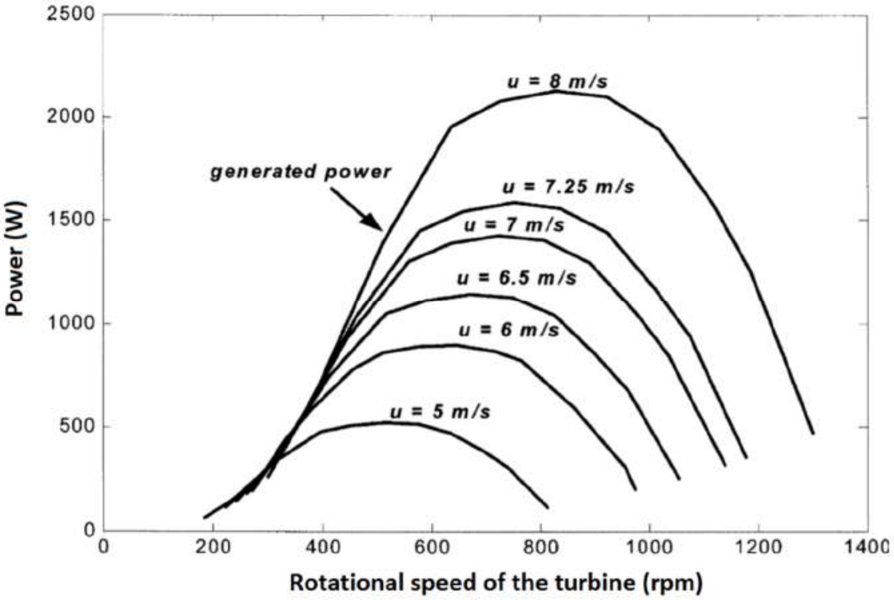

Figure 2-2. Power-speed characteristics of a wind turbine [17]

Regarding micro-hydro turbines, the power speed curves of these turbines for various water flow rates are a similar shape to wind turbine curves. As shown in Figure 2-3 [18], there are some variations between practical and theoretical power-speed curves dependent on the theoretical model being used. Similar to the PV input, the power converter also needs to be able to alter its effective input impedance to any possible turbine output in order to track the maximum power point in various wind/water flow conditions if required.

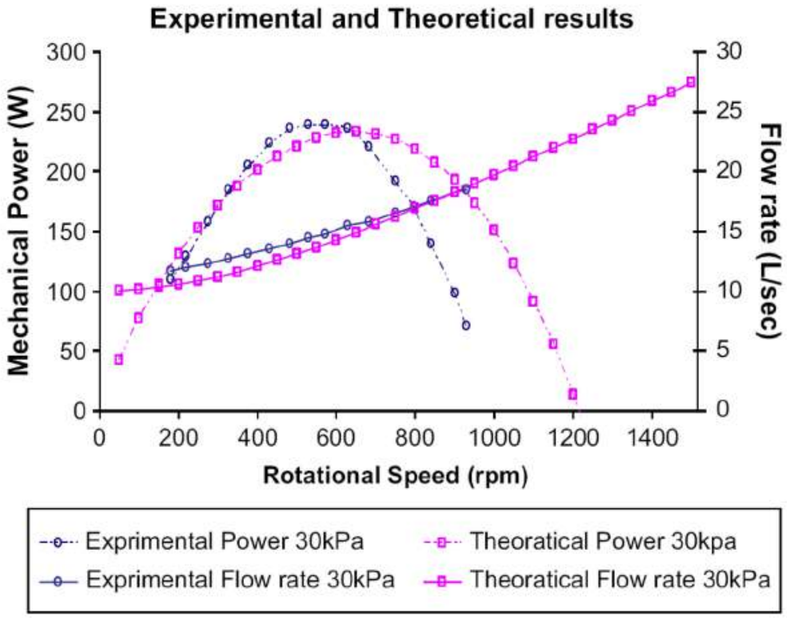

Figure 2-3. Experimental and theoretical output power of the hydro turbine at different speeds [18]

2.2. MULTIPLE INPUT POWER CONVERTERS WITH MPPT

Multiple-input converters (MICs) have some advantages over using independent power converters. One advantage being the reduction in the number of the components used for the same purpose, which means a smaller space is needed for the system, an overall cost reduction, and an increase in the efficiency of the converter. Also, MICs do not require synchronization for maximizing the output power of the converter depending on the load requirements [19].

There have been several isolated and non-isolated topologies of multi-input converters proposed in the last decade. The magnetically connected circuit (MCC) is a galvanically isolated MIC topology based on the use of transformers to achieve flux addition [20, 21] (see Figure 2-4). However this topology is often undesirable because having such a transformer makes the system bulky, costly and less efficient [21]. There is no MPPT for all input sources, and the documented experiment from [21] was only for achieved 80 W of output power which is substantially lower than the range of interest for this thesis. Moreover, it requires complicated control and protection methods because of leakage inductance and parasitic elements [20].

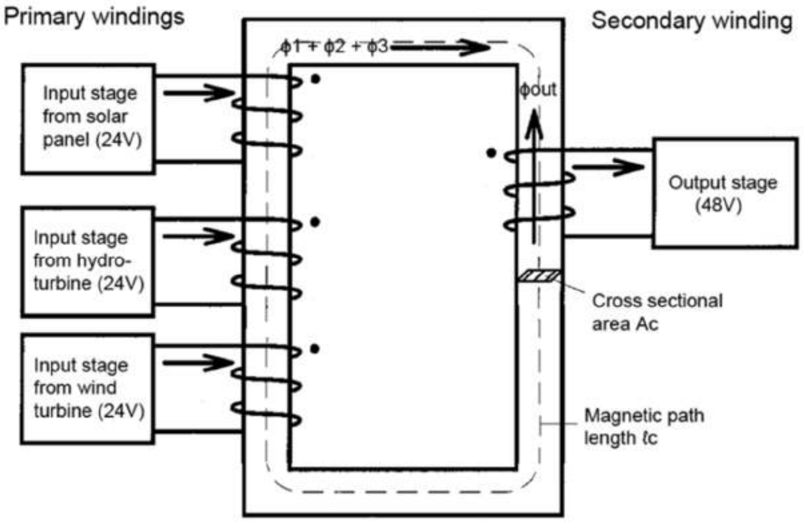

Figure 2-4. MIC topology based on flux addition in the transformer [20]

Non-isolated MIC topologies (also called electrically connected circuit (ECC) topologies) rely on combining various input power generation sources either in series or parallel. This topology is much more attractive for the application of interest as it involves fewer and smaller transformers, is low cost, and its modular structure allows connection to several input sources in parallel and/or series connection [20]. ECC parallel connected systems can be operated in two different modes: (1) only one of the different energy inputs can supply power to the load at a time [22], or (2) different sources simultaneously supply power to the load [23, 24, 25, 26]. Several inputs can also be connected in series to provide more energy to the load [27, 28].

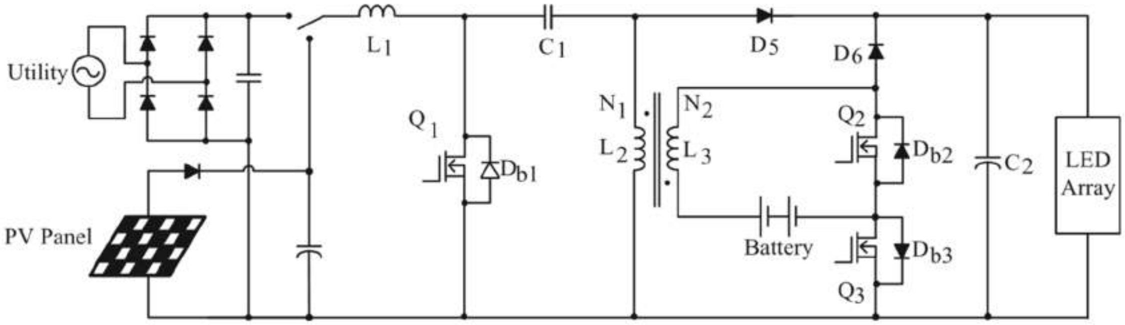

Figure 2-5. Hybrid-input power supply for battery charging and HB-LED driving [22]

An ECC solution that can be used for a stand-alone application, especially for home power in isolated areas, is shown in Figure 2-5 [22]. This system includes a battery charger. However, it is unable to draw energy from two input sources simultaneously. Also, the MPPT algorithm is only implemented for the PV panel. The maximum output power of the converter from [22] is again identified as 80 W.

A simple circuit that can increase the number of input sources is demonstrated in Figure 2-6 [23]. Each input can simultaneously supply power to the load. A capability of 450 W output power is stated by [23], however, MPPT is only applied to PV sources. A similar idea using one inductor, but using a step-down topology, is shown in Figure 2-7 [25]. The advantage of this converter is that is uses dynamic MPPT and charge control, and therefore can reduce circuit elements and cost. This appears to be simpler and cheaper than the combination of three conventional buck dc/dc converters, with the elimination of two inductors and two low-side switching transistors. However, there was no cost analysis of adding the complicated digital control module and 4 complementary pairs of power transistors. These might lead to no change in total expense compared to the ordinary configuration. Additionally, this topology only works when the input voltage is higher than the output voltage, and therefore reduces the flexibility of using different energy sources. For example, the output voltage of wind turbines and PV systems may be too low to operate under low source power conditions.

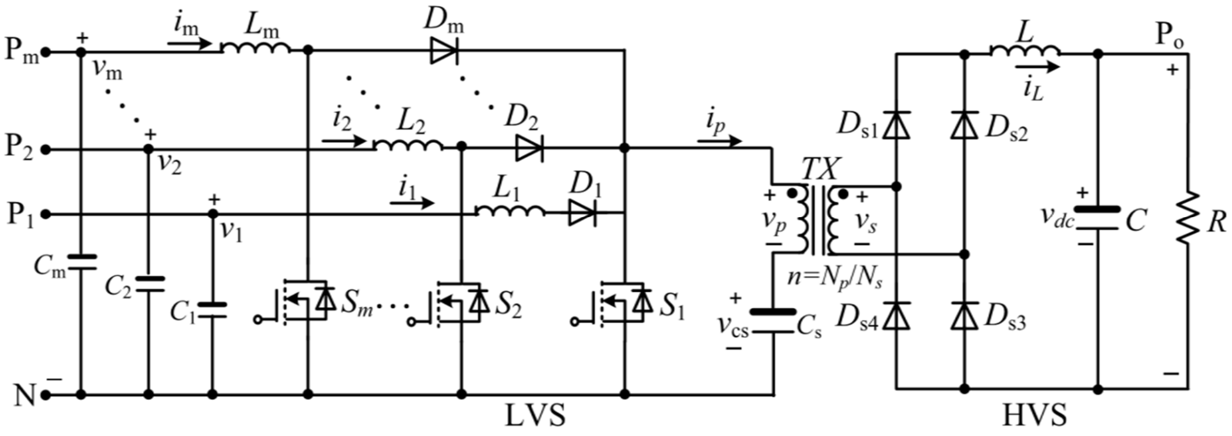

Figure 2-6. Multiport dc/dc converter of multiple different renewable energy sources [23]

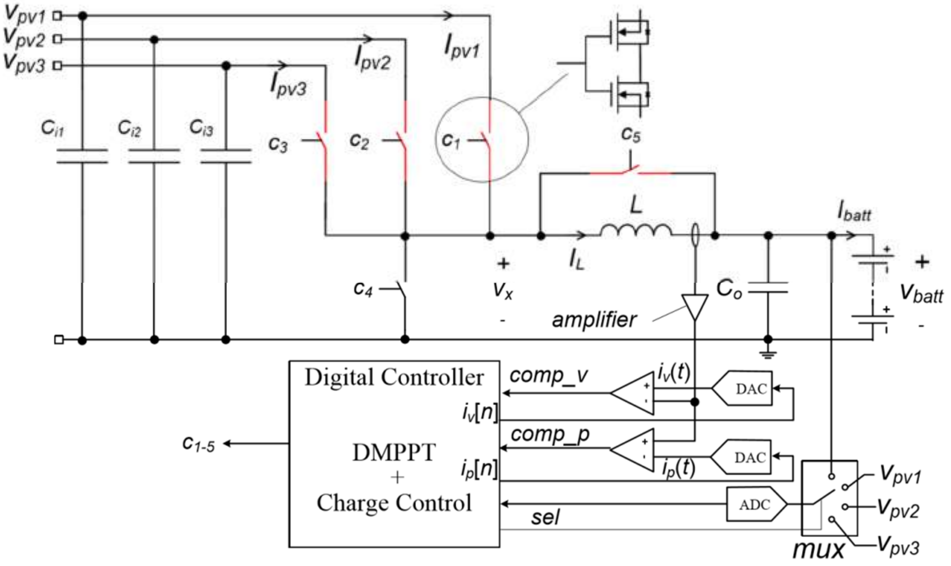

Figure 2-7. Multi-input single-inductor dc/dc converter [25]

In another example, a topology is employed that includes two transformers for each parallel-connected input [24, 26]. These converters have a dual input power converter that includes a PV panel and a wind turbine (or grid). There are two MPPT control blocks, one for each input (see Figure 2-8 and Figure 2-9). The converters identified by [24] and [26] have an output power of 350 – 700 W, high efficiency, and the possible number of inputs can be increased beyond two. However, there is no secondary circuit for charging and protecting a battery that is often expected to be connected to the dc link/bus (discussed in Section 1.3), which is important in remote area applications.

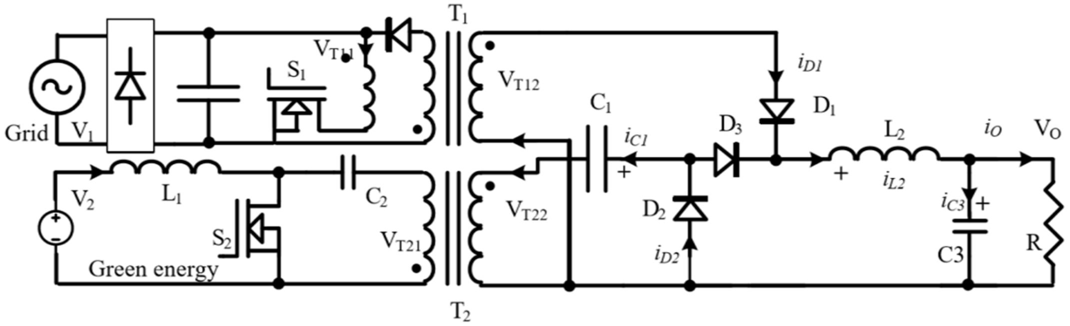

Figure 2-8. Hybrid power system with a two-input power converter [24]

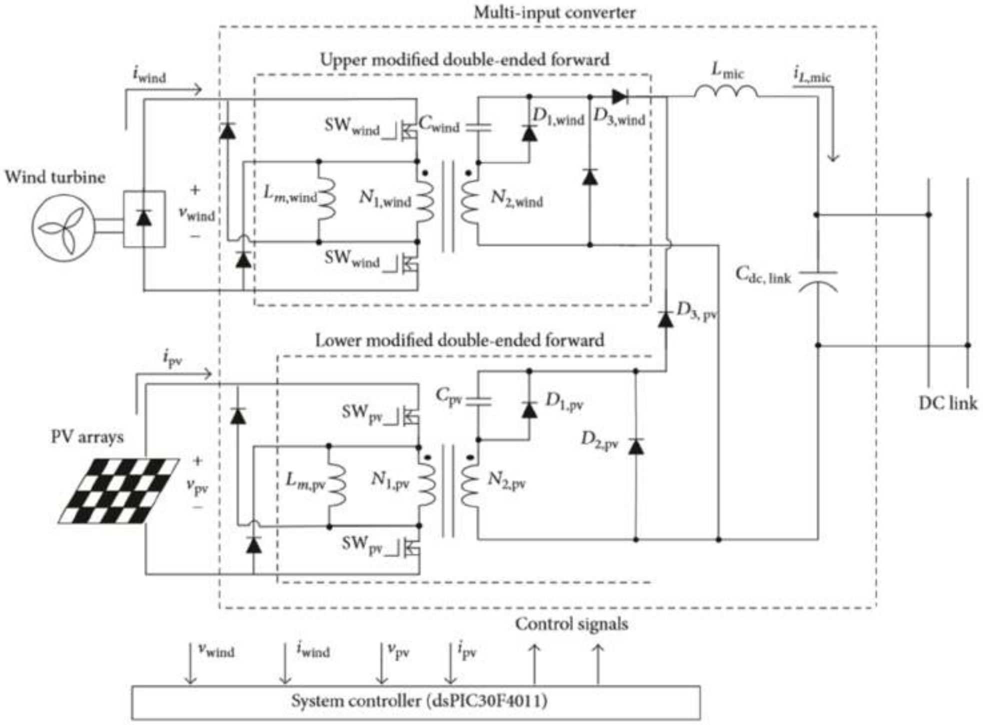

Figure 2-9. Multi-Input converter with MPPT feature [26]

Regarding series topologies of MICs, there are several potentially appropriate converters that have been presented. One of the better examples for the application area under consideration is the fusion of two Cuk converters [27] as shown in Figure 2-10. The circuit configuration includes one PV source and a wind turbine. MPPT for both inputs sources is possible. However, [27] only provides analytical and simulation results. Other information such as power ratings, input voltage range and efficiency are unclear.

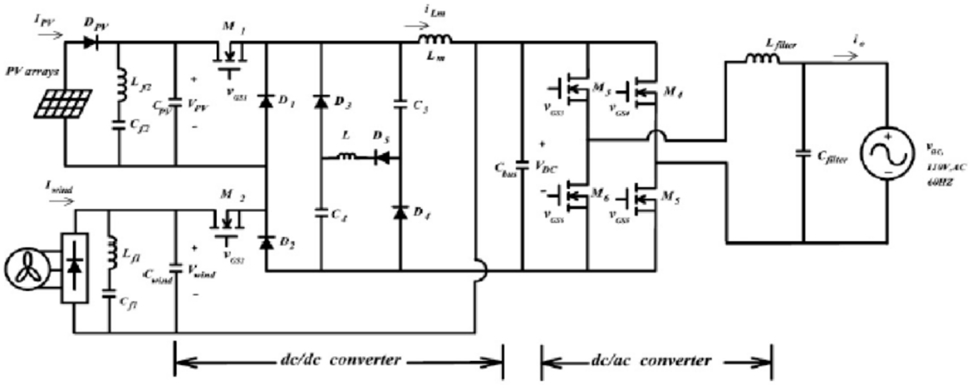

Figure 2-10. A Multi-Input dc/dc converter for integrated wind and PV [27]

2.3. ENERGY STORAGE

A drawback of the renewable energy system is that they depend greatly on the weather and climatic conditions [29]. Although multiple renewable energy sources enable simultaneous and separate power conversion, there are still many instants when the produced power does not satisfy the load demand. For example, a system that utilizes a PV system and a wind turbine could not produce power on a windless night. To overcome this issue, especially for a single home in isolated areas, an energy storage system is required. Currently, available storage technologies include pumped hydro storage (PHS), compressed air energy storage (CAES), thermal and chemical energy storage, batteries, super capacitors, flywheels and superconducting magnetic energy storage. For large scale storage applications, a comparison between storage technologies and their applications has been carried out [30] (see Figure 2-11). In a small and stand-alone (off-grid) system, however, suitable means of storage could be the PHS, CAES, and battery because of their duration of storage, availability, and the feasibility of installation.

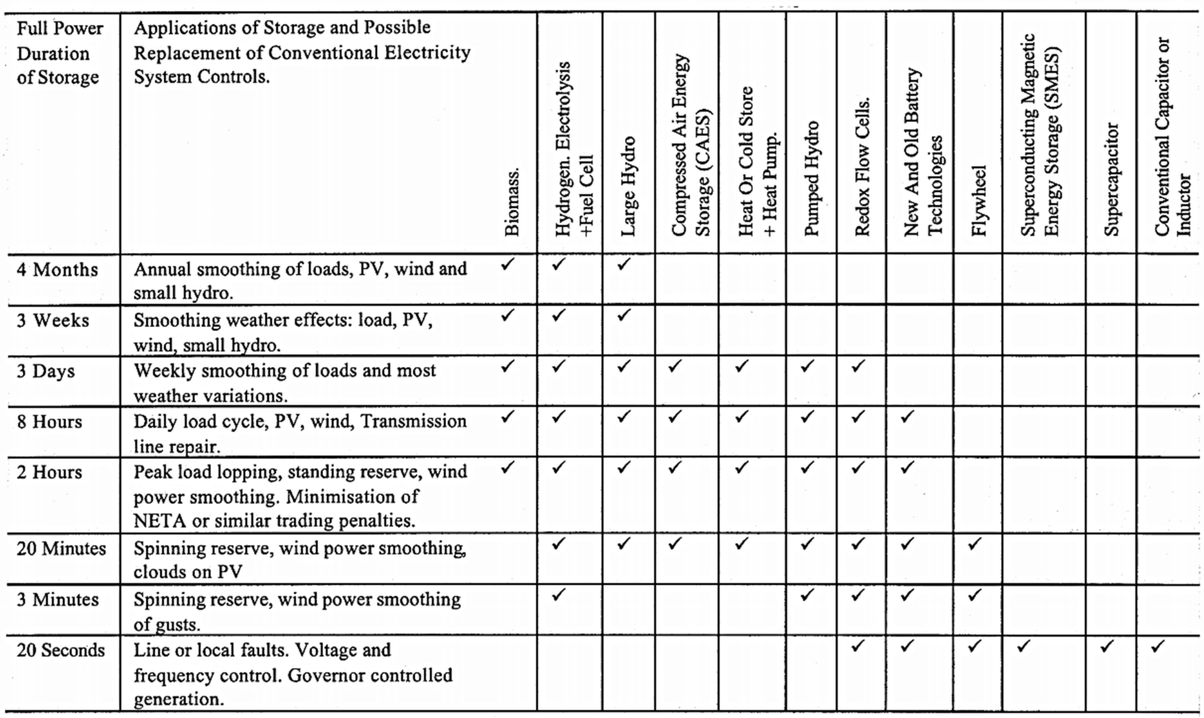

Full Power Duration of Storage	Applications of Storage and Possible Replacement of Conventional Electricity System Controls.	Biomass.	Hydrogen. Electrolysis +Fuel Cell	Large Hydro	Compressed Air Energy Storage (CAES)	Heat Or Cold Store + Heat Pump.	Pumped Hydro	Redox Flow Cells.	New And Old Battery Technologies	Flywheel	Superconducting Magnetic Energy Storage (SMES)	Supercapacitor	Conventional Capacitor or Inductor
4 Months	Annual smoothing of loads, PV, wind and small hydro.	✓	✓	✓									
3 Weeks	Smoothing weather effects: load, PV, wind, small hydro.	✓	✓	✓									
3 Days	Weekly smoothing of loads and most weather variations.	✓	✓	✓	✓	✓	✓	✓					
8 Hours	Daily load cycle, PV, wind, Transmission line repair.	✓	✓	✓	✓	✓	✓	✓	✓				
2 Hours	Peak load lopping, standing reserve, wind power smoothing. Minimisation of NETA or similar trading penalties.	✓	✓	✓	✓	✓	✓	✓	✓				
20 Minutes	Spinning reserve, wind power smoothing, clouds on PV		✓	✓	✓	✓	✓	✓	✓	✓			
3 Minutes	Spinning reserve, wind power smoothing of gusts.		✓				✓	✓	✓	✓			
20 Seconds	Line or local faults. Voltage and frequency control. Governor controlled generation.							✓	✓	✓	✓	✓	✓

Figure 2-11. Storage technologies and their applications in large sale systems [29]

The flexibility of multiple input renewable energy systems can be achieved by pumped hydropower storage [31], where water is present and is used for generating power. Pumping water to a higher reservoir allows accumulation of surplus energy in the form of the potential energy. Releasing the water through a turbine allows the transformation back to electrical energy. This storage system is similar to a conventional micro hydropower system in terms of using stored energy in a reservoir. The storage system establishment is comparable to a micro-hydro system, and therefore practicality depends on environmental geological conditions of the area.

Compressed air energy storage (CAES) systems are promising technologies in the renewable energy field, as they offer a high reliability, low environmental impact and a high energy density [32]. These systems have been applied as a storage medium for electrical energy at utility scale [33]. The micro-CAES system, on the other hand, is being analyzed, researched and developed for stand-alone energy systems [32, 34, 35, 36] for use in rural areas and developing countries [34]. It is obviously environmentally friendly due to compressed air being the only energy source for the charging and discharging process. The micro-CAES can be also integrated with thermal energy storage systems to increase their conversion efficiency [32, 39, 40].

Battery storage still appears to be the best option for a small off-grid renewable system owing to availability, cost, and flexibility of configuration. With a wide range of battery types and capacities, an optimal battery system for a specific application can be designed and implemented. In such systems, the battery cost, service life, weight, and needed space are considered for the best selection. An investigation on the use of a battery system for an off-grid application was made [37], where the optimal battery is selected among lead acid, nickel cadmium, and lithium iron phosphate battery types. The results show the best variant in the price/performance ratio was the lithium iron phosphate battery [37].

2.4. SYSTEMS STRUCTURE

Based on literature search results as identified in section 2.2, there is reasonable scope to design a low-cost, multiple renewable energy source input, MPPT converter for home application in isolated areas. Figure 2-12 shows a conventional system of multiple renewable input sources [10, 37, 38]. However, for the particular application of powering homes in remote locations, this topology is likely to be inapplicable mainly because of cost issues and no grid connection. To increase the use of renewable energy systems in remote and isolated areas, reducing cost is one of the most important factors.

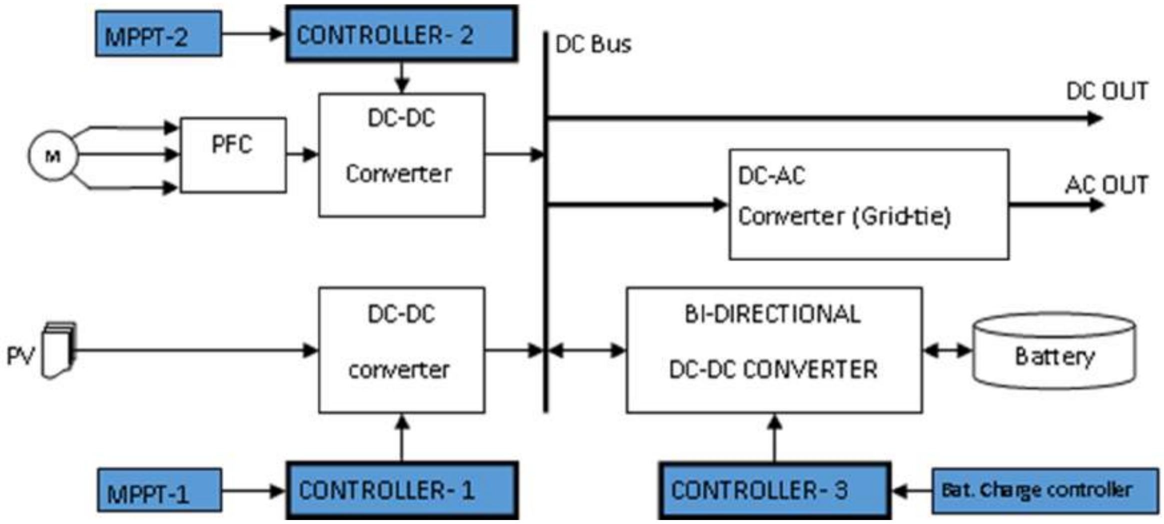

Figure 2-12. A conventional system of multiple renewable sources for home application

One method employed to lower cost is to allow the converter to draw the maximum available energy from sources at the highest possible efficiency. A good MPPT algorithm and a high-efficiency converter are the main requirements to improve the efficacy and efficiency of power conversion from energy sources that may be available. Another method to reduce cost is by selecting the right topology for particular applications. In many instances, the dwelling will only have one input (for example a single, micro hydro, wind turbine, or PV input), but there could potentially be multiple inputs. As such, this requires that the converter must be able to work with a single input, or handle multiple inputs simultaneously. The converter should also be able to connect to a wide range of input voltage and power.

Obviously, a grid-tie converter is not required in the system for a house in an isolated area and not connected to an electric power grid. To reduce system cost, the dc-bus voltage should be designed to be compatible with the level of the battery voltage to be used. In that case, the battery charging and managing block can be integrated into the main power converters. Additionally, improvement of the overall system cost lies in the component composition of the circuit. The removal of as many of the expensive components as possible to minimize the cost and improve the system reliability, such as magnetic devices (particularly ferrite material), and expensive sensing options (for example Hall effect current sensors and overly complex microcontrollers) is necessary. Thus, a suitable topology design for a low-cost multiple input MPPT converter for home applications in isolated areas is shown in Figure 2-13.

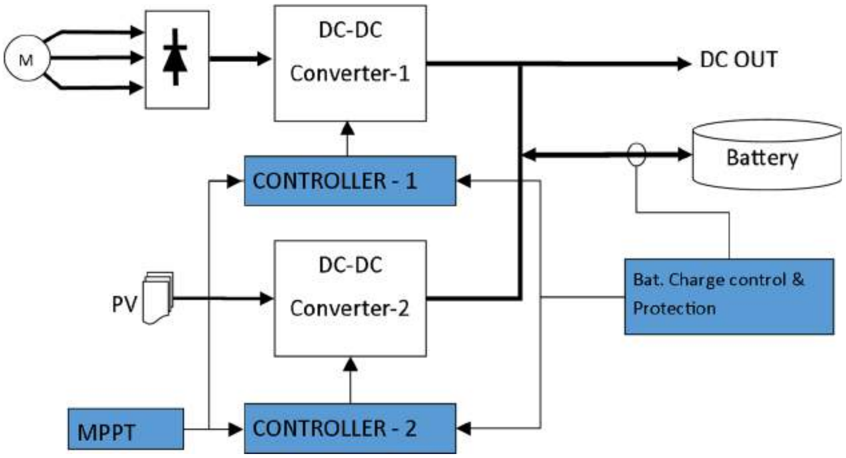

Figure 2-13. A suitable block design for the converter

The multiple-input converter comprises two dc/dc converters and a rectifier (for the ac generator output). In this arrangement, the dc/dc converter topology is regarded to be of the same type for both forms of inputs. The first and most important step in designing a dc/dc converter is the selection of the topology. The target of this system is to deliver as much power as possible over the widest power range as possible while keeping the cost to a low level, and maintaining reasonable power conversion efficiency. As each power converter structure has limitations in its capability of transferring power, it is hard to find a topology that will be suitable for a broad range of input power.

2.5. POWER CONVERSION TOPOLOGY

There are a number of basic topologies used for power conversion applications, such as flyback, forward, push-pull, half-bridge, and full-bridge. The maximum output power has regularly been used as the key factor when choosing a topology. Besides, the topology selection step also takes into consideration many other aspects such as voltage stress over active devices, input voltage range, total cost, and the size of the converter. The size of the power converter is mainly determined by the transformer and the number of the switching devices. These mentioned topologies can be categorized as either single-ended or double-ended depending on the monopolar or bipolar usage of magnetic flux in power conversion transformers. With the same power rating, a double-ended topology normally requires a smaller transformer core than that of a single-ended configuration. In addition, the former does not need an additional reset winding. Table 2-1 summarizes several main factors and their common power ranges of mentioned topologies [19, 41, 42].

Table 2-1. Topology of low voltage dc/dc comparison [19, 41, 42].

Topology	**Power range**	**Transformer Utilization**	**Number of active switches**	**Voltage stress on the active switches**	**Cost**
Flyback	< 250 W	Single-ended	1	$> V_{IN} + N.V_{OUT}$	Lowest
Forward	50 – 250 W	Single-ended	1	$> 2.V_{IN}$ $(D_{max} = 0.5)$	> Flyback
Active Clamp Forward (ACF)	50 – 500 W	Double-ended	2	$V_{IN}/(1-D)$	Flyback < ACF < Forward
Push-pull (P-P)	100 – 1 kW	Double-ended	2	$> 2.V_{IN}$	> ACF
Half-bridge	500 – 1.5 kW	Double-ended	2	$> V_{IN}$	> P-P
Full-bridge	1 – 3 kW	Double-ended	4	$>= V_{IN}$	> Half-bridge

The configuration of the converter will depend on the maximum output power. For power ratings higher than a few kW, the converter's topology would require more sophisticated switching schemes and more expensive components. In single dwellings in rural and/or remote areas, the power generator is normally sized from 10 to 100 W [1, 38]. However, for higher living standards, the generated power should be high enough for standard appliances, such as a TV, a small fridge, light bulbs, a radio, communication (cell phone chargers), and a water pump. In this thesis, the target is to design a converter to handle nominally 2 kW in total. For the mentioned power capabilities, Converter 1 and Converter 2 should be a push-pull, half-bridge, or full-bridge structure.

The push-pull, half-bridge, and full-bridge are using double-ended transformers where the power transfer takes place in both quadrants of the B-H curve. For a high power density converter, these topologies appear to be the best choice. With this selection, the transformer core can be fully utilized and there is no special provision required to reset the transformer. Another benefit of these topologies is that the transformer can be more optimized owning to the extension of duty cycle. These topologies are allow the duty cycle on each side reaching nearly 50 % which can achieving almost 100 % maximum effective duty cycle at the output filter. With an appropriate primary and secondary turn ratio of the transformer, RMS current in the transformer can be reduced significantly. Therefore, a considerably reduction in the size of the output filter can be made [19, 41, 42].

2.5.1. Push-pull

A push-pull topology is shown in Figure 2-14 [42]. The output rectifier diodes D1 and D2 can be replaced by synchronous MOSFETs for higher efficiency. The topology has the advantage of being double-ended, however, the peak voltage stress placed on the primary switches during the off state is very high (well over two times the input voltage) [42]. The other disadvantage of push-pull converters is that they require proper matching of the switch transistors to prevent unequal on times, since this will result in saturation of the transformer core (and failure of the converter) [19]. In addition, there is the need to have a centre-tap on both primary and secondary of the transformer, and therefore, increase the cost of the transformer.

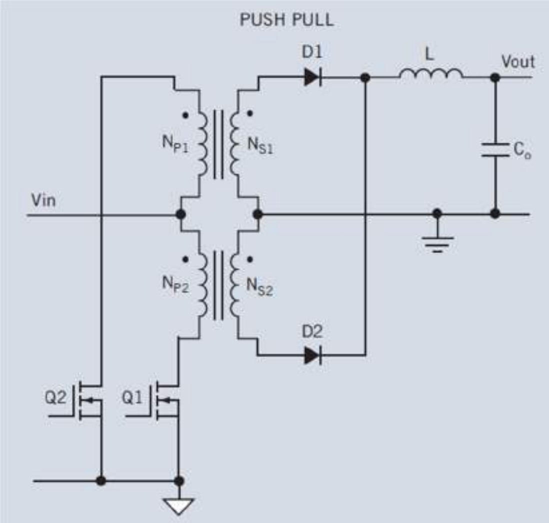

Figure 2-14. Push-pull topology configuration [42]

2.5.2. Half-bridge

Figure 2-15 shows a half-bridge topology arrangement [42]. The advantage of the half-bridge is the voltage stress over the primary switches does not exceed the input voltage [42]. In addition, this topology comprises only one primary winding that allows better utilizing of the core transformer window. However, the topology is not compatible with current-mode control schemes. The reason is voltage of the midpoint between C1 and C2 cannot be maintained in current-mode operation or when applying cycle-by-cycle current limiting. To work with the current-mode control, a balancing circuit can be added to the half-bridge converter, however these circuits are relatively complex [42].

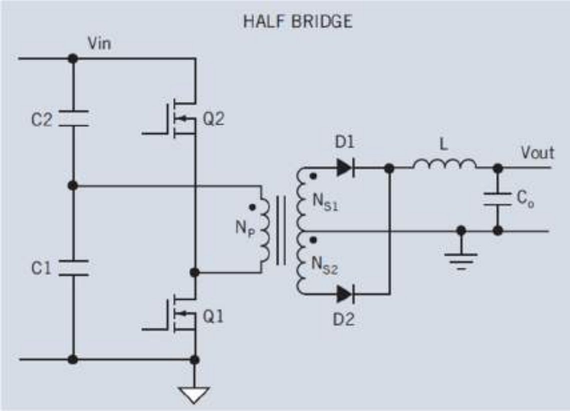

Figure 2-15. Half-Bridge topology configuration [42]

2.5.3. Full-bridge

The configuration of a full-bridge topology is shown in Figure 2-16 [42]. This formation offers all of the double-ended advantages. The stress voltage on the primary switches equals to the input voltage. An excellent utilization of the transformer is archived owning to the single primary winding. With the same power and input voltage, the primary current of the full-bridge converter will be a half of that number in the half-bridge converter. This characteristic allows the full-bridge achieving higher efficiency than the half-bridge converter, especially in the heavy load conditions. However, the full-bridge configuration requires four primary switches, and therefore, adding driving circuitry and cost to the converter. Compared with the half-bridge, this extra cost can be offset by the shrinkage of input capacitor size and the reduction in the amount of heat sinking material required owing to improved converter efficiency.

Another similar configuration is the phase-shifted full-bridge which uses in high input voltage and high power applications. The control methodology for this is different from ordinary full-bridge topology. The controller allows the primary switches changing their states at zero voltage only while maintaining the switching frequency constant. Zero voltage switching is particularly favorable for high input voltage applications as it avoids the switching losses that are typically incurred during conventional PWM operation and timing [83].

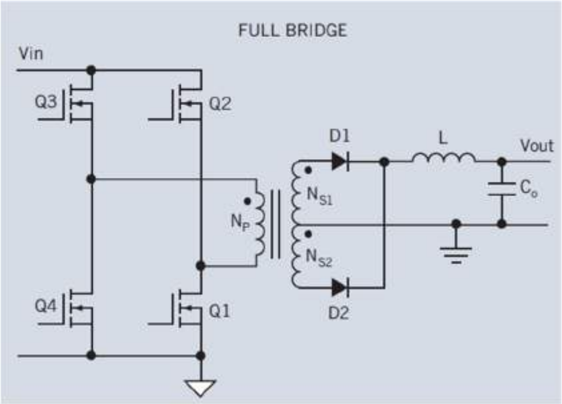

Figure 2-16. Full-Bridge topology configuration with centre-tap [42]

2.5.4. Z-Source

The Z-source inverter employs a unique impedance network to couple the inverter main circuit to the power source, which provides a novel power conversion concept [43, 44]. The Z-source inverter can step up and down the input voltage thus providing unique features, such as ride-through capability during voltage sags, reduced line harmonics, improved power factor and reliability, and extended output voltage range [44, 45].

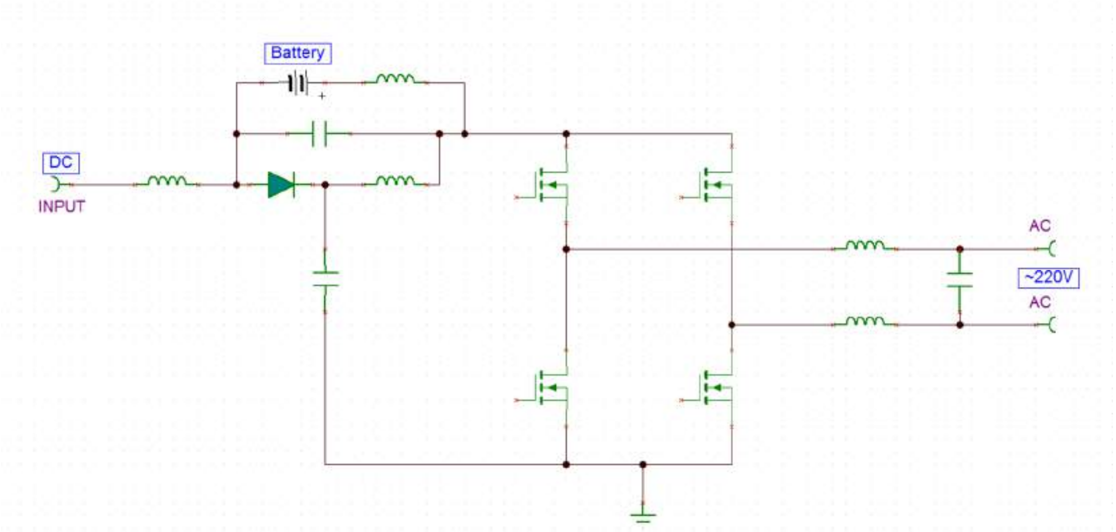

Figure 2-17. Proposed off-grid z-source inverter

When analyzing Z-source topologies, there is room for developing an off-grid inverter that contains a storage battery (optional) to generate ac sine wave power (220 V ac) from low dc voltage source directly. This would be a suitable choice for isolated areas because this inverter takes advantage of the Z-source topology in terms of the wide range of input voltage and cost reduction (see Figure 2-17). From the customer's point of view, this kind of inverter would be more convenient as it is easier for them to buy standard ac voltage household appliances. However, currently there is no specific integrated circuit that is designed for the control of a Z-

Source topology. Therefore, it is required to build the entire control circuit, which means a lot of extra apparatus-specific componentry leading to a more expensive system.

On the other hand, many non-isolated Z-source and isolated dc/dc converters have been proposed [46-51]. Nevertheless, they are mostly basic converters that work in specific conditions, or have just identified fundamental calculated and simulated data. Among these proposals, the quasi-Z-source inverter (qZSI) inherits all the advantages of the traditional ZSI and has some additionally advantages, including passive component stress reductions and continuous input current features [52-55]. Thus, this topology is attractive for renewable energy sources interface applications, such as photovoltaic panels, wind turbines and fuel cells. Figure 2-18 shows a proposed quasi-Z-source dc/dc converter.

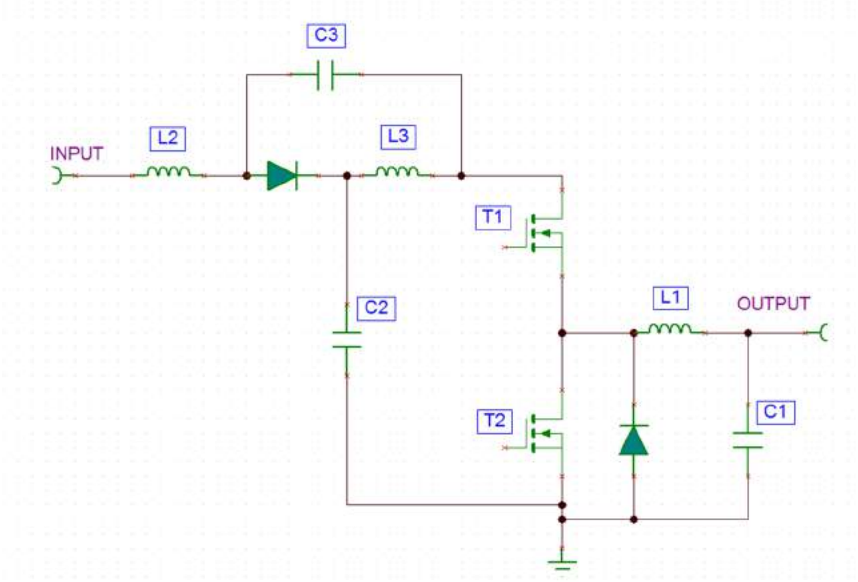

Figure 2-18. DC/DC Z-Source converter

2.5.5. Topology selection

The detailed parameters of the main components of the push-pull, half-bridge, and full-bridge converter topologies are calculated for the intended output power. Table 2-2 shows the comparison of the design of the target converter of 1 kW output power per input source (at the nominal output voltage of 27 V), with an input voltage up to 80 V.

Table 2-2. Comparison of the main features of identified topologies

Topology	**Push-Pull**	**Half-Bridge**	**Full-Bridge**
Current peak at Power switches	44 A (**)	88 A (**)	44 A (**)
Voltage stresses at power switches	208 V (*)	80 V	80 V
Max current	21 A	21 A	21 A

through D1 and D2			
Max voltage stresses over D1 and D2	360 V (*)	360 V (*)	360 V (*)
Switch selection	2 x IRFB4227PbF (200 V, 46 A) ($1.78/unit)	2 x IPD053N08N3GBTMA1 (80 V, 90 A) ($0.77/unit)	4 x PSMN017-80BS (80 V, 50 A) ($0.44/unit)
Middle point capacitors	No	16 x GRM32ER71K475KE14L (4.7 µF, 80 V, X7R) ($0.28/unit)	No
Diode selection	2 x STTH30R04 (400 V, 30 A) ($1.5/unit)	2 x STTH30R04 (400 V, 30 A) ($1.5/unit)	2 x STTH30R04 (400 V, 30 A) ($1.5/unit)
Gate driver	1 x LM5111 ($0.58/unit)	1 x LM5111 ($0.58/unit)	2 x LM5111 ($0.58/unit)
Cost comparison (***)	$7.14	$9.60	$5.92

* 30% of voltage spike has been added to the calculated value.

** Assumed inductor efficiency is 95%

*** Assumed the price of inductors and other parts are the same

As can be seen from Table 2-2, interestingly, the full-bridge converter turns out to have the lowest cost. Also, the full-bridge topology accommodates many advantages in terms of the conversion efficiency and the size of inductor core. Furthermore, it is easier to increase power output capacity by simply changing the inductor and power switches. Therefore, the full-bridge topology is the most preferred among these configurations.

A comparison has been made between the proposed Z-Source dc/dc converter and a full-bridge converter. Regarding the number of components for one input in the MISO converter, Table 2-3 shows the details of main devices for 1 kW capability calculation in power conversion for the full-bridge and Z-source converters. Both topologies have the same input voltage range (up to 80 V) and operational frequency. The results show the main components cost of Z-source converter is higher than that of the full-fridge topology (by around 15%).

Table 2-3. Full-Bridge versus Z-source topology

	Full-Bridge		**Z-Source**	
	Number	Cost ($US)	Number	Cost ($US)
Power Inductors	1 (0.8 µH, 40 A, 2 mΩ)	1	3 (20 µH, 40 A, 2 mΩ)	6
Capacitors	1	1.6	3	4.5

	(10 x 10 µF, 35V, XR7)		(10 x 10 µF, 35V, XR7; 2x (1000 µF, 100V)	
Diodes	4 (Schottky 20A, 80V)	8	2 (Schottky 40A, 80V)	8
Power switches	4 (75A, 80V NMOS)	3	2 (75A, 80V NMOS)	1.5
Transformer	1	3	0	0
Gate driver	2	2	2 (1 High-side and 1 Low-side)	1
Controller	1 (LM5045)	2	1 (1 Microprocessor)	3
Total		**$20.6**		**$24**

Regarding controlling schemes and functional protections, there will be a lot of apparatus-specific development required in Z-Source topologies due to the unavailability of a specific integrated controller. Therefore, the main controller must be established with custom microcontroller programming and additional discrete components, which will lead to higher cost, more complexity, and less reliability of the system than more conventional topologies. On the other hand, full-bridge dc/dc controllers have been developed and applied widely. There are many options that can be chosen, from a single chip that integrates MOSFET drivers to a separate microprocessor. These controllers include fully functional protection such as soft-start, current limit, and high-temperature shutdown, for a completely stand-alone converter/inverter. Additionally, included feedback loops have been analyzed throughout which includes compensation networks for stability in all working conditions. This resource creates a higher possibility of successful operation when implementing this topology in a multiple-input single-output converter.

To conclude, Z-Source topology is a promising topology in the field of renewable energy. However, the full-bridge dc/dc converter appears to be more suitable for a low-cost MPPT multiple-input power converter in terms of cost, effort, and the potential of success.

2.6. CONTROLLER

2.6.1. Microprocessor-based controller

Over the past few decades, many power management structures and power converters have taken advantage of microprocessors. It is undeniable that the design and implementation of power converters and MPPT based on microprocessor control have become more widespread [25, 26, 57]. However, there are some disadvantages related to microprocessor control based converters. Firstly, the requirement of a high-quality auxiliary power supply, analogue buffers for input signals, and isolated gate driver signals for the microprocessors increases the cost of control sections. Secondly, using digital controllers for analogue systems such as dc/dc converters requires a very high sample rate ADC, a significant number of external sensors, high PWM output resolution, and extremely fast calculation ability to satisfy the dynamic requirements expected, which results in cost increase [58].

2.6.2. Full-bridge PWM-based controller

For each input of the converter, a single-chip full-bridge controller can be used for a cost-effective solution. There is built-in capability for feedback control. Adaptions in the feedback loop of the controller allows for balancing power flow from inputs, integrating a MPPT algorithm, and including battery charge control and protection. Therefore, a fully functional multiple-input single-output MPPT dc/dc converter can be formed.

2.7. MAXIMUM POWER TRACKING METHOD

The converter must be able to self-adjusting its parameters whilst operating to ensure maximum power extraction from the sources can be achieved, thus changing input voltage/current levels based on the MPP positions of the energy source. The MPPT converter can be recognized based on different methods and algorithms. The most popular algorithms are known as perturb and observe (P&O) and incremental conductance (INC). The practical implementation of MPPT controllers are mostly conducted in digital form. As the relatively slow variation of environmental conditions (wind/flow speed, temperature, and irradiance), MPPT based on digital control does not need a high speed analog-to-digital converter (ADC). Therefore, the MPPT algorithms allow the designer to use cheap microcontrollers, for basic P&O [60-62] and INC approaches [61, 62] due to simple and easy implementation. Much more expensive devices, like digital signal processing (DSP) and field-programmable gate array (FPGA) systems must be used when the MPPT method is based on much more involved and burdensome computations, as those required by neural networks and fuzzy logic techniques [63].

Considering the aim of this converter, if a powerful microprocessor is used as the primary controller (equipped with ADCs, DACs, and PWM channels), then the MPPT algorithm could be integrated into its program. However, this will increase the programming effort along with requiring 4 synchronized PWM channels, cycle-by-cycle current limit, temperature protection, over/under voltage shutdown and soft start.

If a particular full-bridge controller is selected, an open and low-cost MPPT system that is able to interact with that controller is needed. There are various solutions for this. Firstly, an analogue MPPT circuit for one input with accurate and fast transient behavior can be used [64, 65] by taking advantage of an analogue multiplier. However, the price of analogue multiplier chips are high (nominally about $6 each), and this functional block leads to an increase in the cost of the converter. Secondly, a digital solution is proposed with the P&O technique [12]. The

MPPT block will need 4 ADC channels and 2 DAC ports for both inputs (PV and wind/hydro turbine).

2.8. CONTROLLING POWER FLOW BETWEEN CHANNELS

On one hand, if a converter relies on a microprocessor-based controller where the MPPT algorithm and power flow procedure on each input are integrated into its firmware, the amount of power from each input to output can be distributed adaptably. The developer is able to select operation modes and power distribution schemes according to different operational conditions. As the converter's running code can be adjusted without any hardware changes, this option appears to be a flexible solution. However, there will be more effort on programming.

On the other hand, an analogue solution for controlling input power from multiple input sources to the single output when using full-bridge PWM-based controller can be implemented. These controllers allow interfacing with feedback loops to adjust the duty cycle by a current value. Normally, it is easier and simpler to make subtractions, additions, and clones for current values than those of voltage values. That means a single feedback loop can be used for both channels, where a full-bridge controller controls power conversion for each input. By using the current mirror structure, the idea of balancing power flow between inputs to the output can be employed, keeping both controllers operating at the same value PWM duty ratio while total available input power exceeds load requirements. Therefore, the converter comprises a single error amplifier for the voltage feedback loop control on both input channels. Similarly, another single error amplifier is used for both channels in the constant current feedback loop.

2.9. CHARGING AND PROTECTING THE ENERGY STORAGE BATTERY

A battery bank appears to be the most suitable option for energy storage in small scale off-grid systems. With the availability of types and sizes, it is very flexible to implement and install an optimal battery storage system in a single home application based on the capacity of the input sources, the power rating of the converter, and the output load demand. As discussed in section 2.3, the best choice for cost over performance is the Lithium Iron Phosphate ($LiFePO_4$) battery [37], and the power conversion system suggested is compatible with this battery technology. However, this storage system usually needs a complicated battery management and protection module. When changing the size of the battery, this module needs to be adapted accordingly. For example, rearranging temperature sensors on battery cells, and redesigning the balancing circuit. Therefore, the $LiFePO_4$ battery system can compromise the popular use of off-grid renewable energy systems in isolated areas due to the lack of technical resources. To counteract this issue, Lead acid battery technology is selected for this system for its availability, simple installation, and protection. However, it is hoped that $LiFePO_4$ battery systems will become simpler in the near future so that they displace Lead-acid batteries.

The converter will be expected to operate over a very wide input-voltage range due to the significant variations in environmental conditions. This range limits the system's ability to convert maximum power from solar cells under all light conditions and turbines under all wind/water flow conditions. The requirement of the converter is that it can convert the input power at the maximum power point while providing full charging function to the battery (depending on external load conditions). This goal can be achieved by implementing a narrow voltage dc/dc battery-charging architecture [66, 67]. The narrow voltage range for the system power bus provides higher system efficiency, minimizing battery charging times and extending battery run times [66]. To maximize the capacity and performance of the battery, the converter should provide a three stage operation to charge a nominal lead acid battery (constant current, constant voltage, and float) [68, 69]. Figure 2-19 shows an example of a typical charging profile for a 12 V Lead Acid battery [69]. The constant-current charge takes up roughly half of the required charge time; the constant voltage stage continues at a lower charge current to provide saturation, and the float charge compensates for the loss caused by self-discharge. For a substantially discharged battery, during the constant current period, the battery charges to about 70 percent of full charge, where the remaining 30 percent is charged with a constant voltage. The constant voltage charge stage is essential for maintaining good condition of the battery and to avoid performance decrease due to sulfation [70].

When input power sources are unavailable or insufficient to meet load demand, the battery will be discharged to compensate for the load shortfall. To protect the battery from being over charged and over discharged, there will be a mechanism to isolate the battery from the load. This could be a two-way switch between the battery and the load (or dc-bus), which is controlled by the main digital controller or the analogue comparator.

The power converter should provide charging current for the batteries and/or load simultaneously while extracting the maximum energy from the sources. Unfortunately, in the real world, the customer or installer may purchase a large solar panel, a large turbine, and a small battery. If the controller were to charge at the peak power, the battery would charge too fast and the lifetime of the battery would reduce, or an explosion could occur. What the controller must do is manage the needs of the battery and balance them with the peak power that can potentially be supplied from the inputs along with output load requirements. Thus, a maximum battery charge rate selector for different system battery capabilities should be equipped with the converter system.

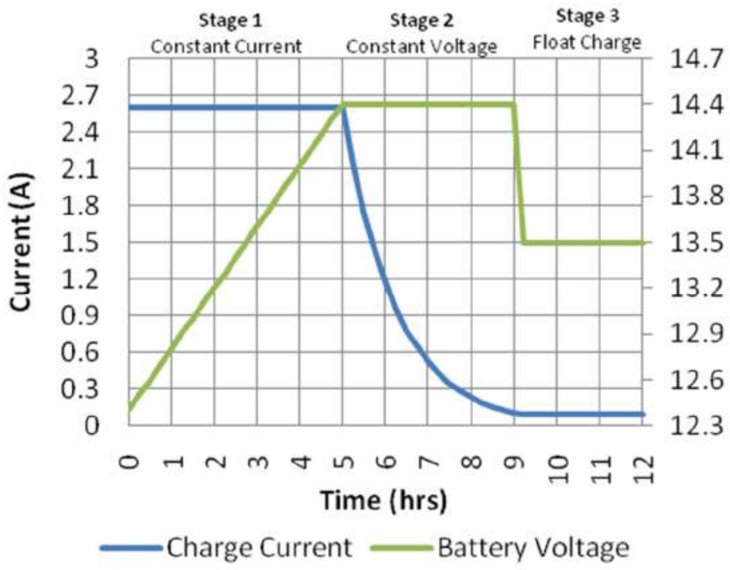

Figure 2-19. Lead Acid battery charge profile [69]

CHAPTER 3 DESIGN AND SIMULATION

3.1. SYSTEM SELECTION AND SPECIFICATION

As previously discussed on the topology and other functions that should be included in the target power converter, the full-bridge topology has been chosen. However, the style of the main power conversion control should be selected before going to detailed design. Thus, the comparison between microprocessor-based and PWM controller-based controllers is made to determine the most appropriate final solution.

For a microprocessor-based system, a high-end microprocessor should be used with its on-chip PWM, ADC and analogue comparator modules. It is able to implement complete digital control of such a MPPT dc/dc system. In order to control and balance the power flow from two input sources (including MPPT on each channel and battery charging control on the output) at a high switching frequency, a C2000 Piccolo microcontroller is a good choice [56].

Regarding a specialized full-bridge controller option, the LM5045 is selected as it has all the mentioned functions and it has integrated MOSFETs drivers [45]. The LM5045 PWM controller contains all of the features necessary to implement full-bridge topology power converters using either current mode or voltage mode control. This device is able to operate with an input voltage up to 100 V. The integrated gate drivers for the primary-side MOSFETs, and control signals for the secondary-side synchronous rectifier MOSFETs makes this controller more flexible for a range of designs. Besides this, the leading and trailing edge dead-time between the primary and synchronous rectifier control signals can be programmed by external resistors. In addition, there are many protection functions that are equipped in the controller, including cycle-by-cycle current limiting, hiccup mode restart, programmable soft start, synchronous rectifier soft-start, and a 2 MHz capable oscillator with synchronization capability and thermal shutdown [59].

Table 3-1. Comparing between control methods

	Microprocessor-based	**PWM controller-based**
Main controller	1 Microprocessors (C2000 Piccolo $8/unit)	2 LM5045 ($2/unit)
Converter topology	2 full-bridge	2 full-bridge
Input/output voltage range	Flexible	Flexible
Power rating	2 kW (1 kW for each input)	2 kW (1 kW for each input)
Number of power switches (MOSFET)	8 x BUK9611 (80 V, 75 A) ($0.65/unit)	8 x BUK9611 (80 V, 75 A) ($0.65/unit)
Number of	4 x STTH30R04 (400 V, 30 A)	4 x STTH30R04 (400 V, 30 A)

rectifying diodes	($1.5/unit) 3 MBR30H10 (100V 15A) $0.4/unit (3 phases rectifying)	($1.5/unit) 3 MBR30H10 (100 V 15 A) $0.4/unit (3 phases rectifying)
Sensing resistors	3 x CSS2725FTL500 0.5 mΩ, 4 W ($0.42/unit)	3 x CSS2725FTL500 0.5 mΩ, 4 W ($0.42/unit)
Inductors	2	2
Auxiliary power supply	Yes Cost: $2	Yes Cost: $2
Gate drivers	2 x LM5111 ($0.58/unit)	No
Isolated signal (for gate drivers)	4 x TPL2361 ($0.33/unit)	No
MPPT	Voltage buffers, current sensing buffers ($1)	Voltage buffers, current sensing buffers ($1)
		PIC16F1769: $1.1
Battery protection	Voltage buffers, comparators, current sensing buffers ($2) 2 x UPA2739T1A: 30 V, 85 A PMOS ($0.6/unit) Total cost: $3.2	Voltage buffers, comparators, current sensing buffers ($2) 2 x UPA2739T1A: 30 V, 85 A PMOS ($0.6/unit) Total cost: $3.2
Max. PWM frequency	120 kHz [57]	Programmable, up to 1 MHz
Output load response	Slow (Output voltage might jump to danger conditions)	Fast, self-regulate, cycle by cycle overcurrent protection
Soft-start	Yes (functioned in program)	Yes
Thermal shutdown	MCP9700 ($0.2/unit)	Yes
Programming efforts	High	Low
Risks that relates to microprocessors	Very high risk	Lower risk , able to work in CC or CV mode without microcontroller
Cost (excluding inductors, PCB)	$30.54	$24.96

Note:

- $ means USD
- Prices based on www.digikey.com and suppliers' website with an order larger than 5k units.

As can be seen from Table 3-1, the cost of the wholly microprocessor-based system is higher than that of the PWM full-bridge controller-based system. Also, there is much more programming effort for the wholly microprocessor-based control solution, and it is inflexible with regards to avoiding runaway of the flux core by using the cycle-by-cycle current limit method. Moreover, the wholly microprocessor-based control would require a lower PWM frequency which leads to an increase in the size of inductors, output filter elements and PC board compared to those of the full-bridge based controller system. For the cost, power density, flexibility, and safety of the converter, the integrated full-bridge controller is selected to be the primary controller of the converter.

Specifications for the converter are listed below:

- Two inputs:
    - 3 phase micro wind/hydro turbine (max 1 kW), input voltage range: 16 ~ 60 V
    - PV panel (max 1 kW), input voltage range: 16 ~ 60 V
- Max Output power capacity: 2 kW, 27 V
- Battery protection (overcharge current and over discharge, battery capacity is selectable)
- MPPT for all inputs
- Can work standalone or with a Lead-Acid battery for energy storage.

3.2. SYSTEM BLOCK DIAGRAM

Based on structural, functional and cost analysis, the block diagram of the MISO power converter system is formed as shown in Figure 3-1. As this power converter works in the range of low voltage (up to a maximum of 60 V), the full-bridge is configured by tying the input and output ground. This non-isolated full-bridge leads to the elimination of isolating devices, and therefore, reduces the converter's cost.

To choose the output LC filter, design the transformer, and to make any calculations that relate to the converter, the switching frequency must first be decided. Frequencies around 300 kHz can provide low switching loss and high efficiency at the price of slow transient response as larger capacitors and inductors are needed when compared to very high frequency switching [71]. On the other hand, converters with higher switching frequencies of around 1 MHz suffer from greater switching loss but offer faster transient response. As the converter to be used in the application of interest here is connected to a battery for most of the time, the transient response is not the highest priority. Therefore, the switching frequency of full-bridge controllers is intended to be set at around 300 kHz. With this range of switching frequency, transformers, inductors and capacitors are a reasonable size, and are of a relatively low cost.

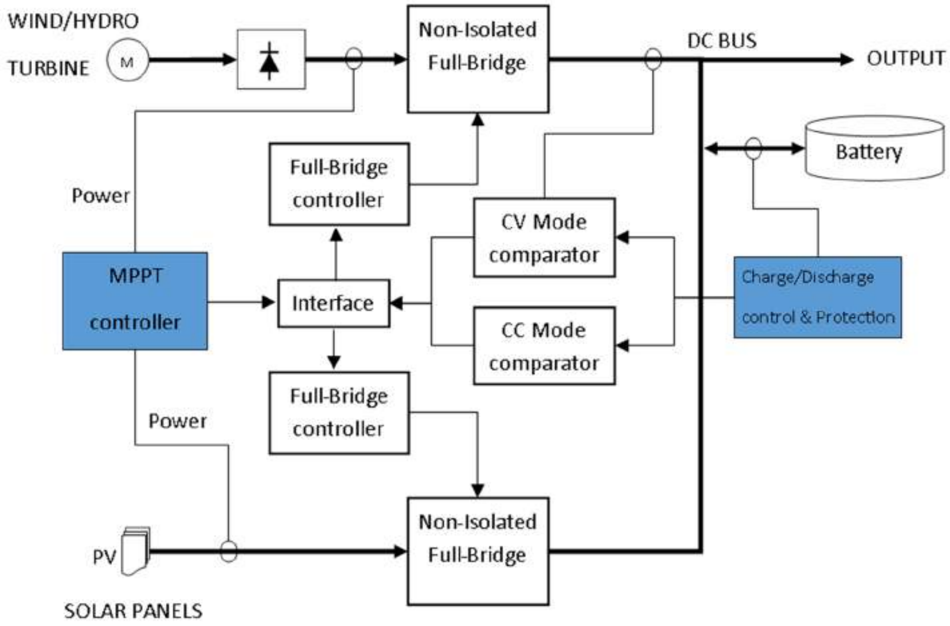

Figure 3-1. System block diagram

3.3. NON-ISOLATED FULL-BRIDGE DESIGN

The power conversion stage will be analysed with two secondary winding methods: the centre-tap configuration and full-wave-bridge configuration that is shown in Figure 3-2 [72].

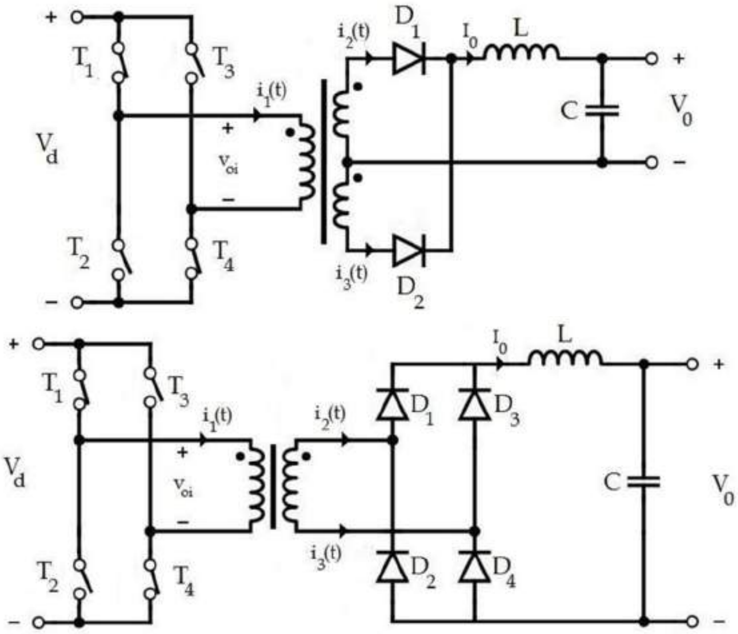

Figure 3-2. Full-Bridge topology with centre-tap configuration and full-wave configuration [72]

The bipolar switching used for the full-bridge converter operates the transistors in pairs. Transistors T_1 and T_4 are called as the first switch pair and the combination of T_2 and T_3 are named as the second switch pair. The output voltage V_0 is regulated and controlled by the PWM signal which is generated by comparing a saw tooth signal with a control signal (see Figure 3-3) [73].

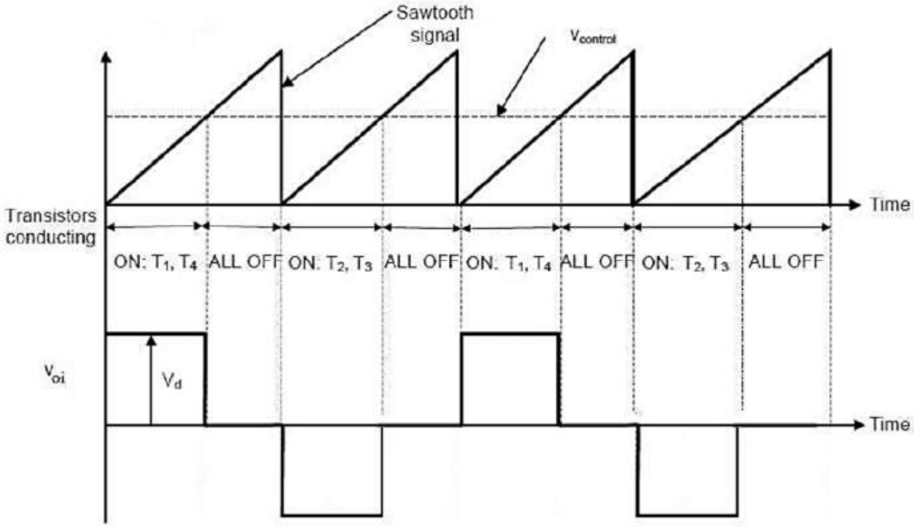

Figure 3-3. Switching waveform of the Full-bridge topology [73]

During the first half period, T_1 and T_4 are conducting as long as the saw tooth signal is lower than the control signal. When the saw tooth signal is higher than the control signal, the transistors stop conducting until the second half period takes place. From beginning of the second period, T_2 and T_3 turn on until the saw tooth signal again goes above the control signal. This process repeats continuously from period to period [72].

Figure 3-4 shows the current waveform on the primary and secondary side of the converter. The RMS current waveform can be expressed as [19, 74, 75]:

$$I_{1,RMS} = \sqrt{\frac{1}{2T_s}\int_0^{2T_s} i_1^2(t)dt} = \frac{n_2}{n_1} I_{o.max}\sqrt{D} \tag{1}$$

$$I_{2,RMS} = I_{3,RMS} = \sqrt{\frac{1}{2T_s}\int_0^{2T_s} i_2^2(t)dt} = \frac{1}{2} I_{o.max}\sqrt{D+1} \tag{2}$$

Where *D* is the duty cycle of PWM signal; T_S is the one time period of that switching cycle; n_1 and n_2 is the primary and seconday turns of the transformer.

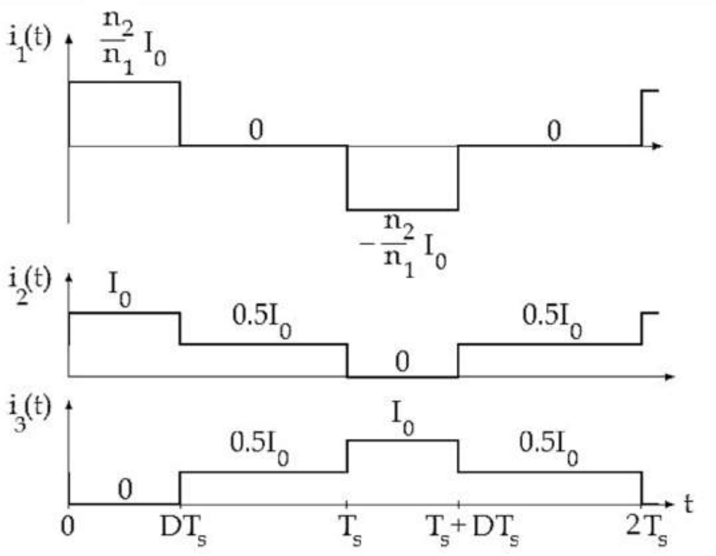

Figure 3-4. Primary and secondary current waveform

Thus, the output voltage V_O is correlated to the on time of the transistor and this association can be derived by integrating the voltage v_{oi} over one time period T_S and then divide it by T_S. The v_{oi} is then given by:

$$V_O = \frac{1}{T_s}\int_0^{T_s} v_{oi}(t)dt = \frac{1}{T_s}\left(2\int_0^{t_{on}} \frac{n_2}{n_1}V_d d(t) + \int_{t_{on}}^{T_s} 0.d(t)\right) \tag{3}$$

$$V_O = 2\frac{n_2}{n_1}V_d D \tag{4}$$

where

$$D = \frac{t_{on}}{T_s}$$

The transformer turns ratio for the converter can be:

$$\frac{V_O}{V_d} = 2.\frac{n_2}{n_1}D \tag{5}$$

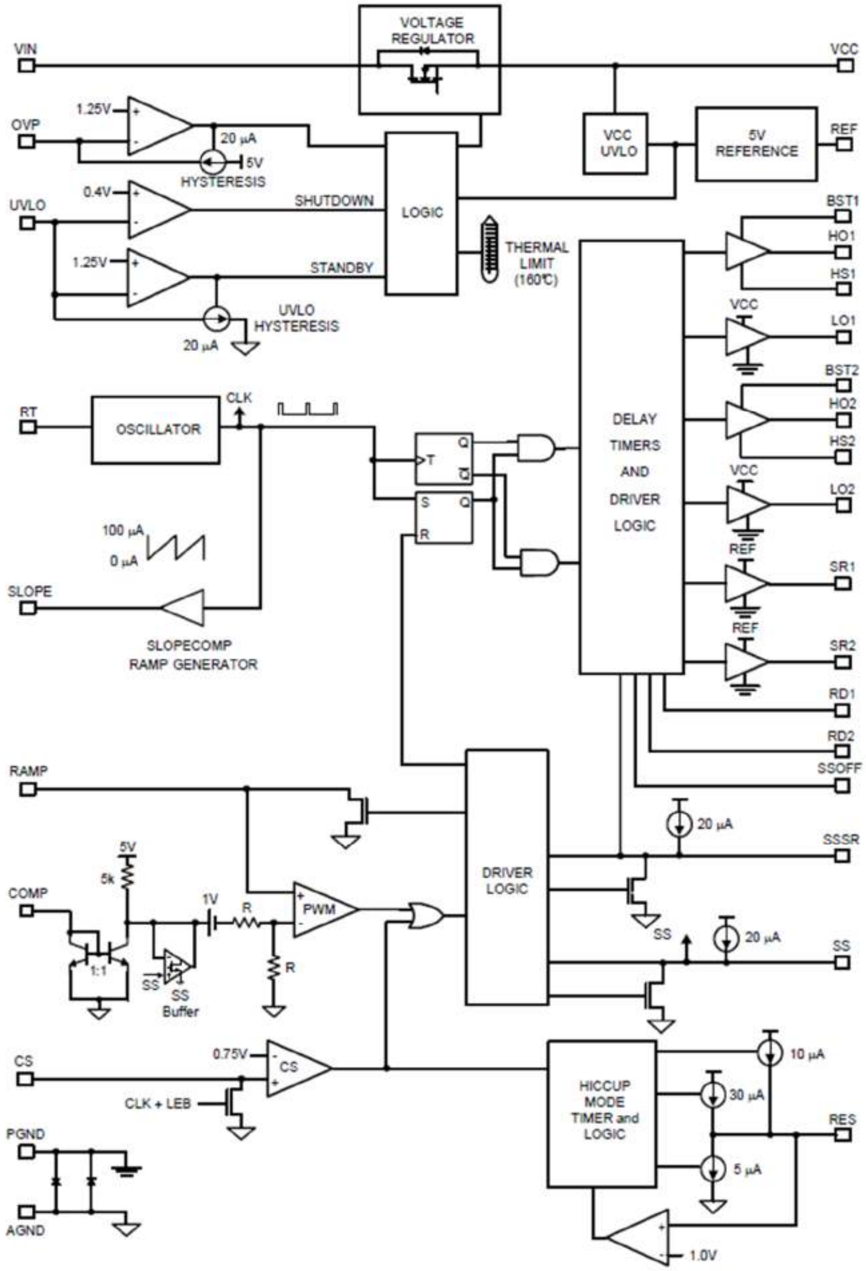

Figure 3-5. Block diagram of LM5045 [59]

Housed in a small package, LM5045 contains all the needed functional blocks for a full-bridge dc/dc converter (see Figure 3-5). There are four gate driver pins for primary switches, and along with two pairs of bootstrap and switching pins for the high-side switching power MOSFETs. The IC comprises two output pins (SR1 and SR2) for controlling secondary switches as synchronous switching is being employed for the rectifier. Beside main pins for power supply (VCC, VIN) and grounding (PGND, AGND) for power and analogue paths, various passive pins are equipped for setting the operation mode of the controller. By connecting external passive components to each pin (capacitor or resistor), the converter is ready to operate.

As can be seen in Figure 3-6, to set the maximum and minimum operating voltage for each input source, a chain of three resistors (R4, R13, and R21) is connected to OVP and UVLO pin. For setting the switching frequency to 300 kHz, a 27 kΩ resistor (R29) is connected to RT pin; the soft-start period is set by a capacitor connected to SS pin, the delay time between switching signal of the low-side and high-side is set by a resistor connected to the RD1 pin, the delay between switching signal of secondary to that of primary by a resistor connected to the RD2 pin.

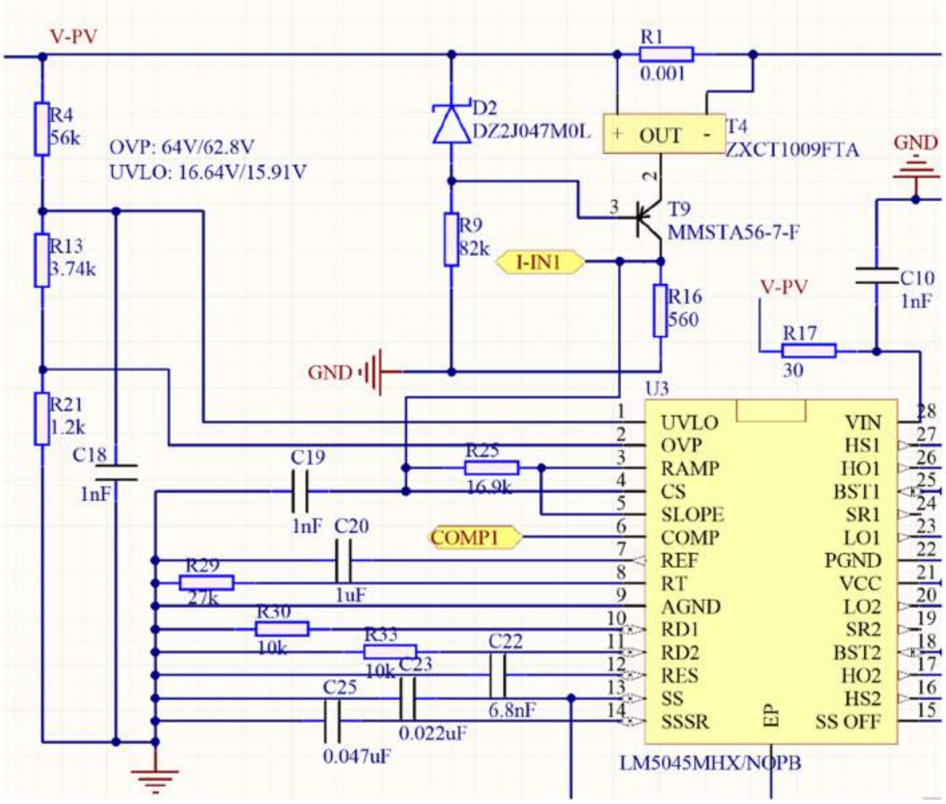

Figure 3-6. External components configuration for setting the operation mode of LM5045 in the converter

To set the converter operating on current mode, the SLOPE and RAMP pin are tied together and they are both linked to CS pin via a resistor. The configuration of feedback controlling pins (CS, SLOPE, RAMP, and COMP) allows the highest flexibility to the developer to establish the control method for the converter. Through interfacing via a current sink on the COMP pin with the duty cycle signal of the output PWM, this IC allows the use of a simple method to integrate two or more feedback control loops. Therefore, the requirement of integrating two input power sources into one combined feedback loop can be implemented. In addition, the control for MPPT on each channel is also facilitated by the use of this pin's function. The configuration and calculation of the interface circuits will be discussed in more detail in section 3.5.

For current sensing, a power resistor of 1 mΩ, 4 W is selected. At the maximum power operation and nominal input voltage, the input current is estimated to be 60 A, and therefore, the dissipate power on this resistor will be around 3.6 W. The current sense amplifier ZXCT1009 is used to convert the resistors' dropping voltage to a required voltage value that can be used by the full-bridge controller (see Figure 3-6).

As mentioned before, the power switching MOSFETs can be driven by the integrated gate drivers in the full-bridge controller. In fact, however, these blocks can generate a lot of heat which makes the controller become very hot during its operation. Additionally, the controller is surrounded by many external components for its operational configuration, therefore the power switches cannot be placed next to the controller. As a result, the long traces with high frequency and current from the controller to the switches could produce noises that interfere with other signals on the controller. For higher reliability of the system, external gate drivers are used in the system. This solution also allows flexible placement of control block and the power block during the PCB layout process, including the separation of the high-noise, the high-temperature area out of the sensitive regions.

3.4. TRANSFORMER DESIGN

The ratio of primary turns over secondary turns is determined by [19, 74, 75]:

$$\frac{n_1}{n_2} = \frac{(V_{d.min} - 2.V_{DSON})}{(V_o + V_{DSON})} D_{max} \tag{6}$$

Where $V_{d.min}$ is the minimum value of input supply voltage, V_{DSON} is the voltage across the Drain and Source of the power switches (T_1, T_2, T_3 and T_4), and D_{max} is the maximum allowed duty cycle that the converter can reach. For marginal design calculation, a worst case scenario is set at reaches 0.15 V and $Dmax$ is 85 %. The minimum input voltage $V_{d.min}$ is set to 16 V while the output voltage V_O is 27 V. Therefore:

$$\frac{n_1}{n_2} = \frac{\big(16 - 2(0.15)\big)}{(27 + 0.15)} 0.85 \approx 2 \tag{7}$$

At the possible highest value input voltage, the converter will run at its minimum PWM duty cycle. According this ratio, this value can be calculated by ($V_{d.max}$ is the maximum input voltage, and is expected at 60 V):

$$D_{min} = \frac{(V_o + V_{DSON})}{(V_{d.max} - 2.V_{DSON})} \frac{n_2}{n_1} = \frac{(27 + 0.15)}{(60 - 2.(0.15))} 0.5 = 0.227 \tag{8}$$

These values of duty cycle can be achieved by the controller and the gate driver, which confirm the appropriate ratio of the transformer.

Regarding power transfer capability of ferrite cores [74], the ETD39 ferrite core with the cross section A_e= 125 x 10^{-6} m^2 and N87 material is selected. Based on the basic equation of the transformer:

$$B = \frac{10^8.E}{4.f.A_e.n_1} \tag{9}$$

Where B is the flux density in teslas, E is the square wave peak voltage in volts, f is the frequency in hertz, A_e is the cross sectional area of the core in m^2, and n_1 is the number of the primary turns.

When determining the number of turns on the primary-side, it is vital to ensure that the core does not saturate. This number also determines the peak flux density in the core B_{max}. The value of n_1 is chosen to make sure B_{max} is below 1000 T within the expected range of input voltage [74, 75]. Thus, the number of primary turns will be:

$$n_1 \geq \frac{10^8.V_{d.max}}{4.f.A_e.B_{\max}} = \frac{10^8.60}{4.(300000).(1.25).(1000)} = 4 \tag{10}$$

From equation (10), n_1 is 4 and thus the number of secondary turns is 8.

The transformer works with a high switching frequency (300 kHz), and as such the skin effect must be taken into consideration. The skin-depth will be [74, 75]:

$$S = \frac{72.06}{\sqrt{f}} = \frac{72.06}{\sqrt{300000}} = 0.1316\ mm \tag{11}$$

The diameter d of wires used for the transformer windings should be less than two times the skin-depth [74], which means 0.25mm or smaller. Another option is to use Litz wire. In order to reduce the overall resistance (dc and ac) of the transformer winding, a parallel-connected bundle of 0.25mm (or thinner) wires or Litz wire are used. These parameters of the transformer were put into transformer design software (EPCOS Magnetic Design Tool) to confirm the copper winding size, ac and dc resistance, the core loss, and the operating temperature. The transformer is then assembled for the converter (see Figure 3-7).

The specifications of appropriate transformers for this power converter are:

- Core: ETD39 (39 mm x20 mm x13 mm), material N87;
- No air gap;
- Primary: 4 turns, secondary: 8 turns;
- Winding: 4 x parallel connected Litz wire (4 x 1 mm^2 = 4 mm^2 total cross sectional area).

Figure 3-7. The designed and assembled transformer

3.5. OUTPUT LC FILTER

Similar to many switching power supply, output voltage and output current need to be filtered. This can be done with a low-pass LC filter as shown in Figure 3-8. To keep the output current ripple within a specified limit, a sufficient inductor should be used. Typically, it is recommended to operate the circuit with a ripple current of less than 20% of the average inductor current [76]. To minimize size and cost of the output inductor, the maximum ripple is chosen to be 20% for this converter. The current wave form of the output LC filter is shown in Figure 3-9.

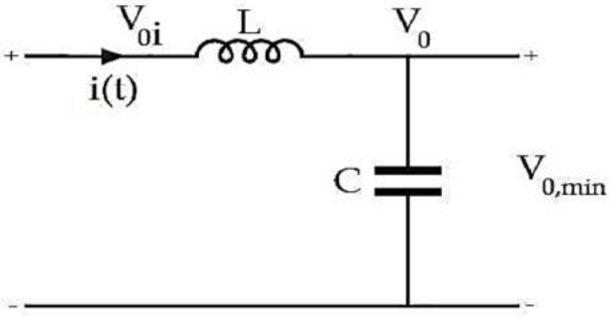

Figure 3-8. Output LC filter

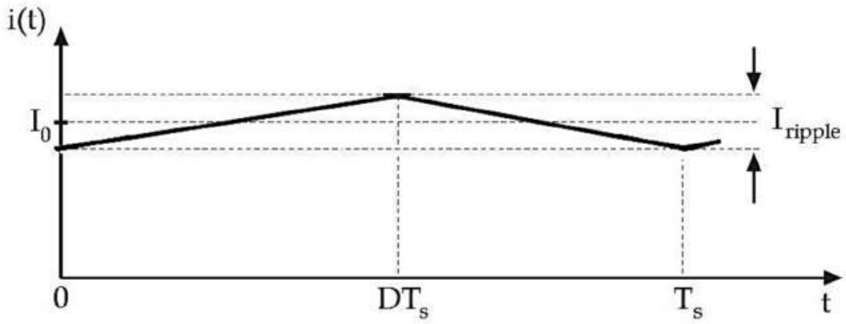

Figure 3-9. Output current wave form

The voltage over the inductor is given by:

$$V_L = L\frac{dI_L}{dt} \tag{12}$$

The inductance is then given by:

$$L = V_L\frac{dt}{dI_L} \tag{13}$$

The minimum inductor's value can be determined by the maximum voltage across the inductor ($V_{L,max}$).

$$L_{min} = V_{L.max}\frac{t_{on}}{I_{ripple}.I_{L.max}} \tag{14}$$

As seen in Figure 3-8, the voltage across the inductor can be given:

$$V_L = V_{oi} - V_o \tag{15}$$

where $V_{oi} = \frac{n_2}{n_1}V_d$

The maximum voltage across the inductor is calculated by:

$$V_{L.max} = \frac{n_2}{n_1}V_{d.max} - V_{o.min} \tag{16}$$

The on-state time of the switching transistors can be calculated by

$$t_{on} = D.T_S = \frac{1}{2}.\frac{V_{o.min}}{V_{d.max}}.\frac{n_1}{n_2}.T_S \tag{17}$$

The maximum average inductor current is given by

$$I_{L.max} = \frac{P_{o.max}}{V_{o.min}} \tag{18}$$

From equation (14), the lowest necessary value of the inductance is then

$$L_{min} = \frac{\frac{n_2}{n_1} V_{d.max} - V_{o.min}}{\frac{I_{ripple} . I_{L.max}}{\frac{1}{2} . \frac{V_{o.min}}{V_{d.max}} . \frac{n_1}{n_2} . T_S}} = \frac{1}{2} . \frac{n_1}{n_2} . \frac{1}{f} . \frac{\frac{n_2}{n_1} V_{d.max} - V_{o.min}}{I_{ripple} . I_{L.max}} \tag{19}$$

$$L_{min} = \frac{1}{2} . \frac{1}{2} . \frac{1}{300000} . \frac{2.(60) - 27}{0.2(\frac{1000}{27})} = 1.04\ \mu H \tag{20}$$

In order to calculate the needed value of capacitance, the following relation is used

$$I_C(t) = C \frac{dV_C}{dt} \tag{21}$$

The output current from the inductor is then going through the output capacitor, which produces the voltage ripple on the output voltage. For a high quality dc/dc converter, the output voltage ripple should be as low as possible. However, this leads to the increase in components cost. Normally, the output voltage ripple is ranging from 1 % to 2 % of the output voltage. The configuration of this power converter is that the output is normally battery connected, and therefore, the output voltage ripple is also chosen to be 5 % of the output voltage for cost reduction. The minimum value of the capacitor can be calculated as:

$$C_{min} = \frac{I_C(t)}{\frac{dV_C}{dt}} = \frac{I_{ripple} . I_{L.max}}{\frac{V_{ripple} . V_{o.min}}{t_{on}}} = t_{on} . \frac{I_{ripple} . I_{L.max}}{V_{ripple} . V_{o.min}} \tag{22}$$

$$C_{min} = \frac{1}{2} . \frac{V_{o.min}}{V_{d.max}} . \frac{n_1}{n_2} . T_S . \frac{I_{ripple} . I_{L.max}}{V_{ripple} . V_{o.min}} = \frac{1}{2} . \frac{27}{60} . \frac{1}{2} . \frac{1}{300000} . \frac{0.05.(\frac{1000}{27})}{0.2.(27)} \tag{23}$$

$$C_{min} = 2\ \mu F \tag{24}$$

3.6. INTERFACING CIRCUIT

As the different power sources (wind/hydro turbines and solar panels) have different characteristics, the interfacing circuit plays an important role in the converter. Containing three feedback control loops for each channel (constant output voltage, constant output current and MPPT), this circuit also shares the power flow between two different power source inputs. As can be seen from Figure 3-10, the interface circuit allows for two full-bridge controllers to be working simultaneously in three main modes: constant output voltage, constant output current and MPPT in each input. This is one of the most important blocks in the converter as it controls power flow from multiple inputs to a single output, allowing the integration of different modes to the full-bridge controllers without any disruption. By using analogue signals only, this block is capable of fast response, and is cheap and reliable.

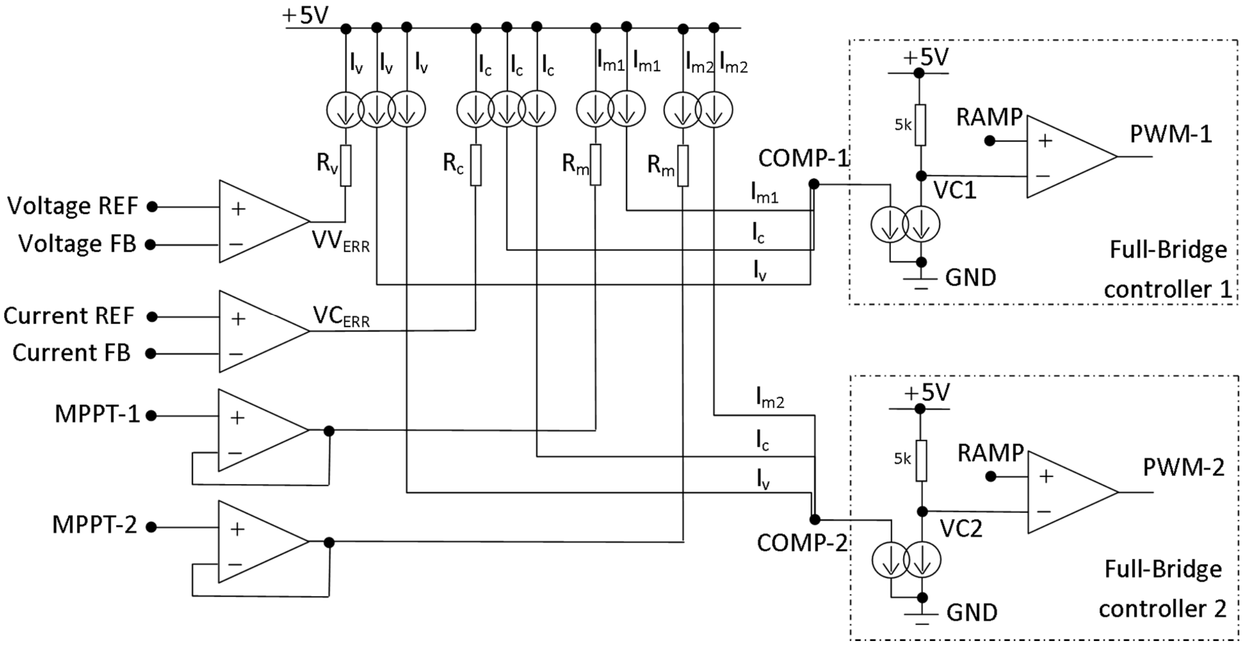

Figure 3-10. Interface circuit that allows integration of control loops into channels

With the current mirror structure shown in Figure 3-10, the integration of MPPT signals from the microcontroller to the full-bridge controller on each channel can be established. When the microcontroller desires either the PV or TB input, or both the PV and TB inputs to run in MPPT mode, the MPPT signal will override other feedback loop signals as the natural characteristic of the error amplifiers. For example, when the feedback value is lower than the reference value in MPPT mode as the input power is not enough to satisfy the output load requirements (including charging the battery). Thus, the value of the error amplifiers output jump to the highest possible value, and then the current from these loops that flow to the COMP pin is zero. Consequently, the MPPT signal sets the value of the PWM duty ratio on that channel with no effect from other control loops. This overriding rule is also true for the constant output voltage mode and constant output current mode. Depending on what condition occurs first, the other feedback signals will be overridden naturally.

As shown in Figure 3-10, currents into the COMP pins ($I_{COMP\text{-}1}$ and $I_{COMP\text{-}2}$) of the full-bridge controllers are calculated as shown in equation (25) and equation (26). Where I_v and I_c is the current generated by the voltage feedback loop and the battery charging current feedback loop, respectively; I_{m1} and I_{m2} is the current generated by MPPT signal of channel 1 (PV) and channel 2 (TB) respectively.

$$I_{COMP-1} = I_{m1} + I_c + I_v \tag{25}$$

$$I_{COMP-2} = I_{m2} + I_c + I_v \tag{26}$$

Via a current mirror with a 1:1 ratio that is set inside each controller, these currents create voltage values (V_{C1} and V_{C2} as calculated by equation (27) and equation (28)) that are compared with RAMP signals (saw-tooth signals) for setting the PWM duty ratios.

$$V_{C1} = 5 - 5000 * I_{COMP-1} = 5 - 5000(I_{m1} + I_c + I_v) \tag{27}$$

$$V_{C2} = 5 - 5000 * I_{COMP-2} = 5 - 5000(I_{m2} + I_c + I_v) \tag{28}$$

Clearly, V_{C1} and V_{C2} are inversely proportional to the value of current flowing to the COMP pin. In other words, the higher the currents into the COMP pins, the lower the duty cycle of the PWM signals. No current flowing into the COMP pin means the controller will run at maximum PWM duty cycle. From Figure 3-10, the values of currents are:

$$I_v = \frac{5 - VV_{ERR}}{R_v} \tag{29}$$

$$I_c = \frac{5 - VC_{ERR}}{R_c} \tag{30}$$

$$I_{m1} = \frac{5 - V_{MPPT-1}}{R_m} \tag{31}$$

$$I_{m2} = \frac{5 - V_{MPPT-2}}{R_m} \tag{32}$$

Where VV_{ERR} , VC_{ERR} is the output voltage of the error amplifier in CV and CC feedback loop, respectively; V_{MPPT-1} and V_{MPPT-2} is the output voltage of the MPPT control circuit for PV and TB input, respectively.

Then the voltage for determining the PWM duty cycle value on each full-bridge controller is (V_{C1} for PV and V_{C2} for TB input):

$$V_{C1} = 5 - 5000(\frac{5 - V_{MPPT-1}}{R_m} + \frac{5 - VC_{ERR}}{R_c} + \frac{5 - VV_{ERR}}{R_v}) \tag{33}$$

$$V_{C2} = 5 - 5000(\frac{5 - V_{MPPT-2}}{R_m} + \frac{5 - VC_{ERR}}{R_c} + \frac{5 - VV_{ERR}}{R_v}) \tag{34}$$

By choosing $R_m = R_c = R_v = 5k\Omega$, thus:

$$V_{C1} = (VC_{ERR} + VV_{ERR} + V_{MPPT-1} - 10) \tag{35}$$

$$V_{C2} = (VC_{ERR} + VV_{ERR} + V_{MPPT-2} - 10) \tag{36}$$

The result of this, from equation (35) and equation (36), is that the difference in output PWM duty cycle value of the PV channel from that of the TB channel is determined by the value of the MPPT voltage for each input from the MPPT block. As characteristics of the current error amplifier and voltage error amplifier, VC_{ERR} and VV_{ERR} will reach 5 V (power supply rail of the amplifiers) when their feedback voltages are lower than the reference values. This means that when the converter is operating in MPPT mode (input power is not enough for output load), the voltage value for generating the PWM output on each channel will be:

$$V_{C1} = V_{MPPT-1} \tag{37}$$

$$V_{C2} = V_{MPPT-2} \tag{38}$$

When the input power is more than sufficient to supply the required output load, the converter will change to CC mode or CV mode depending on which load condition is required (as determined by the battery state of charge). In the case of meeting the CC condition, the CV error amplifier output signal and MPPT values will be at the highest value of 5V. Thus:

$$V_{C1} = V_{C2} = VC_{ERR} \tag{39}$$

Similarly, when the CV condition is required, the value of V_{C1} and V_{C2} will be:

$$V_{C1} = V_{C2} = VV_{ERR} \tag{40}$$

The RAMP signals inside each full-bridge controller are the same (in terms of slope, amplitude, and frequency). Therefore, equation (39) and (40) shows that the PWM signals for both channels are the same in CC and CV mode. As a result, the amount of power from each input to the output will be dependent on the difference of input voltages. For example, if the input voltages on both channels (dc value) are the same, then the total input power is distributed evenly to the output. Theoretically (and practically), the channel that has the higher voltage from the power source will contribute more input power than its counterpart.

With the selected value of R_m, R_c, and R_v at 5kΩ, the currents that flows in each mirror traces are about 1 mA. Due to the availability of a current mirror structure integrated into a single IC package (BCM62), the full interfacing circuit can be designed (see Figure 3-11).

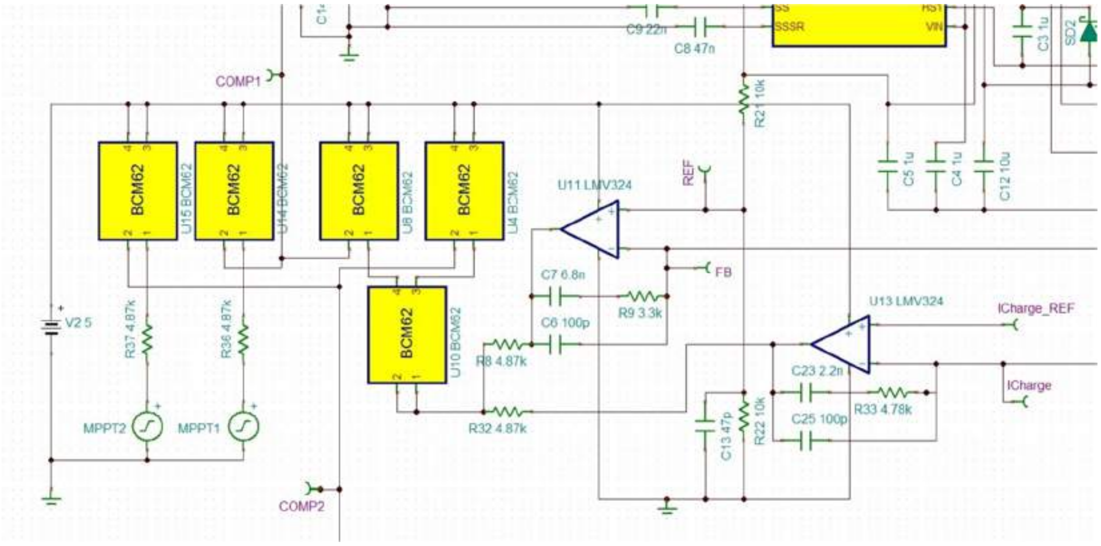

Figure 3-11. Interfacing circuit that allows two channels to work simultaneously in three modes: CC, CV and MPPT

3.7. MPPT ALGORITHM AND EMBEDDED PROGRAMING

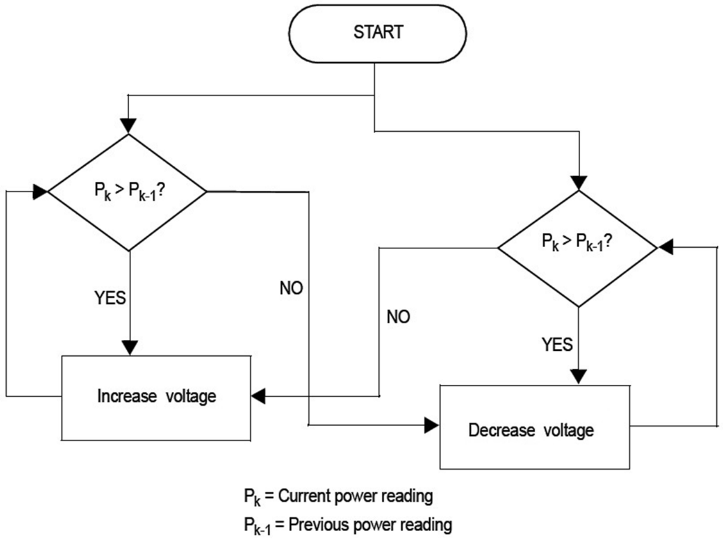

Figure 3-12. P&O algorithm

Two voltage values MPPT1 and MPPT2 (see Figure 3-11) for the input maximum power tracking from the solar panels and the turbine are generated by the microcontroller (PIC16F1769 is used owning to the low cost, and the number of ADC and DAC). The P&O algorithm was used in parallel for both types of input, see Figure 3-12. By periodically perturbing (either incrementing or decrementing) the input current of each energy source and comparing input power with that of the previous perturbation cycle to desire the next step. If the change in current increases input power, the control moves the operating point in the same direction. Otherwise, the operating point is changed to the opposite direction. In the next perturbation cycle, the algorithm continues in the same way.

An integrated development environment (MPLAB® X IDE) and a harware tool (PICkit3) was used for configuring, editing, compiling and building code, and programming and debugging the algoritm in the microcontroller for tracking MPP of both input channels. There are two analogue output voltage signals (MPPT-1 and MPPT-2) that are applied the interfacing circuit. Thus in total there are four analogue input signals (2 voltage and 2 current values) for the two input power sources that correlate to the two channels. Pin allocation and connection with the microcontroller is shown in Figure 3-13. For the PV source signals, current and voltage is assigned to pin 15 (analogue channel AN5) and pin 3 (analogue channel AN 3), respectively. These analogue values are converted to 10-bit digital code by the 10-bit ADC module. Based on the value of the input power and the controller's controlling step, the calculated output value of the MPPT (using the 10-bit data) is then converted back to an analogue voltage (MPPT-1) by a DAC module for interfacing with the full-bridge controller. However, there is no direct connection from the output of that converter to any identical pin of the microcontroller. Therefore, the integrated operational amplifier module (OPA1) of the microcontroller is used as a buffer for the DAC output. In this case, RC2 (pin 14) and RB4 (pin 13) are tied for the MPPT-1 voltage as shown in Figure 3-13. Similarly, the configuration for the Turbine channel uses pin 16 and pin 17 for inputs, and pin 7 and pin 8 for the output.

There is no need for a fast response to the MPPT outputs as the natural dynamic characteristics of input power to the sources are particularly slow (measured in multiple tenths of a second for wind turbine systems to multiple seconds for PV systems). For example, MPPT-1 can be adjusted to the MPP of PV panels in about 2 s or longer in order to adequately compensate for the sun moving or clouds obscuring the sun. Therefore, the input power sample rate was set at 60ms for each step of calculation in the P&O algorithm. This timing is done by using the Timer3 interupt of the microcontroller when it overflows. For cutting down cost and reducing power consumption of the microcontroller, the system clock is therefore set by its internal clock to just 2 MHz.

As the overall converter has many modes of operation, the microcontroller needs to be able to detect whether it needs to be in MPPT mode or in standby. Thus, the value of dc-bus is measured by the microcontroller. The dc-bus feedback voltage is connected to input AN9 (pin number 9) of the microcontroller. When either a PV or TB input is present, the microcontroller will activate MPPT if the feedback voltage is lower than its preset value. That means MPPT mode is activated when the input power is not sufficient to meet the output load requirements. This is because neither the CC or CV loop signals indicate that enough power is being supplied.

There are five analogue voltage inputs to be read while there is only one ADC in the microcontroller, so an intergrated multilexer inside the microcontroller is used. These input values are converted one by one in sequence, and each conversion needs a certain amount of time (time for charging the holding capacitor, and time for the analog to digital conversion). Values of inputs are not taken at the same time, and therefore the accuracy of the calculation results are reduced. The converter operates at high current and high frequency, so these inputs also have a significant amount of coupled noise that have an effect on the accuracy of individual input readings. To overcome this sort of noise issue, all input signals are sampled and converted three times and then averaged to provide the final value of each input.

The coding for this microcontroller has been done in C language (refer to Appendix I. MPPT coding for the microcontroller for details).

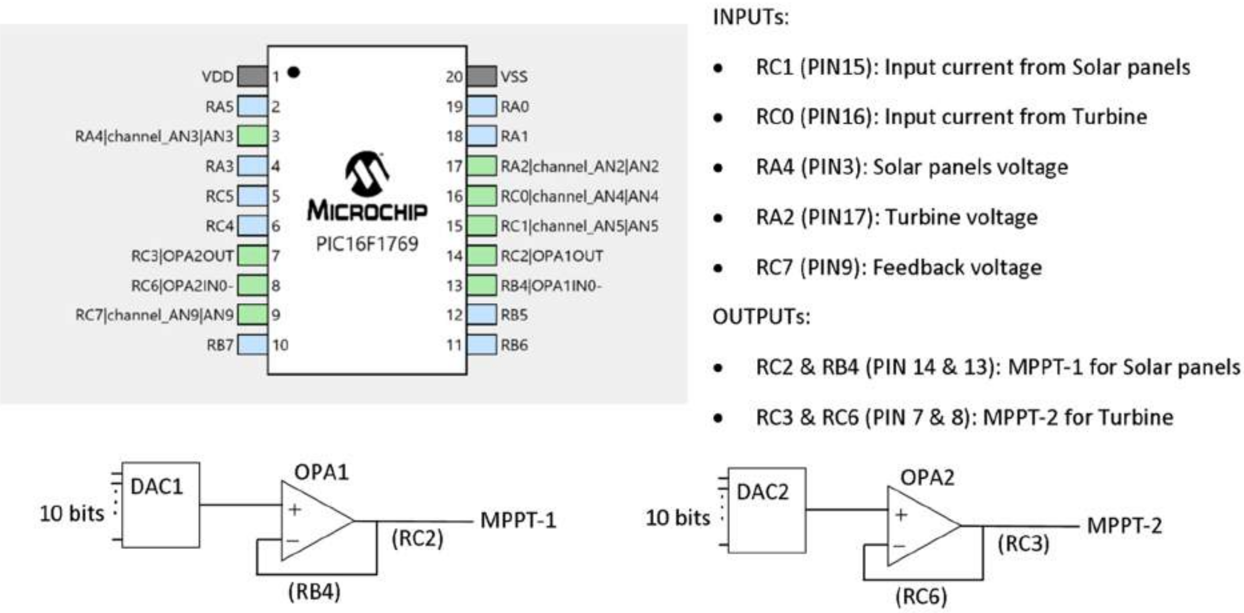

INPUTs:

- RC1 (PIN15): Input current from Solar panels
- RC0 (PIN16): Input current from Turbine
- RA4 (PIN3): Solar panels voltage
- RA2 (PIN17): Turbine voltage
- RC7 (PIN9): Feedback voltage

OUTPUTs:

- RC2 & RB4 (PIN 14 & 13): MPPT-1 for Solar panels
- RC3 & RC6 (PIN 7 & 8): MPPT-2 for Turbine

Figure 3-13. Pin allocation and connection of the microcontroller for MPPT

3.8. BATTERY CHARGING AND PROTECTION CIRCUIT

As can be seen from the system block diagram (Figure 3-1), the dc-bus voltage and the battery voltage are the same during charging and discharging. To control the power flow (charging and discharging the battery), the circuit as shown in Figure 3-14 is proposed. Here, T1 (a P-channel MOSFET, 40 V, 110 A, SUM110P04 is selected) and a comparator (LM324) linked to the battery's critical voltage (the lowest allowable level of battery voltage) are used. When the battery voltage is lower than Critical REF, the comparator will turn off T1. Once there is enough source power to raise the dc-bus voltage, in the first instance the body diode of T1 will forward bias and conduct, and slowly start charging the battery. Once the bus voltage rises enough, the comparator output will reverse, automatically turning T1 back on which reconnects the battery to the dc-bus and enabling normal battery charging to occur.

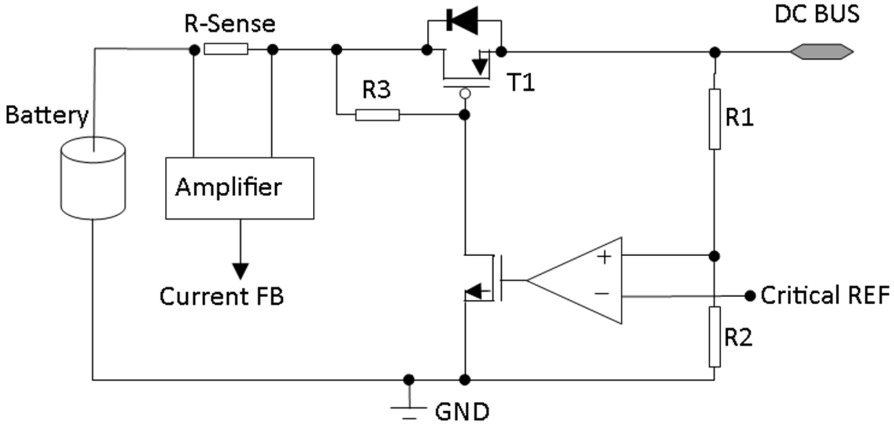

Figure 3-14. Battery protection and battery charging current amplifier

An analogue scheme was proposed for battery charging and discharging. Figure 3-15 shows the feedback circuit that includes MPPT, charging current, and the regulated output voltage (dc-bus) into the main feedback loop of the full-bridge controller. This circuit permits the full-bridge controller to work at MPP, and regulate the output voltage at the required values (depending on which phase of charging the battery is in). The output voltage of the converter is essentially set by Rfb1, Rfb2 and R5; the maximum charging current is set by the resistor chain (R1 – R4) with mechanical switches K1-K3 allowing variation of the voltage divider voltage, which are set by the user. The switch state of K1-K3 will set the value of I-Charge-Ref voltage which is used for defining the constant current charging value and the threshold of changing from constant voltage to float charging. The threshold for float charging is set by the ratio of R6 and R7, which is normally around 10 % of the constant charging current [68]. When the charging current is higher than this value, T2 is turned on and R5 is paralleled with Rfb2 which leads to a higher value of regulated output voltage (28.8 V – constant voltage charge mode). On the contrary, when the charging current is lower than that threshold, the converter regulates its output voltage at 27 V (float charge mode).

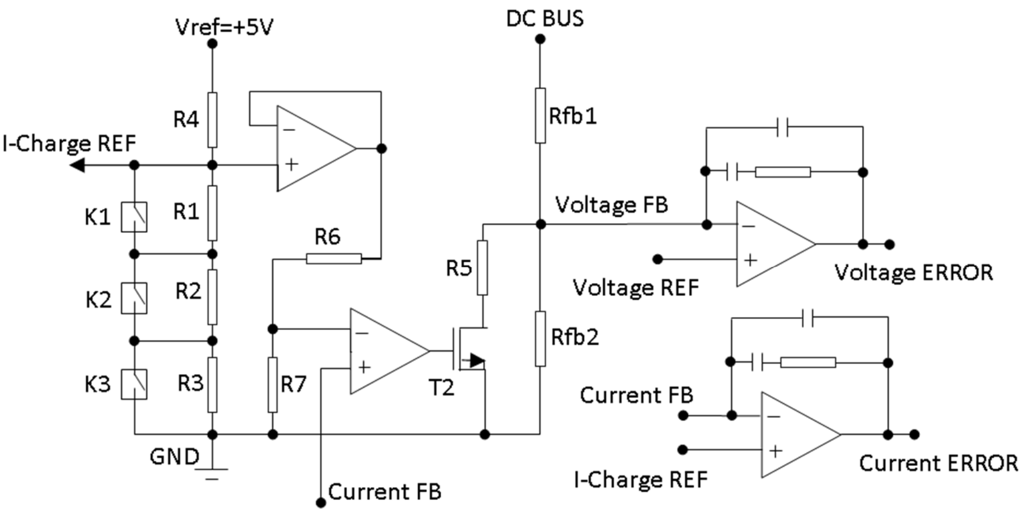

Figure 3-15. Setting charging current and Feedback loops configuration

The overall power converter should provide charging current for the batteries and/or load simultaneously while extracting the maximum energy from the sources. However, a customer or installer may purchase a large solar panel, and/or a large turbine, and a small battery. In this situation, if the converter were to charge at the peak power possible, the battery would charge too fast and the lifetime of the battery would degrade, or an explosion could occur. What the controller must do is manage the needs of the battery and balance them with the peak power that can potentially be supplied from the inputs along with output load requirements. Thus, a maximum battery charge rate programming circuit for different system battery capabilities is implemented (see Figure 3-15) where the maximum charge current is set via the chain of three switches (K1-K3). By selecting the right position of the switches according the battery capacity, there are eight levels of maximum charging current that can be set.

Figure 3-16 shows the designed schematic of the battery control blocks as well as the feedback circuitry. Controlling battery charging and discharging can be done by three comparators and three switches to adjust the level of feedback pin voltage for two charging voltages levels and setting the maximum charging current with three-switch selector.

Following the charging profile shown in Figure 2-19, the controller circuit automatically selects the charging state depending on the value of the battery voltage and the charging current. When the battery voltage is lower than 28.8 V and the charging current is larger than 10 % of the set maximum current, the converter runs in the constant current charging mode. This is due to the mismatch of the feedback voltage and the reference voltage. The constant output voltage loop tries to increase output current as much as possible to regulate its output voltage at 28.8 V. However, the constant current loop will take over when the charging current reaches the set point, and therefore, only delivers the fixed current amount (Stage 1: constant charging). During this stage, the battery voltage increases slowly until it reaches 28.8 V. This is the point where the constant voltage feedback loop is activated to regulate the battery voltage. When the battery voltage is held at 28.8 V, the battery charging current drops gradually (Stage 2: Constant voltage). This charging current continues to decrease in this constant voltage charge mode. When this current drops to lower than 10 % of the set maximum charging current, comparator 3 (see Figure 3-16) is activated to adjust the value of the feedback resistor chain for shifting the regulated output voltage to 27.2 V (Stage 3: Float charge).

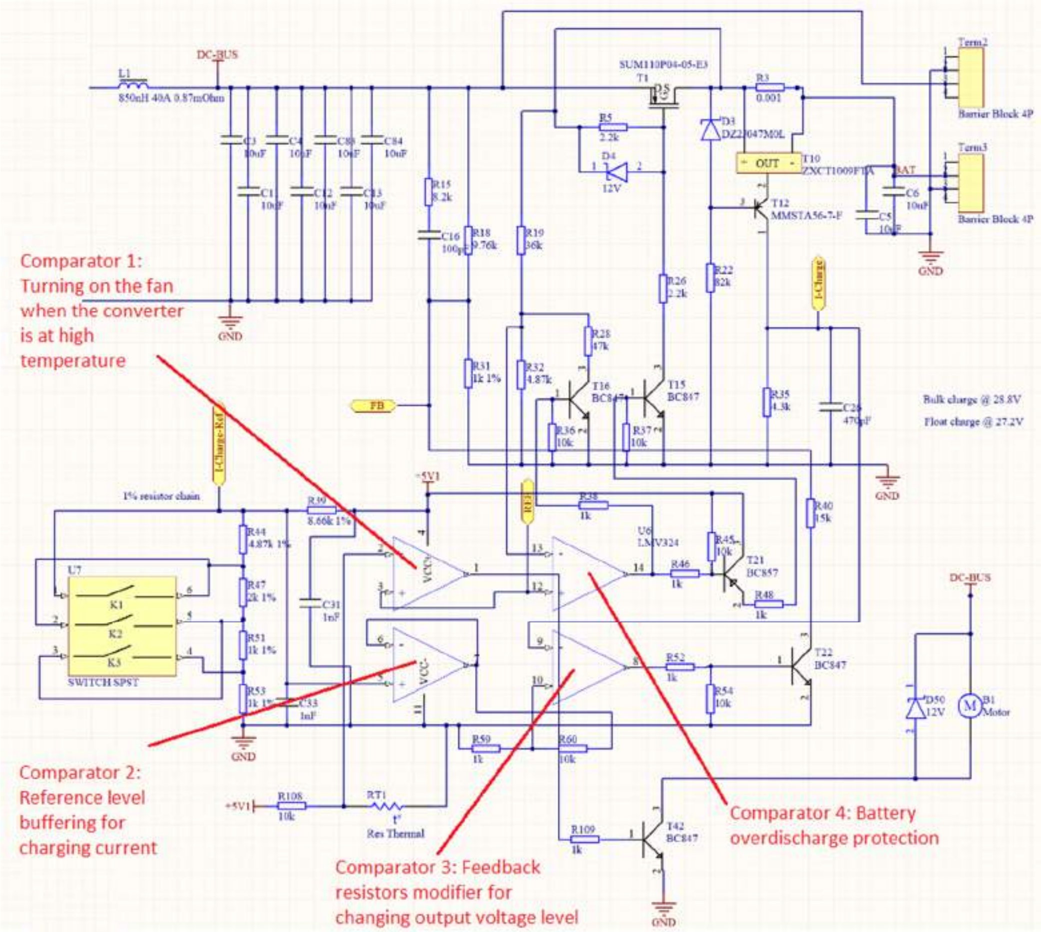

Comparator 1: Turning on the fan when the converter is at high temperature

Comparator 2: Reference level buffering for charging current

Comparator 3: Feedback resistors modifier for changing output voltage level

Comparator 4: Battery overdischarge protection

Figure 3-16. Battery charging/protection circuit

The battery protection circuit controls switch T_1 (Figure 3-16) to turn on when the battery voltage is in a safe voltage range and turn off when the battery voltage drops to its critical level (over discharge). This is done by the function of comparator 4 and the appropriate setting of the three mechanical switches (see Figure 3-16). While T_1 is off, if a power source is available, the battery is charged via the body diode of T_1 until the battery voltage reaches the safe zone where the comparator turns T_1 on again.

There is an optional block for automatically turning on/off the fan based on the converters' temperature. There is one available comparator out of four comparators in a LM234 chip (three of them have been used for buffering charging current, battery protection, and modifying output voltage level). Thus, this block is formed by adding a negative temperature coefficient resistor, a small NPN transistor, and appropriate resistors.

3.9. SYSTEM SIMULATION

In the design process, the connection of circuits is made in a schematic capture software tool and then transformed to a netlist file for simulation to confirm basic operational characteristics. TINA-TI (Toolkit for Interactive Network Analysis – Texas Instruments) has been used owning to its availability. Before full system connections are formed, each functional block is designed and simulated separately. Along with integrated models of basic devices such as resistors, capacitors, and transistors in the software, the SPICE models of third-party components are acquired and compiled into TINA for simulation. See Appendix A. SPICE model of LM5045, Appendix B. SPICE model of LM324, Appendix C. SPICE model of the transformer, Appendix D. SPICE model of BCM62, Appendix E. SPICE model of LM5110A, and Appendix F. SPICE model of the current sense amplifier (ZXCT1009) for details.

It is not possible to integrate a microcontroller and its source code into the TINA simulation environment, so the MPPT mode is simulated with its output preset voltages to see how the MPPT interacts with other modes via the interfacing circuit. Fortunately, this issue will not affect the converter’s hardware configuration after the PCB is fabricated. The MPPT algorithm and program can be adjusted and modified when the microcontroller is mounted on board. The converter’s simulation schematic is shown in Figure 3-17 that includes all the main functional blocks. Simulations were run by this schematic to confirm the operation of the system, such as start-up response, output load response, and switching between operation modes.

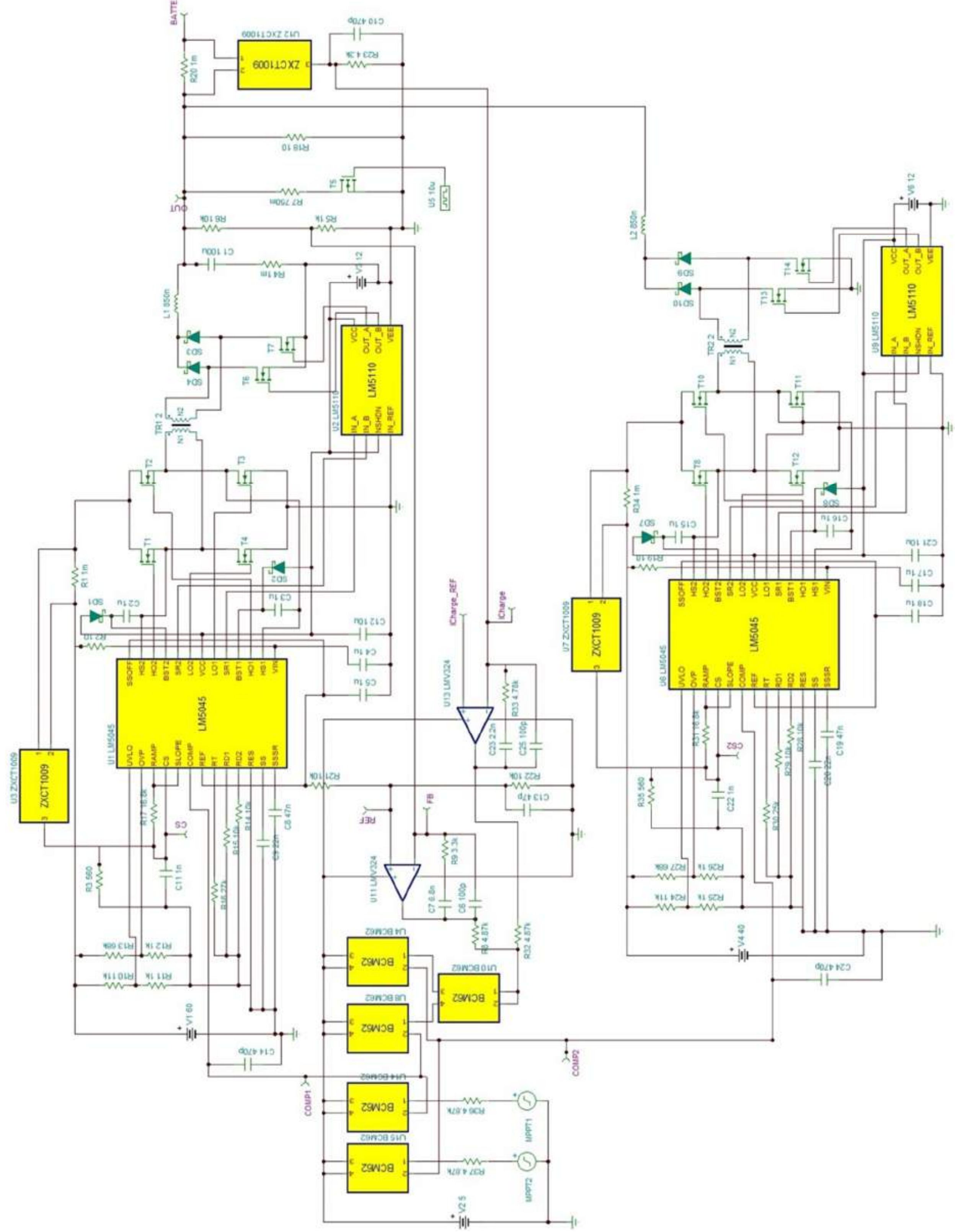

Figure 3-17. Simulation circuit in the TINA-TI environment

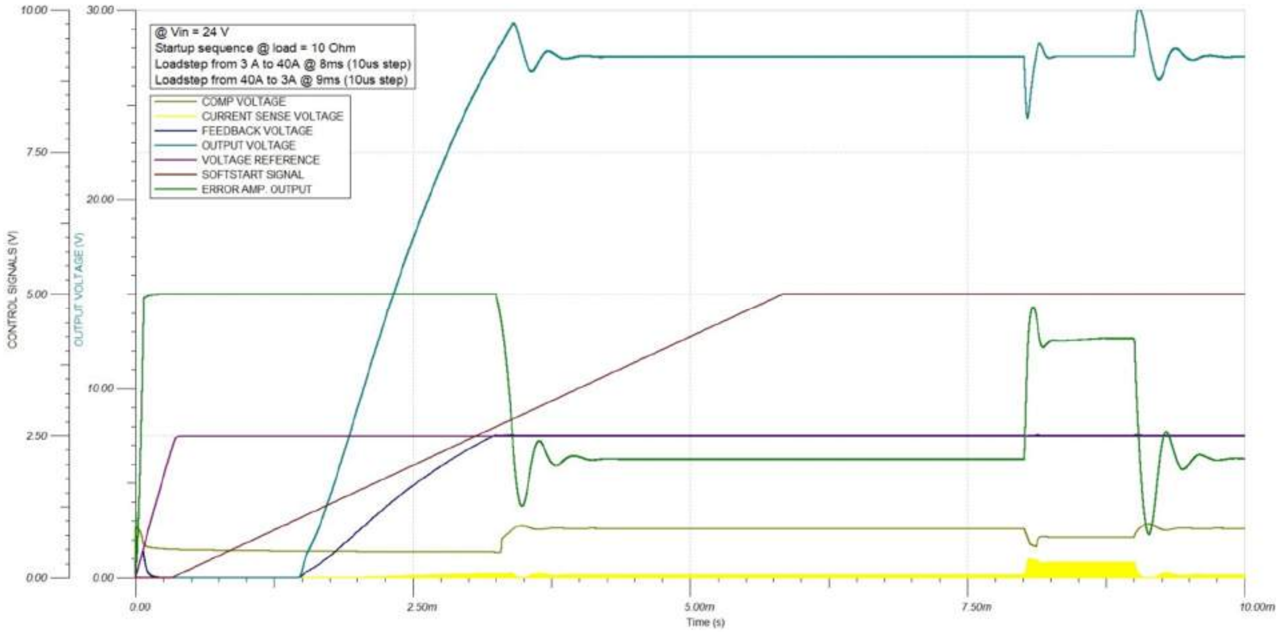

Figure 3-18. System simulation results: start-up sequences and load step response of the converter

As can be seen from Figure 3-18, the converter response to power up and step changes in the load are simulated. When both the input power sources from both sources (that is, both channels) are stepped up from 0 V to 24 V at the beginning of the simulation (0 ms) and the output is connected to a 10 Ω resistor as load with no battery, the converter takes about 3 ms for the output voltage to reach the set dc-bus value (the Light Blue line). At the beginning, as the feedback voltage (the Dark Blue line) is lower than the reference voltage (2.5 V), the output voltage of voltage error amplifier (the Green line) is at the maximum level (5 V). Hence, the output PWM signals will be generated at their maximum duty cycle, and the converter will be moving to produce the maximum output current. However, the soft-start block is activated by the soft-start voltage (the Maroon line) which is increasing slowly. Therefore, the output current rises gradually on each PWM cycle, which leads to the slow increase in output voltage. Nevertheless, there is some ringing before the output voltage is regulated at 28.5 V. This is because the value of the soft-start capacitor is smaller than needed for slowing down the output voltage when powering up the converter. Although a bigger capacitor can be connected to the SS pin to solve this issue, this simulation result is kept for demonstrating the behavior of the converter. When the output voltage exceeds its desired value and goes up to nearly 29 V, the output of the voltage error amplifier drops rapidly to nearly 1 V and there are no PWM signals to the power switches. Consequently, there is no current flowing to the output and the output voltage drops to about 27 V. The voltage of error amplifier output continues to adjust until reaching the stable value according to the output load. Once the level of the error amplifier is regulated, the output voltage (dc-bus) is stable.

When applying a step load change from about 3 A to full load (40 A) at 8 ms, the output drops to 25 V and takes approximately 0.25 ms to recover. This is the time it takes for the control loop error amplifier output voltage to reach its new level. In this high load condition, from 8ms to 9ms of the simulation time, the increase in the current sense peak voltage (the Yellow line) and the decrease in the voltage of the COMP pin (the Brown line) are also recorded. At 9 ms of the simulation time, the output load is reduced rapidly from full load to a light load condition (40 A to about 3 A), the output voltage of the converter jumps to nearly 30 V and takes 0.5 ms to return to normal level.

When the input voltage of power sources are set to the higher values (60 V for example), the load transient is much better (smaller drop and overshoot, quicker response time); however, the overshoot at start up goes up to nearly 30 V. In the other direction, there is no overshoot at start up when the inputs are set lower than 20 V.

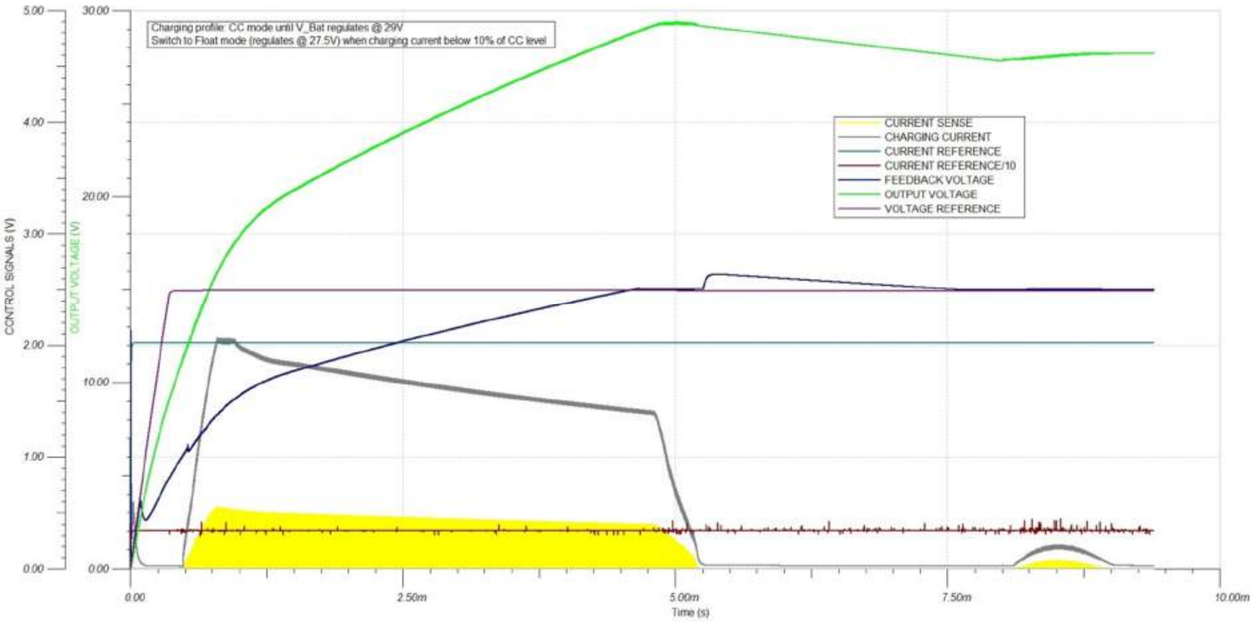

Figure 3-19. System simulation results of battery charging profile: CC mode --> CV mode --> float charge mode

The battery charging profile is shown in Figure 3-19, which contains the three stages of charging: constant current, constant voltage and float charge. In order to simulate this profile, a simple model of a lead-acid battery (comprising of a large capacitor – 0.1 F - that is connected in series with a voltage source – 20 V - and a small value resistor - 10 mΩ) is connected to the output of the converter. Thus, the charging time is much shorter than in a real battery and it is just suitable for simulation, where the changes between charging modes are displayed. As shown in Figure 3-19, the Green line (the battery voltage) increases from 0 V to 29 V in 4.9 ms while the charging current is varied through several stages (the Grey line – charging current feedback signal). After a certain time for the starting up of the system, the charging current increases quickly to the constant current charging level (at about 1 ms) and it is kept at that level after about 250 µs (the Grey line – charging current feedback is equal to the current charging reference setting level – the Light Blue line). The charging current is then reduced slowly until the output voltage (battery voltage) reaches the constant voltage charging level of 29 V. The converter then regulates the output voltage at that value in about 500 µs, representing constant voltage charging. While keeping the output voltage constant, the charging current decreases until the charging current signal is lower than the Current Reference/10 voltage (the Maroon line). From this moment, the converter turns off its switches and waits for the battery voltage to fall down to 27.5V (in about 2.5 ms) to continuously regulate at this level (float charging mode). During the two constant voltage regulation periods (constant charging voltage and float charging mode), the level of feedback voltage (the Dark Blue line) and reference voltage (Purple line) are equal.

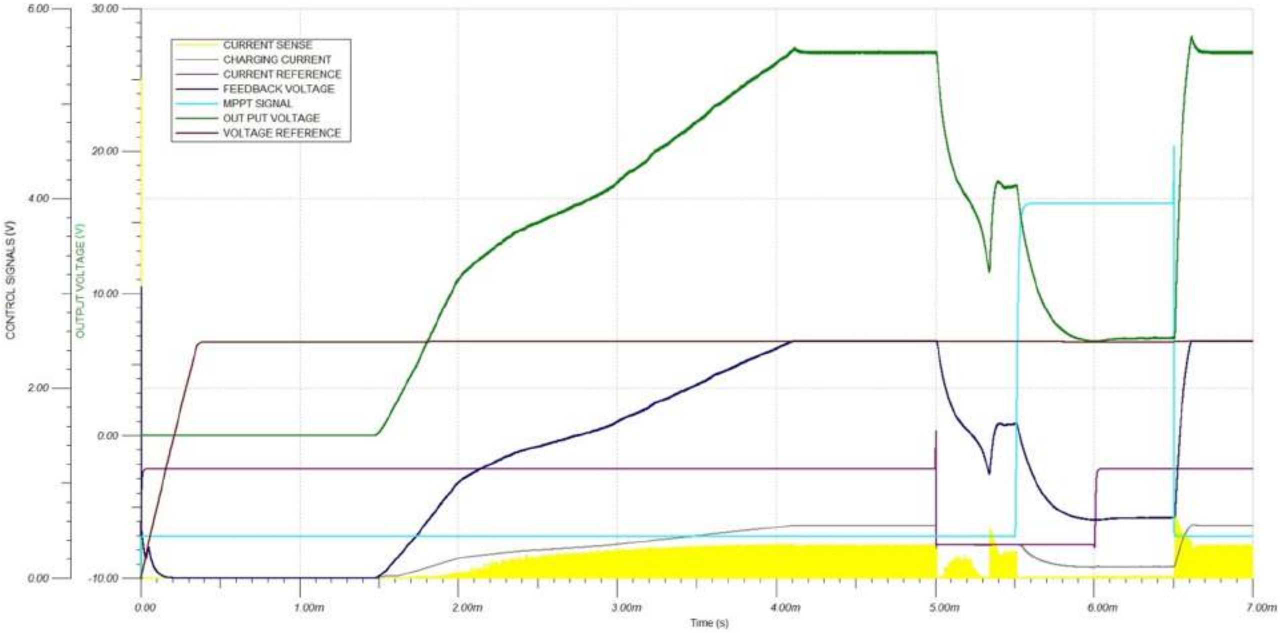

Figure 3-20. The simulation results of changing between operational modes of the converter (CC, CV and MPPT)

The switching between operation modes (MPPT, CC, and CV) of the converter is shown in Figure 3-20. The simulation is conducted with the PV channel, where the input voltage is set at 24 V and the output load is a 2 Ω resistor. From the beginning of simulation to 5 ms, the converter is set at CV mode by fixing the charging current reference (the Purple line, at 1 V) higher than the current feedback voltage (light load at the output – the Grey line), and MPPT voltage at low level (the Light Green line, at 0.5 V). As shown in the figure, the converter increases its output voltage (the Green line) to the regulated value in about 4 ms. The CV mode starts at 4.1 ms and lasts nearly 1ms until the current reference is set to a lower value (0.5 V) at 5ms. When the current feedback is higher than the current reference voltage, the CC mode is then activated and the CC feedback loop takes about 300 μs to reach its stable level. During this short period, the value of current reference voltage and the current feedback signal are the same. As the output current is regulated at about 8.5 A, the output voltage is maintained at about 17 V only.

From CC mode, the MPPT mode is activated by rising MPPT voltage from 0.5 V to 4 V at 5.5 ms of the simulation (see the Light Green line in Figure 3-20). The output current is then reduced to about 3 A after 0.5 ms and maintained at that value afterward. At 6.5 ms, the MPPT signal is set back to 0.5 V and the converter turns back to CV mode. The simulation results show that the converter is able to move quickly between operation modes.

CHAPTER 4 PCB DESIGN

4.1. SCHEMATIC AND MATERIAL

After simulations adequately indicated desired function could be achieved, the schematic of the converter was designed using the Altium Designer software tool (see Figure 4-1). The list of materials (components) is also generated by the tool, see Appendix G. Converter build-in material list. By achieving about $55 of the total components cost, the converter should be a low-cost in regard to its power capability and functions.

4.2. PCB DESIGN PROCESS

The converter contains both analogue and digital signals at high frequency and high current that can couple noise to the output and other functional blocks on the board. There are a lot of sensitive signals that can be adversely affected by noise, for example, the feedback and reference voltage on the constant voltage loop, and the reference voltage and feedback voltage for the current loop. Therefore, the design of the PCB will greatly affect the converter operation. The PCB design for this converter was divided into three main steps. Firstly, board floor planning followed by layout and placing of components for each functional block was made. After that, traces in each block were routed with the priority from power and ground, sensitive signal, high current, to ordinary signals. The interconnection between functional blocks is included in this phase. Finally, the design was checked and verified with standard design rules from the PCB manufacturer.

Board floor planning was performed at the beginning of the PCB design process for defining the location of each functional block and components before routing any traces. The main switching groups (including primary power switches, transformer, secondary freewheel diodes, and output LC filter) of the PV and TB channels are arranged in parallel across the board. The microcontroller for MPPT is placed between two channels that close the power supply. Two full-bridge controllers are located in the middle of the board where they work in placement conjunction with the switching transistors, the microcontroller, and other blocks. Analogue blocks and components are placed farther to the output side of the board. With this arrangement, the high-speed logic and high-power switching components have less chance to interfere with other signal traces. It is important to note that the main current loops and digital signals should be located away from analogue circuits, low-speed signals, and connectors. The placement of heat sink devices was conducted during this stage as well.

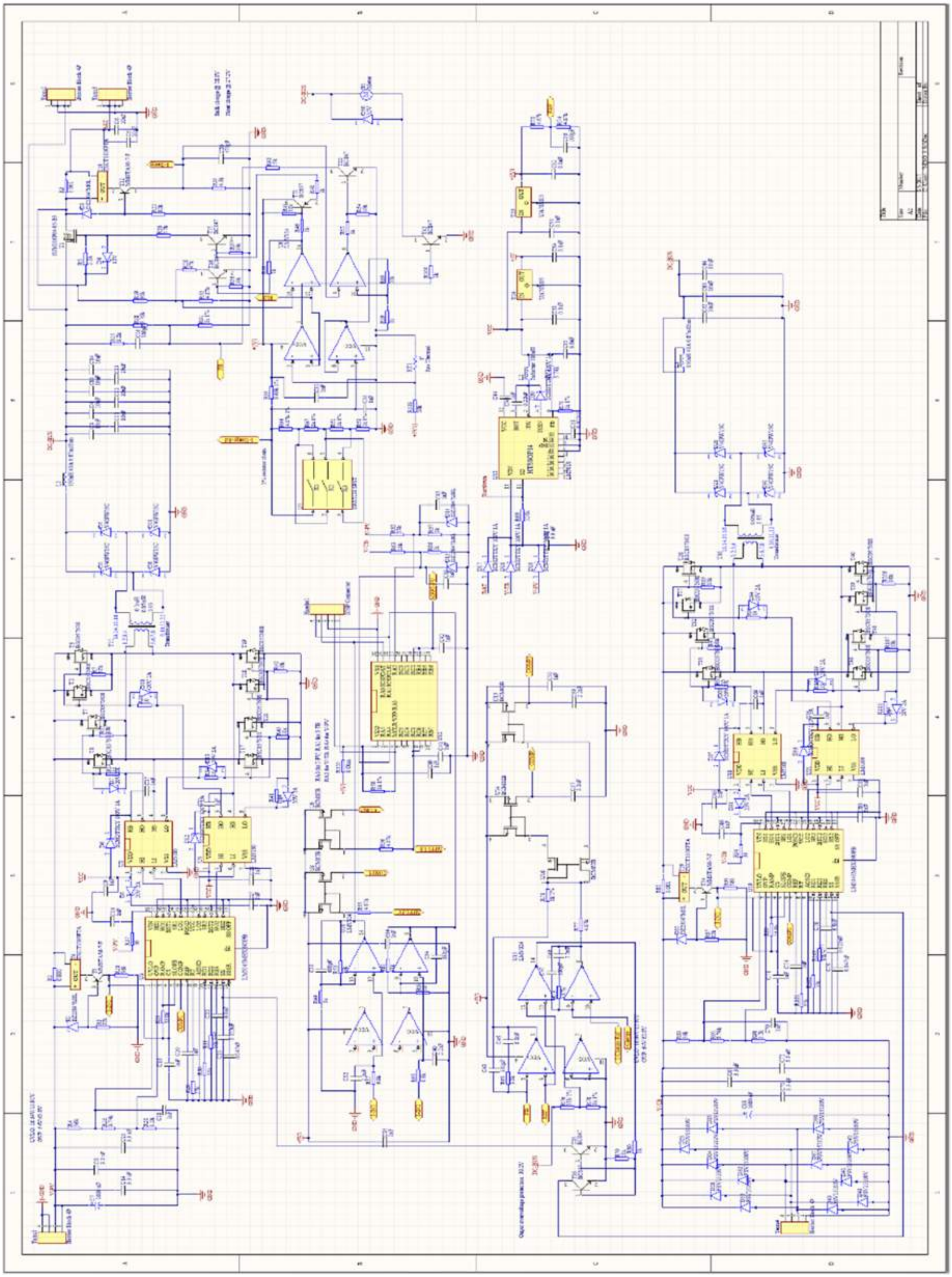

Figure 4-1. Schematic of the converter

Trace routing was manually implemented after all the components of the converter were positioned. The power traces were routed with the highest priority to be as short and wide as possible for the lowest impedance. The grounding on the board was also taken into special consideration. The digital and high power ground tends to contain a lot of noise, so the digital, high power, and analogue grounds were routed separately. Those grounds are connected to a single point on the board (star connected). This technique was applied to the power supply voltage as well, including 5 V and 12 V from the auxiliary power regulators. The sensitive traces were routed away from the power switching paths and digital traces, and a ground shield was added between if there was no way to place them a good distance apart.

4.3. 2-LAYER PCB

A design of 2-layer PCB for the converter was performed first, in which components are mounted on both sides. In order to reduce resistive power loses, 2 oz. copper thickness was used. See Appendix H. The design of 2-layer PCB for the detail of the designed PCB with the size of 21 cm x 17 cm.

This design was sent out for fabrication as the first version of the MISO converter intended to determine overall performance and identify any circuit design issues. Overall, the converter worked appropriately (full results analysis of the 4-layer prototype is provided in Chapter 5). Each input channel works at 360 kHz and self-adjusts power flow correctly. It can work with single or both inputs simultaneously. The constant voltage loop, constant current loop and MPPT interface circuit functioned appropriately. All the protective functions worked, including UVLO, OVP, cycle-by-cycle current limit, battery over discharge protection, and thermal shutdown. The power conversion efficiency was slightly lower than expected (around 85 %).

There were some minor errors that relate to this first PCB design. The footprint used for the gate driver ICs was incorrect, there was no power supply for the battery protection circuit when both inputs are unavailable (in the mode of discharging the battery), and it was not possible to program the microcontroller on board. However, given the overall good performance, a 4-layer PCB design was then carried out.

4.4. 4-LAYER PCB

Although the first version of the converter works properly, some issues that relate to this 2-layer PCB have been mentioned. It was required to improve the PCB for better performance of the converter. This could be accomplished by redesigning 2-layer PCB or move to a 4-layer PCB. During this step, the design of a 4-layer PCB has been done for comparison with the previously fabricated 2-layer PCB. To reduce the cost, instead of using both blind vias and through hole vias, the 4-layer PCB used through hole vias only. On this PCB, the board design was stacked by the characteristics of signals: POWER/POWER-GND/ANALOGUE-GND/SIGNAL in the order of Top layer/Middle layer 1/Middle layer 2/Bottom layer. Having a smaller size and greater copper thickness than the 2-layer PCB, this version was expected to gain some improvement of power conversion efficiency and have better heat dissipation. See Figure 4-2 to Figure 4-7 for the detail of 4-layer PCB design.

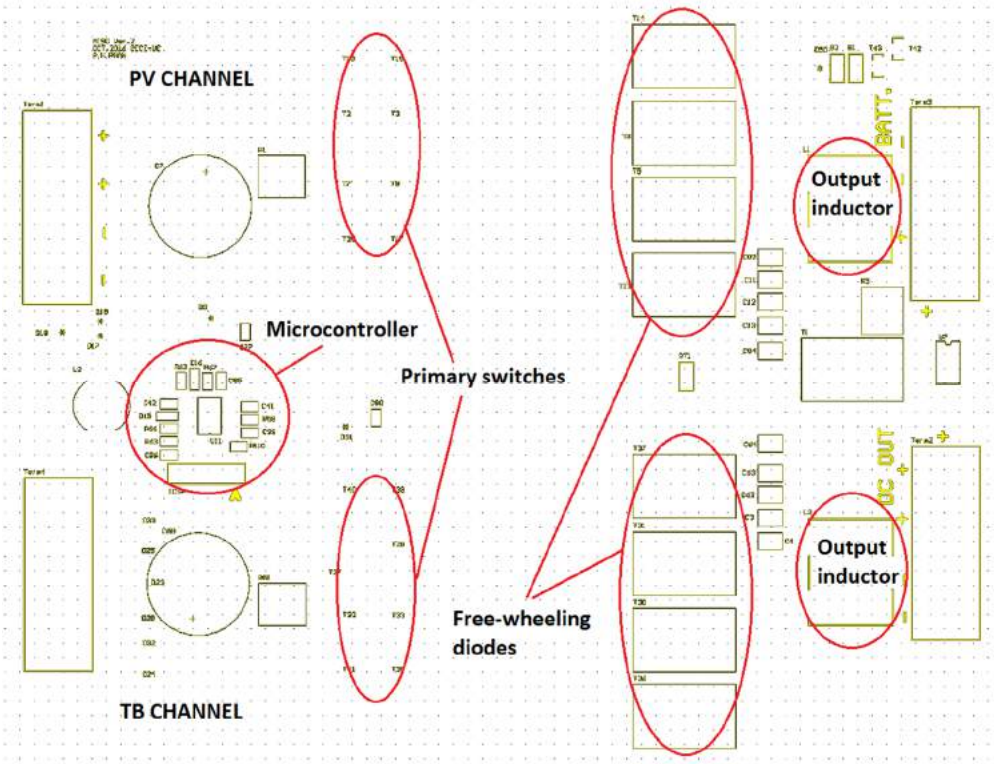

Figure 4-2. Components layout on the top side of the 4-layer PCB

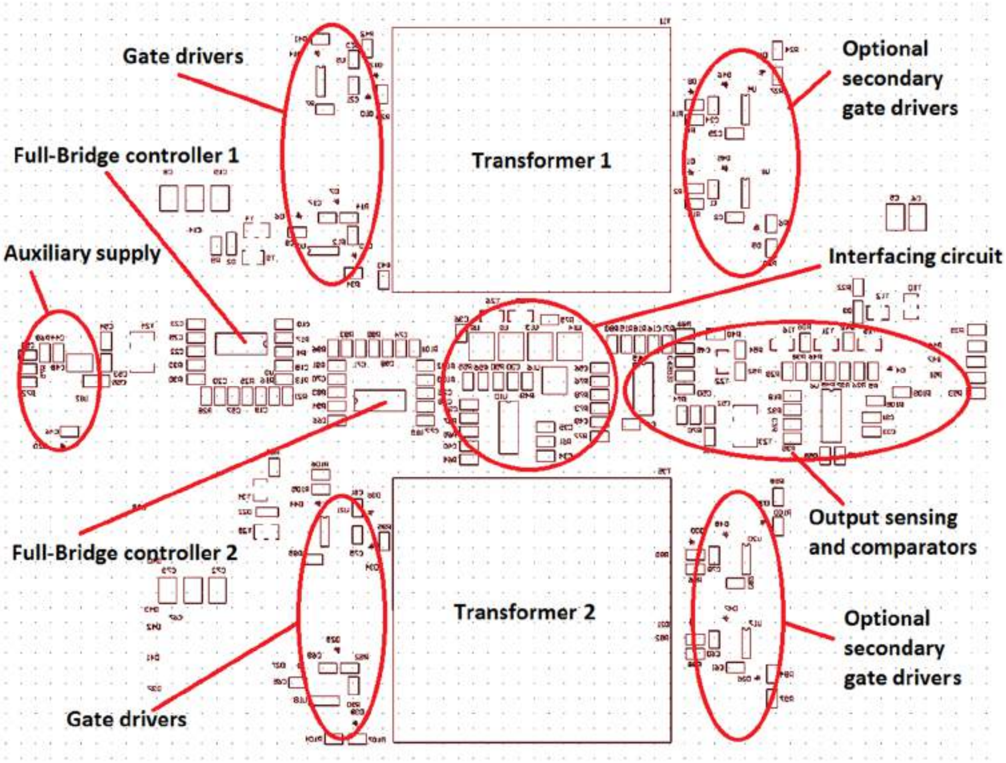

Figure 4-3. Components layout on the bottom side of the 4-layer PCB

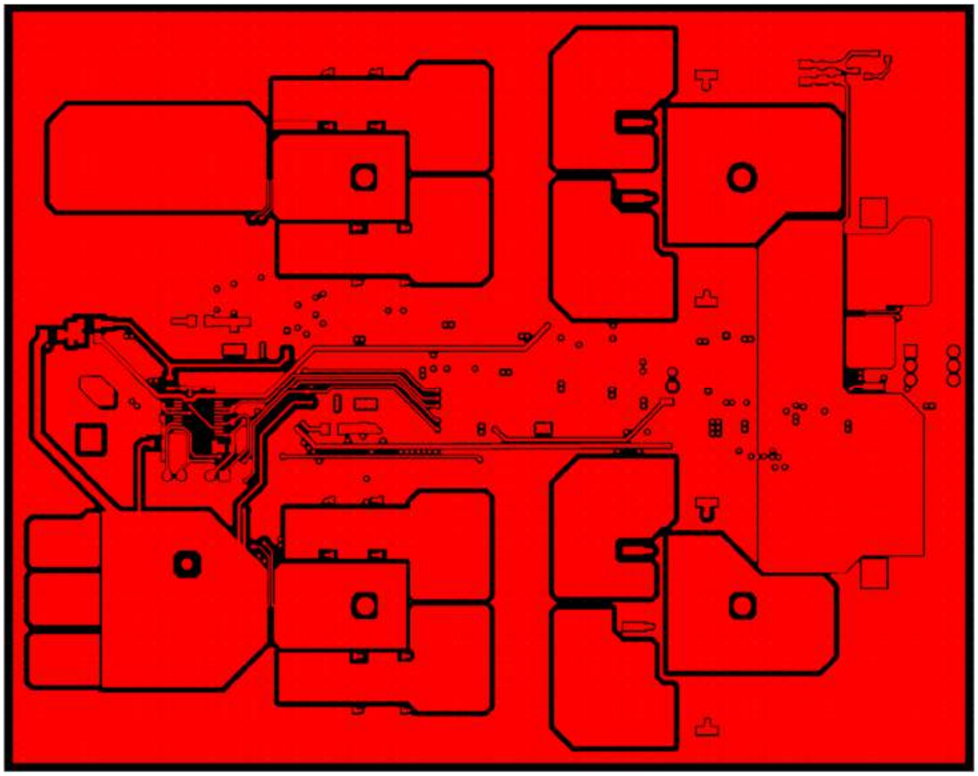

Figure 4-4. Top copper layer of the 4-layer PCB

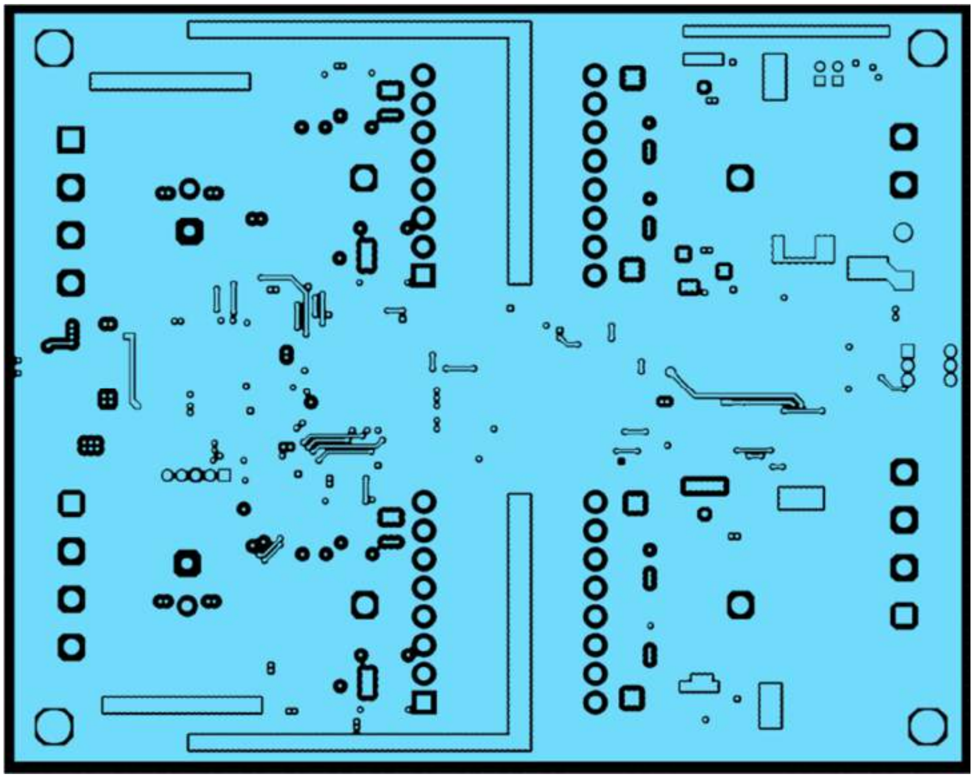

Figure 4-5. Middle-1 copper layer of the 4-layer PCB

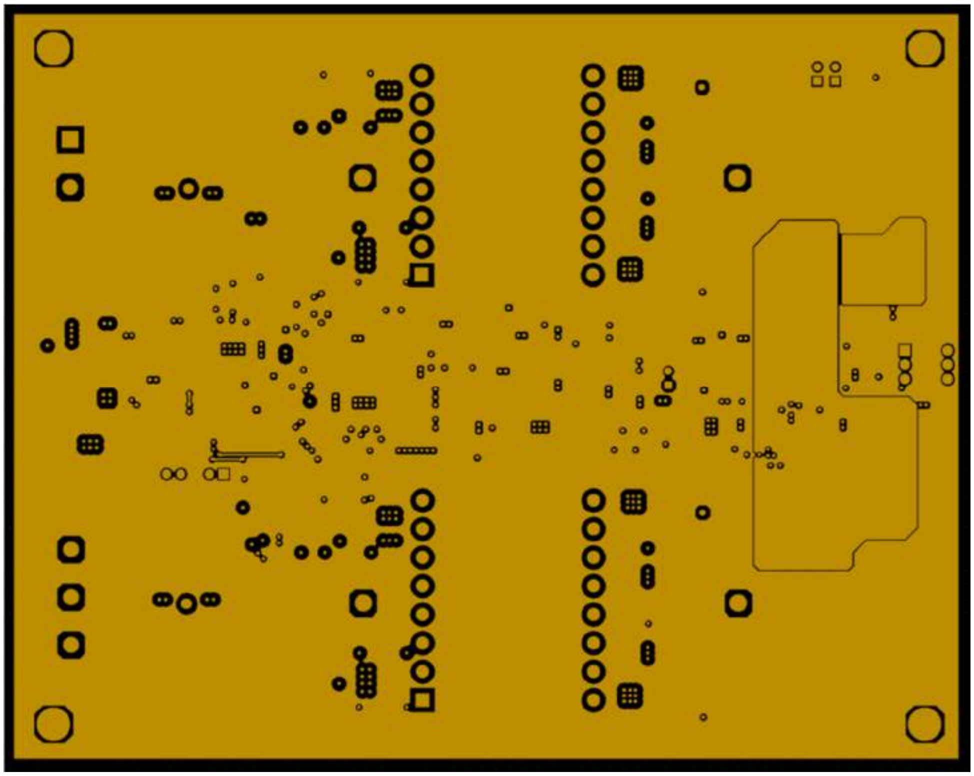

Figure 4-6. Middle-2 copper layer of the 4-layer PCB

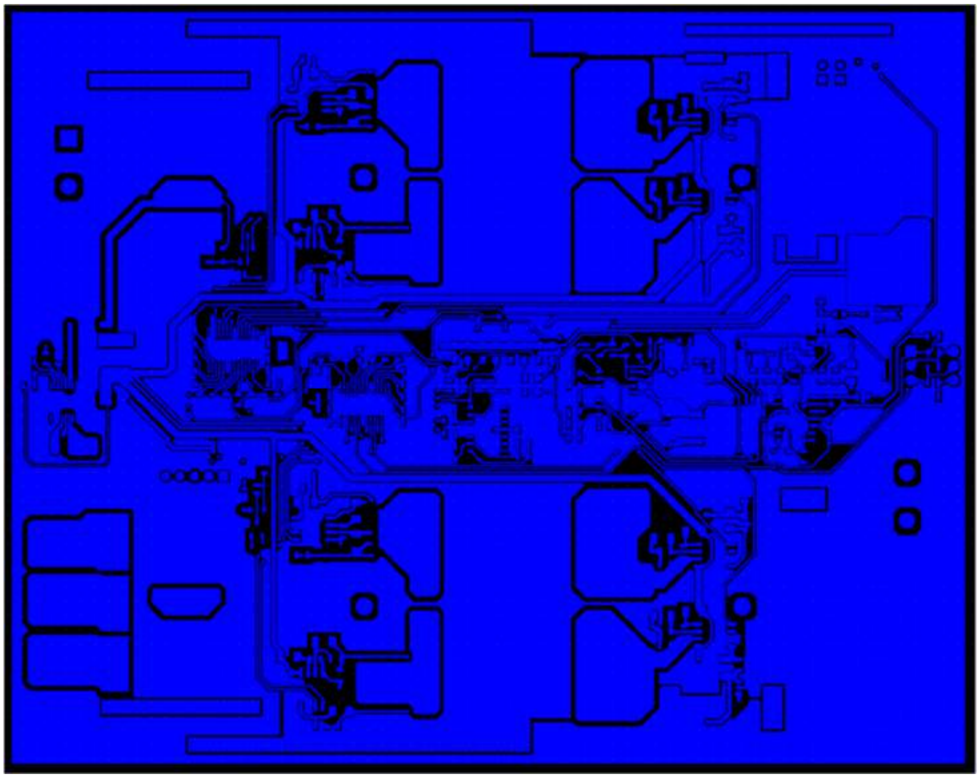

Figure 4-7. Bottom copper layer of the 4-layer PCB

4.5. SELECTED DESIGN

Table 4-1. 2-layer PCB versus 4-layer PCB

Category	**2-layer PCB**	**4-layer PCB**
Size	21cm x 17 cm	17cm x 13cm
Board assembling cost (devices attaching, soldering, and testing)	same	same
PCB cost (2 oz. copper thickness, exclude shipping cost)		
Seeed (200 pcs order)	9$/pcs	6.3$/pcs
PCBcart.com (5000 pcs order)	7.75$/pcs	6.43$/pcs
FirstPCB.com (5000 pcs order)	3$/pcs	2.67$/pcs
EMI & Noise decoupling		Better than 2-layer
Heat conduction		Better than 2-layer
Power conversion efficiency		Higher than 2-layer (shorter and thicker power traces. This means lower DC resistance and parasitic inductance on the power traces.

An assessment of 4-layer design was made and compared to the 2-layer PCB, which is shown in Table 4-1. As can be seen in the comparison table, the 4-layer PCB has more advantages and is a lower cost than the 2-layer PCB. Therefore, the 4-layer PCB was chosen for the revised version of the MISO converter.

CHAPTER 5 TEST RESULTS

5.1. SETTING UP

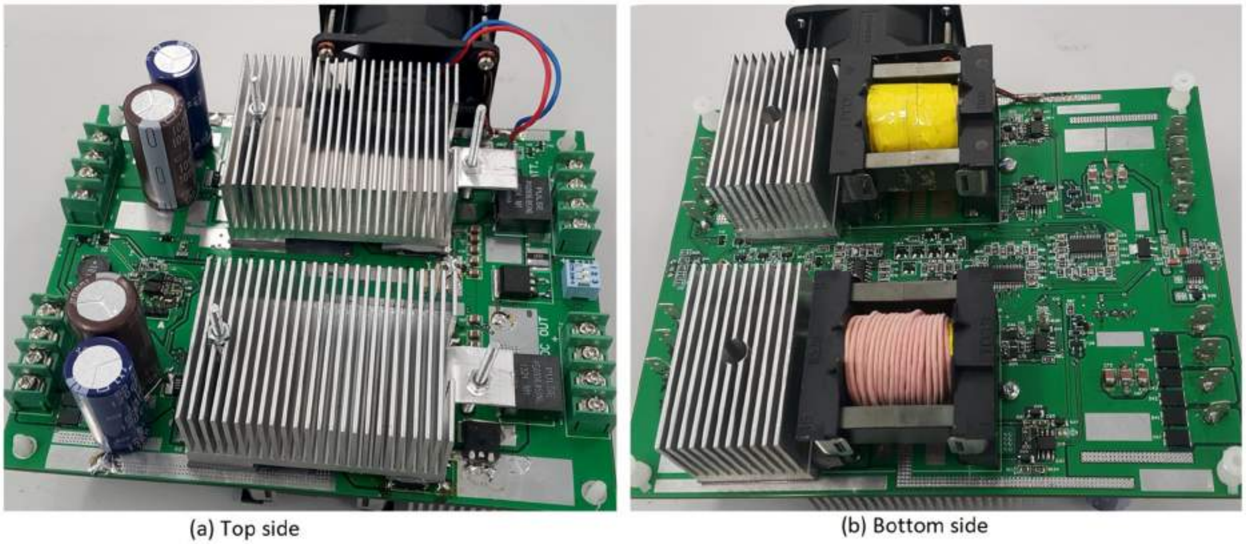

(a) Top side (b) Bottom side

Figure 5-1. The fully formed converter

Soldering and other component mounting have been done on the 4-layer PCB for physical experiments (See Figure 5-1). As the converter can perform many working functions, the characterization of the apparatus is divided into two main setups with different laboratory equipment. The first group of testing is conducted with ordinary power supplies, and the second group is carried out with emulated power sources for both PV solar pannels and wind/hydro turbines. For both groups of testing, the output can be connected to a source-free electronics load (that is, a resistive load), a lead-acid battery bank, or a combination of both.

5.1.1. Ordinary power supply based testing

The aim of this experimental setup was to test and characterise the converter for discrete functions, which vary from very basic to complicated functional operation. A low voltage, high current dc power supply (Model EA-PS 9080-510) was used for the PV input, while a three phase ac source was connected to the TB input (Chroma programmable AC source, Model 61704). With this combination, control loops and power conversion of each channel were checked. Along with these tests, the responses of the converter to all input conditions were also tested, such as start-up sequences, simultaneously running two inputs, and one input on/off or varying while another present. Additionally, protection functions were activated and tested. Lastly, testing the battery charging profile was carried out as part of this group.

5.1.2. Emulated renewable power source based testing

This group of testing was made to confirm the converter operation for real applications after all the functional blocks had been tested successfully. It is time-consuming and costly if these tests are conducted with real renewable energy sources such as solar panels and wind/hydro turbines. The best solution is to conduct these tests in a laboratory environment where there can be control of the various parameters. Therefore, emulated power sources for the two types of input power source of interest were established with laboratory equipment.

The PV input can be supplied by a Chroma programmable DC power supply (Model 62150H-600S) which is capable of emulating PV solar panel characteristics. The Chroma is very convenient for setting all the parameters of a particular PV solar panel, including V_{OC} – Open circuit voltage, I_{SC} – Short circuit current, V_{MP} – Voltage at the Maximum power point, and I_{MP} – Current at the Maximum power point. These parameters can be changed dynamically as the power supply is operating to emulate varying conditions, such as cloud covering, and sun motion.

On the other hand, creating an emulation of the Turbine channel input power source is quite complicated. A laboratory system for emulating turbines was built to test for the real application. The emulator was able to emulate turbine power curves without using a closed loop control system [77], and consists of a dc voltage source, a power resistor and a dc motor. Coupled with the dc motor shaft was a three-phase permanent magnet generator (sourced from an unknown model of wind turbine of approximately 300 W power) which was used as a power generator for the turbine input of the converter. The dc motor used has a power curve shape similar to a wind turbine power curve for a given wind speed. Wind speed variation can be emulated by variation of the dc motor's voltage source [77].

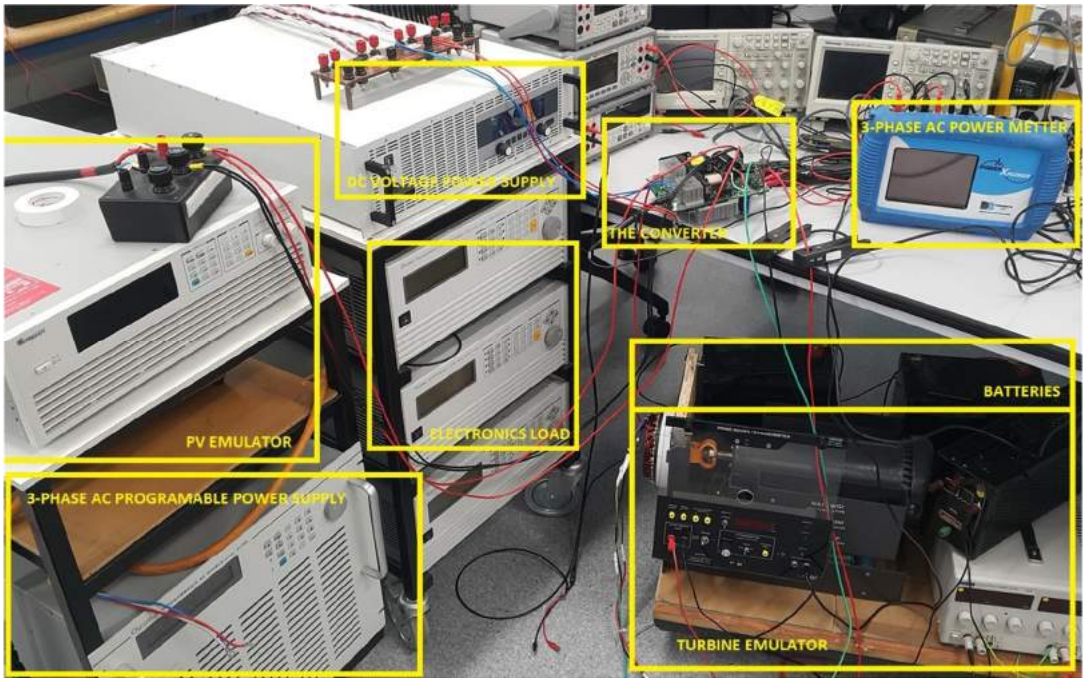

Figure 5-2. The arrangement of laboratory testing equipment for actual applications

Testing equipment for this emulation based testing group is shown in Figure 5-2. The ac generator's power curve characteristic needed to be characterized before running MPPT mode for the turbine input. At a specific value of dc voltage applied to the dc motor, the turbine emulator generates a specific power-speed curve. See Figure 5-3 for the relation between the turbine emulator's speed and its output power over different dc voltage values supplied to the dc motor. Based on this graph, a value of maximum power point for a specific applied dc voltage will be picked up by the MPPT mode. To emulate the variable wind/water flow condition, the dc input voltage supply to the turbine emulator is varied during the tests. Based on Figure 5-3 and the value of this input voltage, the MPP of the emulator is determined.

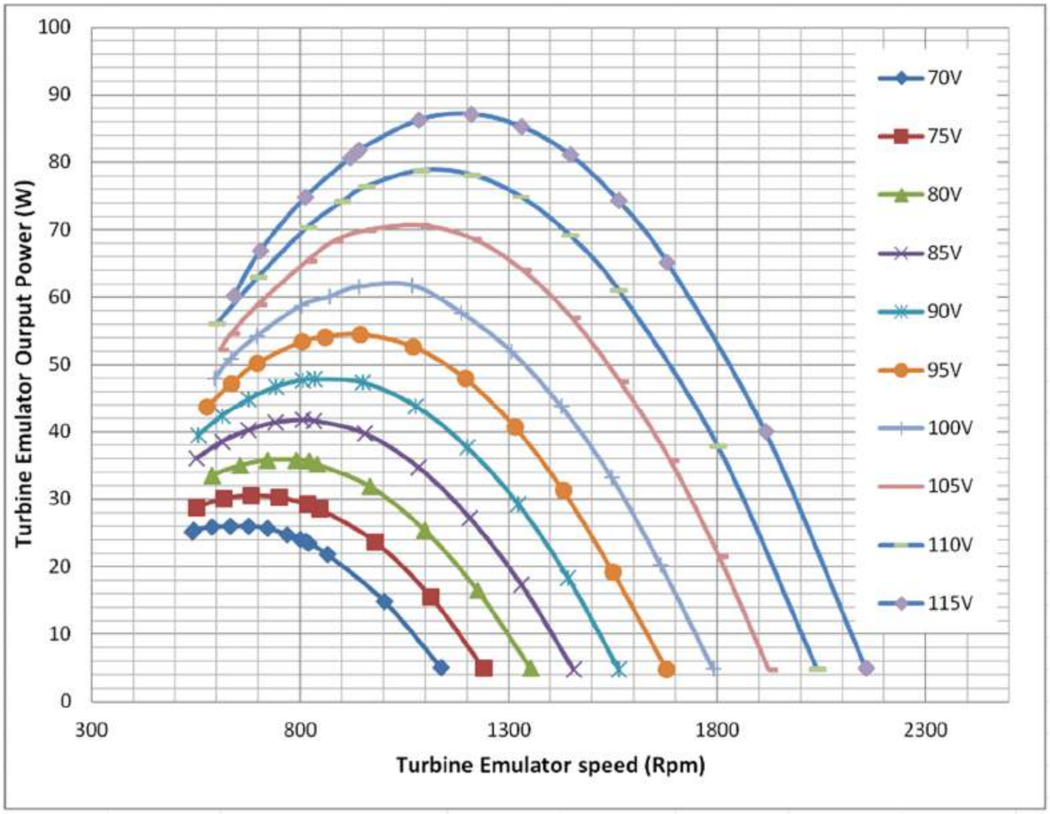

Figure 5-3. Power-speed characteristic curves for various input dc voltages to the turbine emulator

5.2. CONSTANT VOLTAGE OUTPUT MODE, NO BATTERY

This situation occurs when the battery bank is not connected to the output, and the resistive load is completely supplied by the available input power sources.

5.2.1. Start-up sequence

It is important to know how the converter reacts when it is first turned on. Figure 5-4 shows the output response when just the PV input is turned on suddenly with a source value of 25 V (no TB input), and no load at the output. Being filtered by the input capacitors, the input voltage (the Light Blue line, CH2) increases gradually from 0 V to 25 V in 2 ms. The channel turns on when the input voltage is about 16 V, and the output voltage (the Yellow line, CH1) is controlled by the soft-start function. There is some ringing of the converter output voltage around the set point before settling to the regulated value. The startup time for the output is about 2 ms.

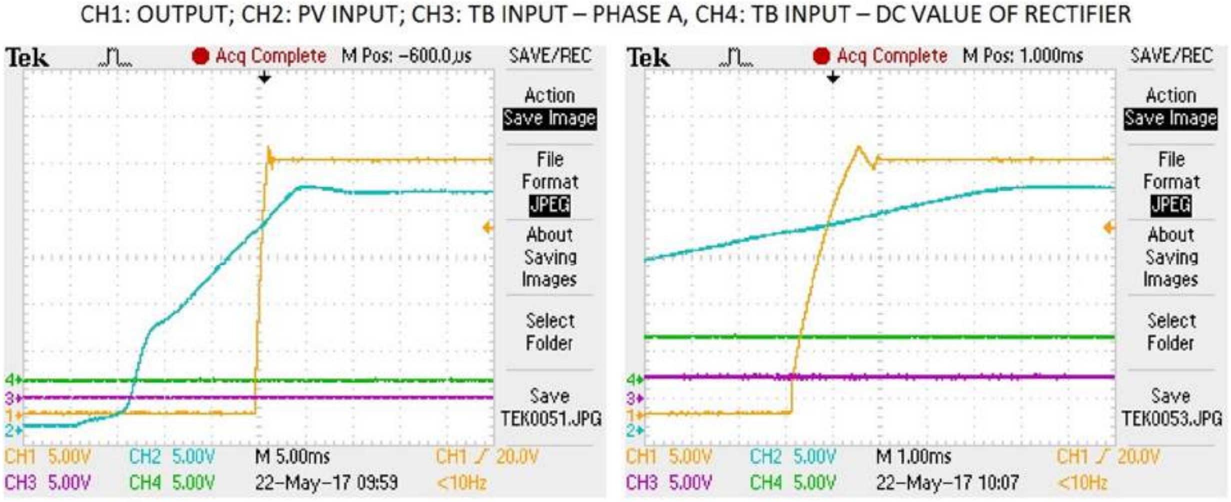
CH1: OUTPUT; CH2: PV INPUT; CH3: TB INPUT – PHASE A, CH4: TB INPUT – DC VALUE OF RECTIFIER

(a) On large scale capturing

(b) Zoom in

Figure 5-4. The start-up sequence of the converter when PV channel is supplied suddenly

The startup sequence test for TB channel was done by steps, incrementally increasing the input ac voltage. Because of the inrush current, all the output phases of the programmable ac source are shut down when the supply is suddenly connected to the TB channel. Thus the peak voltage ac input to the TB channel is increased suddenly from 10 V to 20 V to capture the dc-bus voltage startup while there is no load connected. The 3-phase ac input is rectified to a dc voltage by the three-phase bridge. As can be seen from Figure 5-5, when the dc voltage (the Green line, CH4) of the rectifier reaches an appropriate value, the channel turns on. Similar to the PV channel, the output voltage (the Yellow line, CH1) rings slightly before reaching its regulated voltage. The output start-up and settling time is also about 2 ms.

CH1: OUTPUT; CH2: PV INPUT; CH3: TB INPUT – PHASE A, CH4: TB INPUT – DC VALUE OF RECTIFIER

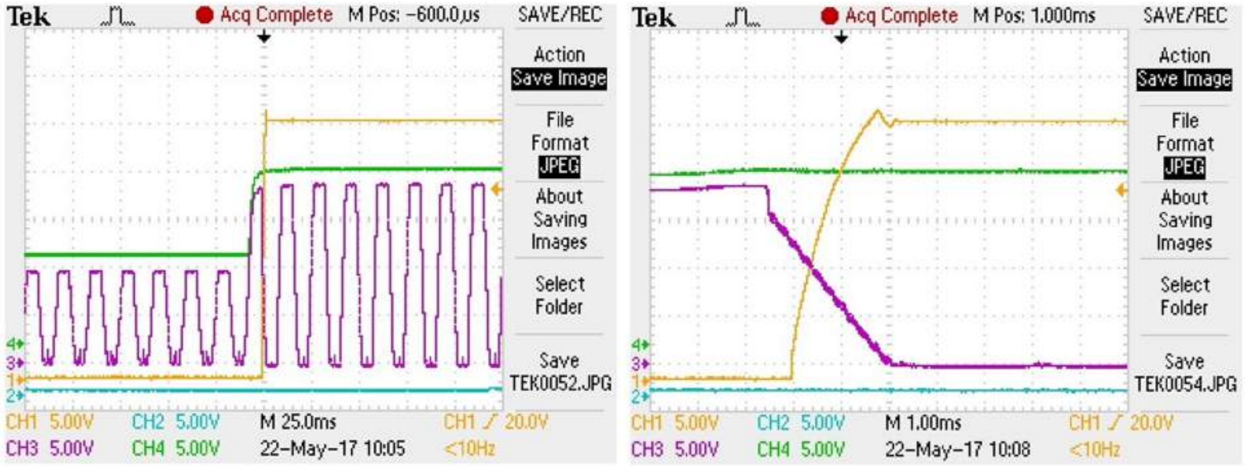

(a) On large scale capturing

(b) Zoom in

Figure 5-5. The start-up sequence of the converter when TB channel is supplied

The results of the start-up responses when supply power is suddenly applied to each input shows that the constant voltage loops work properly. The output voltage waveform shows the control loop is operating at appropriate values. The converter does not jump to any unexpected states. Regarding the spike on the output voltage waveform, this can be reduced and slowed down by adding more capacitance to the soft-start circuit. However, this is not an issue when connecting the output (dc-bus) to a battery.

The measured output voltage waveforms of the converter during start up sequences for both inputs were similar to the simulation results (see Figure 3-18). They have a similar starting time (took about 2 ms for the output voltage reaching its desired value), and the similar ringing times before settling. With this result, the relations between simulation models and practical design can be confirmed. Meaning the simulation models had supported the actual design of the converter.

5.2.2. Input fluctuation response

The TB channel is supplied by a three phase ac voltage source with amplitude of 23.8 V at 60 Hz which is the highest frequency value of the power supply (see Figure 5-6 – Green line, CH4). While a load (the Light Blue line, CH2) of 5 A is being drawn from the dc-bus while being sourced by the TB channel alone, the PV channel source (the Purple line, CH3) is suddenly turned on from 0 V to 40 V (see Figure 5-6 (a)). There is no change on the level of dc-bus voltage (the Yellow line, CH1) and there are no stability issues during or after the change of the input source. A slight increase in the peak voltage of the ac source is observed when its current drops. This voltage increase means the power to the dc-bus is now shared by the later activated channel. The output voltage (dc-bus) is also unchanged in the opposite situation, where the PV channel is turned off when both channels are on (see Figure 5-6 (b)). Note that the peak voltage of the ac generator drops as the load is now drawing power from this channel only.

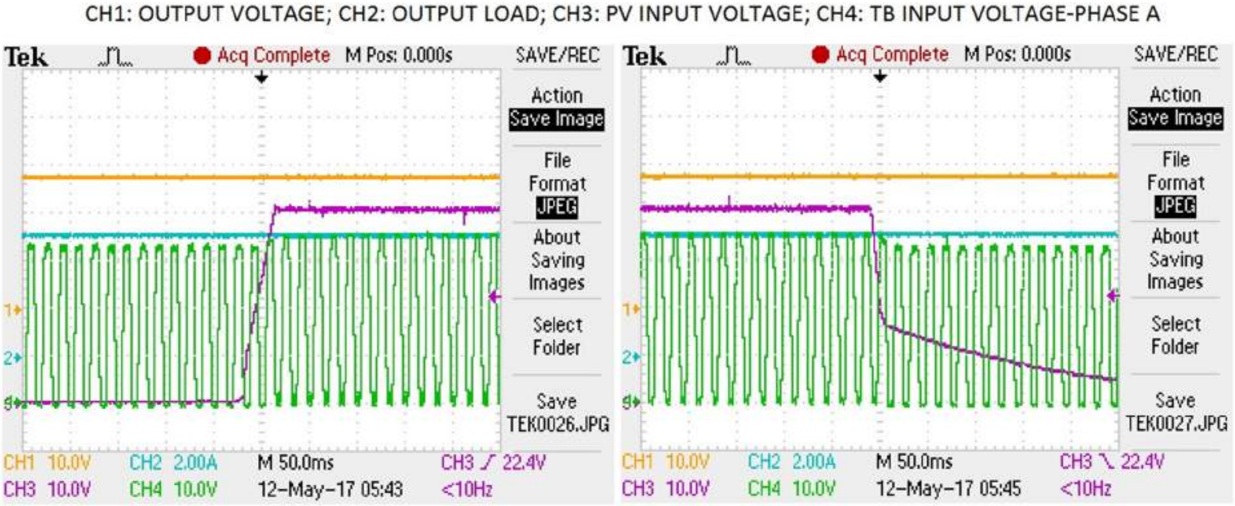

(a) PV channel turning on

(b) PV channel turning off

Figure 5-6. Converter response to step connection and disconnection of the PV source when being sourced by the TB channel only

Similar to the connection and disconnection of the PV channel, the connection and disconnection of the TB channel was also tested while the PV input voltage is sourcing power. The turbine generator is set to 60 Hz and the peak voltage is changed. For display purposes, the turbine voltage is measured and captured at the output of the three-phase rectifier (see Figure 5-7, Green line, CH4). As can be seen from Figure 5-7, there is no change in the converter output voltage or current and no stability problems when TB input voltage steps from 10 V to 20 V and vice versa.

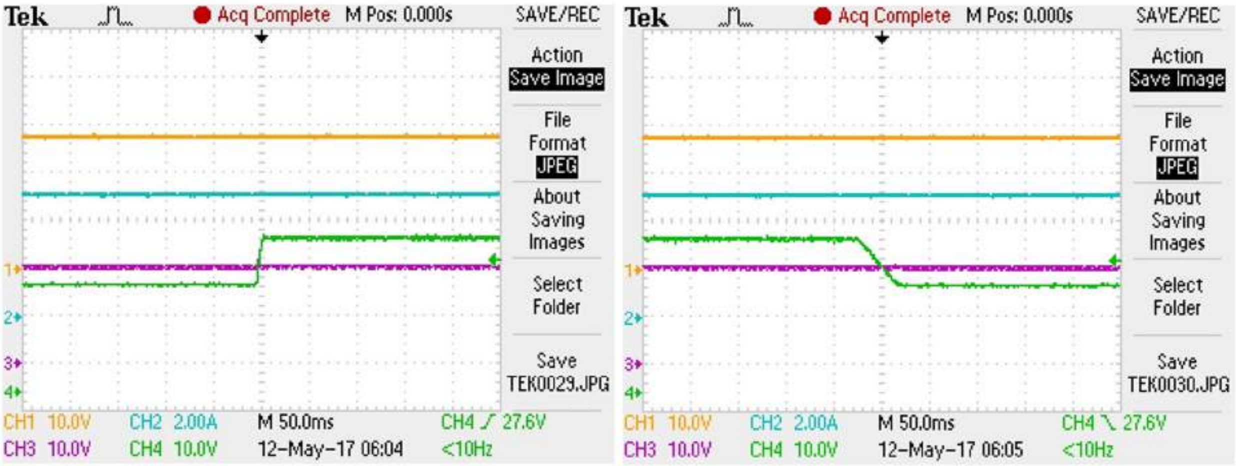
CH1: OUTPUT VOLTAGE; CH2: OUTPUT LOAD; CH3: PV INPUT VOLTAGE; CH4: TB INPUT VOLTAGE-PHASE A

(a) Increasing TB input voltage

(b) Decreasing TB input voltage

Figure 5-7. Converter responses over the fluctuations of TB input voltage

5.2.3. Load response

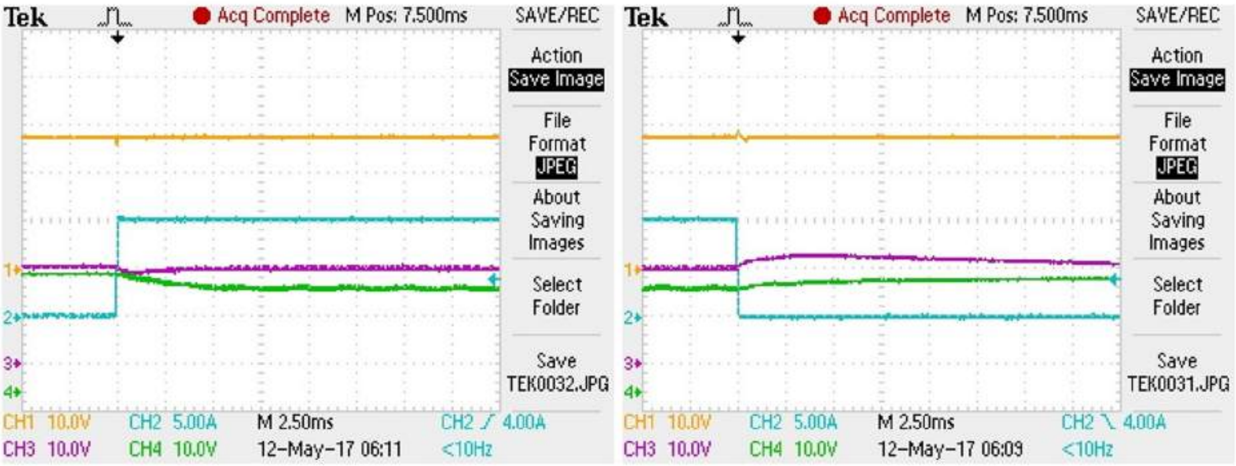
CH1: OUTPUT VOLTAGE; CH2: OUTPUT LOAD; CH3: PV VOLTAGE; CH4: TB VOLTAGE - DC VALUE

(a) Output load turning on

(b) Output load turning off

Figure 5-8. Output load response when input voltages are lower than the output voltage

The load response of the converter was tested at various conditions while both channels were present. As shown in Figure 5-8, the load current from the dc-bus (the Light Blue line, CH2) was changed rapidly from no load to 10 A and from 10 A back to 0 A. For display purposes, the input of the turbine channel was measured and captured at the output of the three-phase rectifier. In the first two cases (see Figure 5-8), the converter is working in the step up mode where both channel voltages are below the output voltage. There is a small amount of voltage ringing at the output (the Yellow line, CH1) at the moment of load change. The output voltage is maintained at the same level during the different load conditions. As the required current at the inputs changes according to the load, there are some variations in the input voltage level of the two sources (the Purple and Green line for PV and turbine voltage, respectively). Those input voltages rise at lighter load and reduce at heavier load.

In the step-down mode, where the voltage of both inputs are higher than output voltage (PV = 40 V and TB = 25 V, see Figure 5-9), there is no ringing on the output voltage when the load varies. The output voltage is very stably regulated at the desired value. In a similar manner to the step-up mode, the voltage of each source also varies according to the load conditions. However, there is a higher level of high frequency voltage ripple for the inputs at higher load conditions in comparison to the step-up mode (although still very low level).

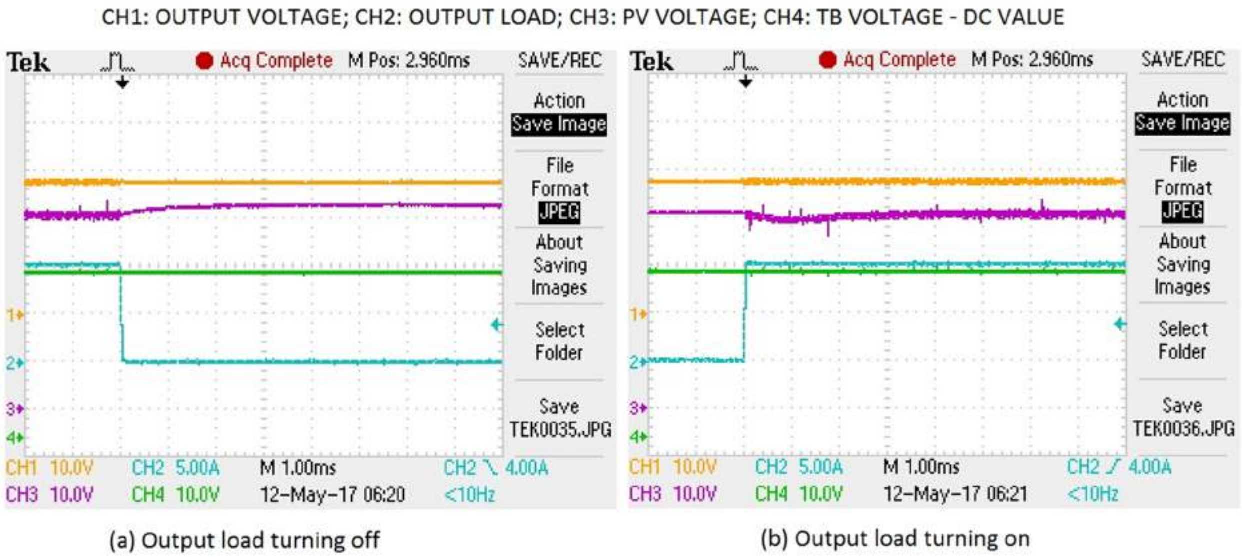

(a) Output load turning off

(b) Output load turning on

Figure 5-9. Output load response when inputs voltages are higher than the output voltage

5.2.4. Power conversion efficiency

The power conversion efficiency testing for the converter was conducted in constant output voltage mode with standard power supplies. Due to the power capability limitation of the turbine emulator that can only achieve up to 90 W of output power (see Figure 5-3), it was unable to cover the whole range of input power in MPPT mode for the turbine input channel. As a result, using emulators to measure the power conversion efficiency in MPPT mode while both inputs are sourcing was unfeasible. The tests were also conducted with just the resistive load on the output.

As a wide range of input voltage is allowed for both sources, which includes step-up and step-down mode for each channel, the power conversion efficiency tests were divided into four groups. They are for both channels in step-up mode, both channels in step-down mode, step-up

PV and step-down TB, and step-down PV and step-up TB. Input power measurements were taken from the programmable power supplies. Unfortunately, the output current of the three-phase power supply is limited to 16 A. This power supply also shuts down automatically when a surge current occurs. The dc power supply is also limited to 25 A. Therefore, these conversion efficiency tests are limited to a lower range of input power.

During the power conversion efficiency testing, the distribution of input power from each input source is also displayed. As described, the control method for regulating output voltage and current is using the current mirror structure for keeping both channels at the same value of output PWM signals. This leads to the shared power between the two sources being highly dependent on their voltage levels (the dc voltage of the three-phase rectifier output on the turbine channel and the dc voltage of PV source output).

Firstly, the converter operation is set for both channels in step-up mode. The dc voltage value of the TB input is around 24 V, while the PV voltage is about 20 V. For the whole range of load, the dc-bus voltage is always regulated at 26.7 V. As shown in Figure 5-10, 300 W is the maximum total input power that can be tested in this condition due to the limitation of the power supplies. The conversion efficiency increases gradually until reaching its peak at slightly above 93 % at 150 W input power. The efficiency slowly reduces to 91 % when the converter takes more power from this peak point. The distribution of input power from each channel is also displayed in this graph. There is no power from the TB input when the total input power is lower than 30 W; however, the converter increasingly takes power from this channel when it needs more power. The share of the TB channel input power keeps increasing and eventually becomes the larger part of the power range when the total input power is higher than 80 W. For the PV channel, the input power increases consistently to follow the load demand.

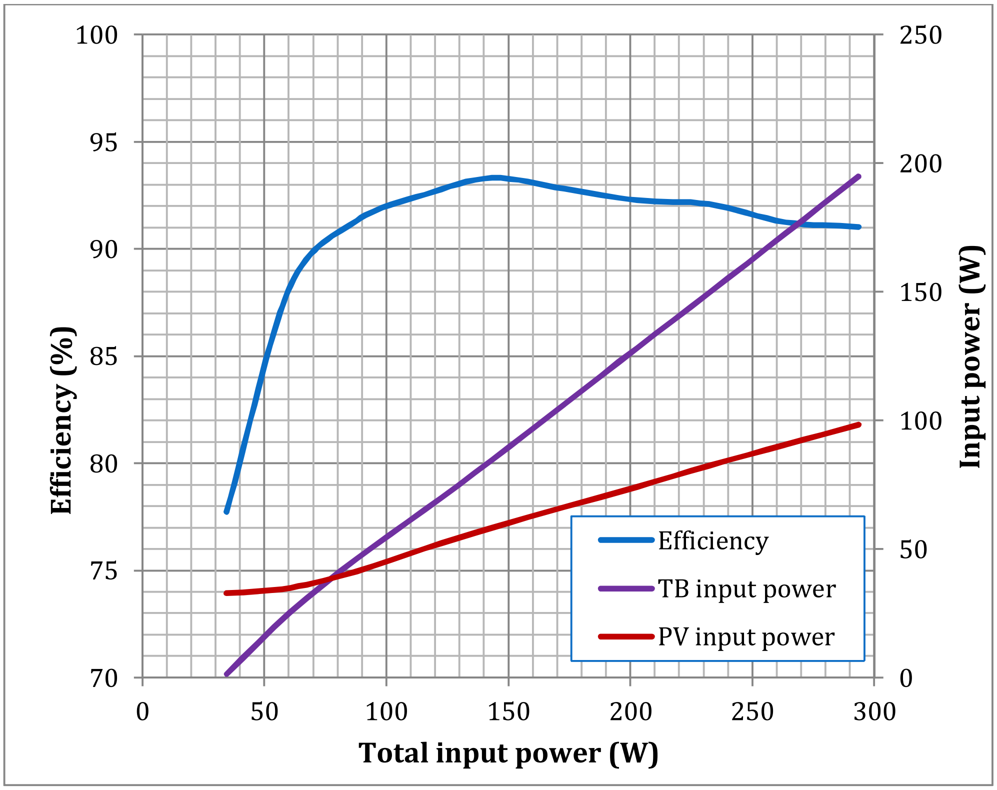

Figure 5-10. Both channels in step-up mode

The results of power conversion efficiency and power distribution between channels are shown in Figure 5-11, where both input source voltages are set to be higher than the output voltage. In this case, the TB channel voltage is around 36.8 V and the PV channel voltage is about 40 V. At the range of total input power below 350 W, the efficiency increases gradually for the first 150 W from around 72 % to 81 % and then only adds 3 % more in the next 150 W. There is no power from the TB source that is used by the converter until the demand power is higher than 350 W. From 350 W of total input power, the converter starts to draw power from both channels. However, the amount of power from the PV source is about 5 times the power from the TB source. The efficiency keeps increasing to 86 % at around 600 W and seems to flatten out from this point. As the ac power supply reached its current limit, the test stopped when the total input power reached 800 W.

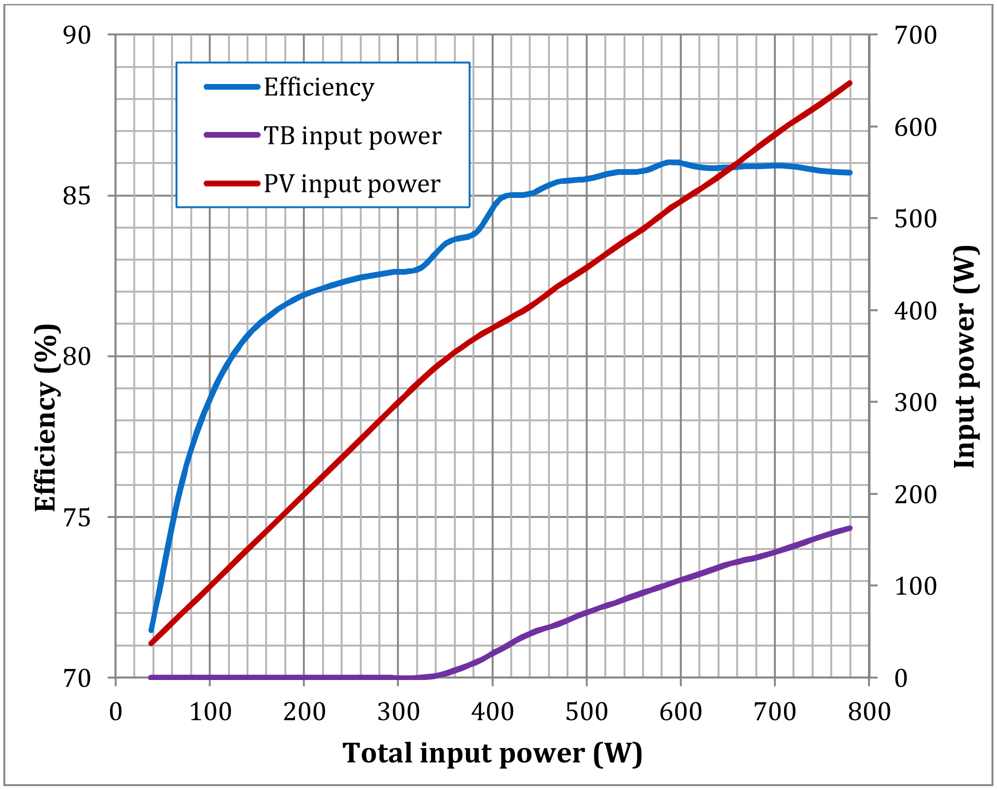

Figure 5-11. Both channels step-down mode

When the PV channel is in step-up mode and TB channel is in step-down mode, the conversion efficiency appears to be the highest range. A peak of 95.3 % was recorded at 400 W over the tested range of input power to about 600 W. The input voltages are set at about 54 V and 24 V for the TB and PV input, respectively. As can be seen from Figure 5-12, at the peak efficiency point, the amount of power being drawn from each channel is equal. The power flow from the PV input is higher than that of the TB input when the total input power is lower than 350 W. There is no power from the TB source until the converter needs more power than 150 W. Above 150 W, the power from the TB input increases rapidly and becomes the dominant power source when the total power is higher than the power at the peak efficiency point. These tests were stopped at just under 600 W of total input power, where the power from the TB and PV source is about 330 W and 230 W respectively.

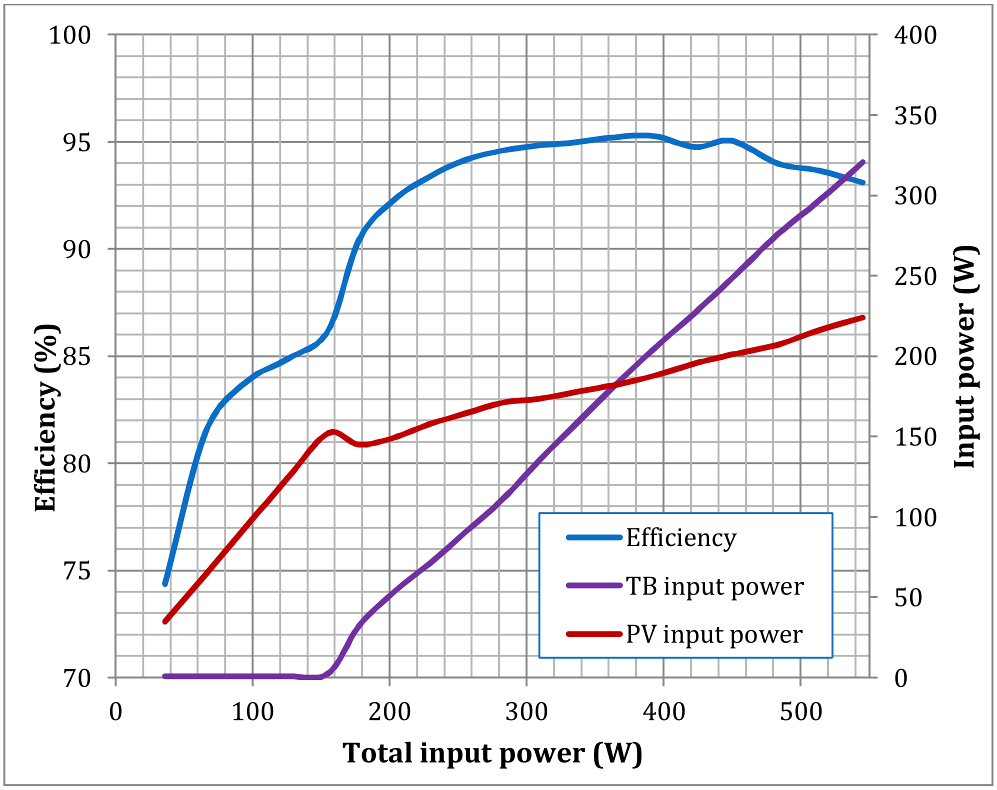

Figure 5-12. PV channel in step-up, and TB channel in step-down mode

In the last efficiency tests, the input voltages were set for TB in step-up mode and PV in step-down mode (25.5 V and 40 V, respectively). The output voltage is still regulated at 26.7 V (as this is the default output voltage of dc-bus and also the float charge voltage of the battery if it was connected). As shown in Figure 5-13, the converter takes power from both inputs over the whole range of tested power from 0 W to 700 W. However, the amount of energy from the PV source is about 3 times higher than that from the TB input. Regarding power conversion efficiency, there is an increase from around 70 % to slightly above 86 % in the first 300 W. From this peak of efficiency, there is a gradual reduction to 85 % at the maximum tested input power.

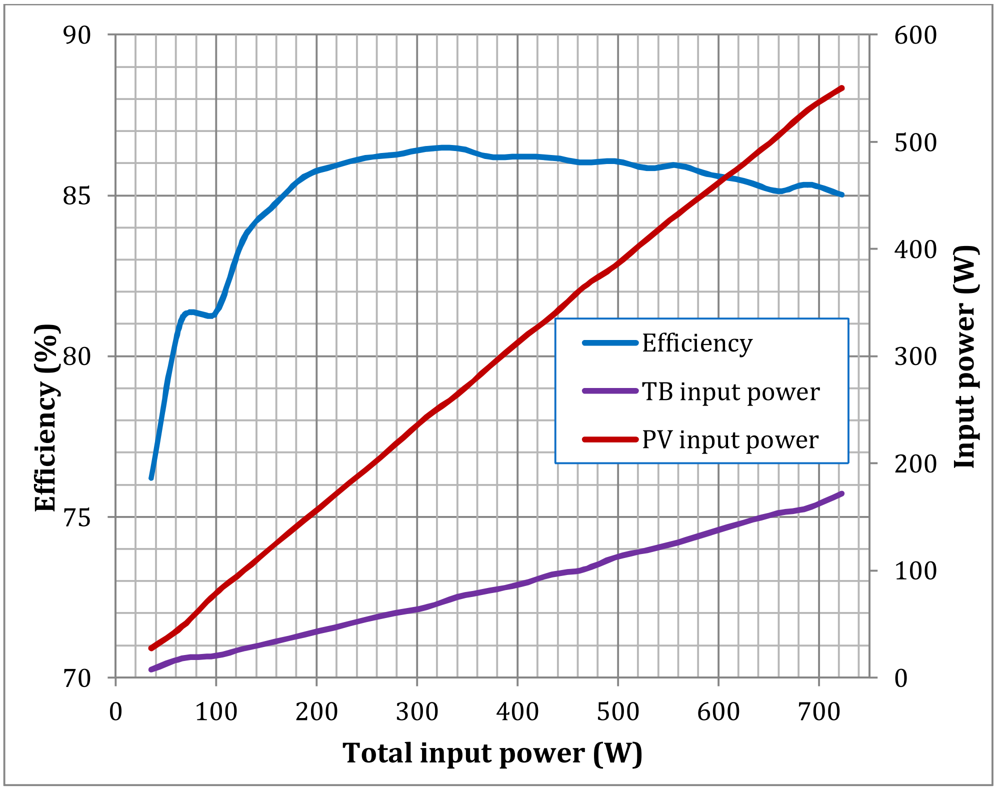

Figure 5-13. PV channel in step-down, and TB channel in step-up mode

5.3. CONSTANT OUTPUT VOLTAGE AND CURRENT MODE, WITH A BATTERY AND A RESISTIVE LOAD AT THE OUTPUT

5.3.1. Battery size selection

Table 5-1. Allocation of the switch states for charging reference voltage

K3	K2	K1	Charging reference voltage (V)
ON	ON	ON	0.5154
ON	ON	OFF	0.9335
ON	OFF	ON	1.2825
ON	OFF	OFF	1.5737
OFF	ON	ON	2.0083
OFF	ON	OFF	2.1192
OFF	OFF	ON	2.3682
OFF	OFF	OFF	2.5168

Battery charging current is measured by sensing the voltage drop over the series current-sense resistor and then amplifying this to a compatible value for the constant current loop control. Based on the charging reference voltage and the output voltage of the amplifier, the loop adjusts the duty cycle of PWM signals in both channels to regulate the battery charging current.

In order to set the appropriate level of battery charging current for the battery size, the selection switches are used for setting the charging reference voltage (see Table 5-1). The current sensing voltage was also measured for different charging currents (Figure 5-14). By matching the current sensing voltage and the charging reference voltage, the value of charged current is determined. Therefore, the recommended switch configuration for a battery's capacity is shown in Table 5-2.

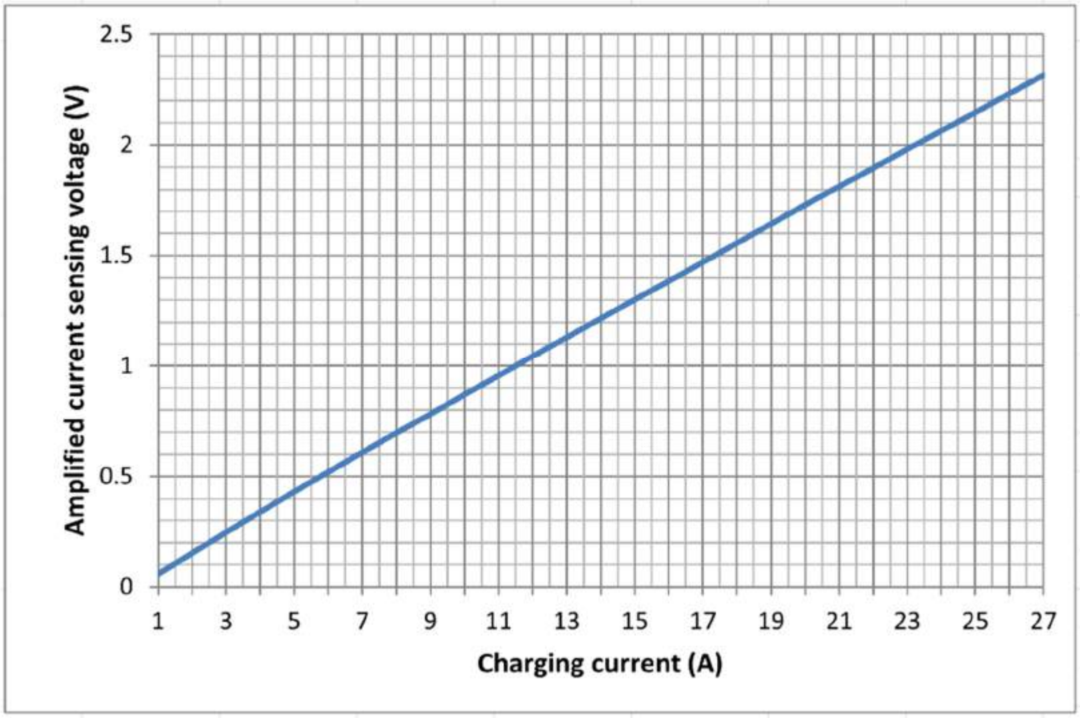

Figure 5-14. Measured current sensing voltage over charging current

Table 5-2. Recommended switch configuration for given battery capacity

K3	K2	K1	Charging current (A)	Battery capacity (Ah)
ON	ON	ON	6.8	75
ON	ON	OFF	10.5	120
ON	OFF	ON	15	160
ON	OFF	OFF	18	200
OFF	ON	ON	23	240
OFF	ON	OFF	25	260
OFF	OFF	ON	27	300
OFF	OFF	OFF	30	320

All the tests with a battery connected to the dc-bus in this section are made with a lead-acid 24V 75AH battery owing to availability. The constant current charging level was set at 6.8A (K1 ON, K2 ON and K3 ON).

5.3.2. Response to step changes in input voltage

In normal application operation, it is expected that a 24 V battery bank will be connected to the output dc-bus. As such, start up when a battery is connected was tested. Initially the input voltage is turned on at the PV channel, from 0 to 25 V. As can be seen in Figure 5-15 (a), no current is initially taken from the dc-bus, the charging current increases from 0 A to the set charging current of 6.8 A in roughly 7 ms after the converter turns on. A small current spike appears during this period as the CC mode takes control. While the load is drawing current from the battery via the dc-bus (no input power from the PV channel or TB channel), the start-up sequences of the converter are shown in Figure 5-15 (b). In about 12 ms, the current to battery changes rapidly from -5 A (negative, as supplying current to the load) to 6.8 A. That means that the output load current is replaced quickly from the battery source to the power from the input channel via the converter in the first 5ms of this period. When the input power is still available after supplying all of the load power requirements, the converter starts increasing charging current to the battery. There is no disruption of the current to the load. In both start-up sequences, the dc-bus voltage slightly increases when the input power source is applied to the converter.

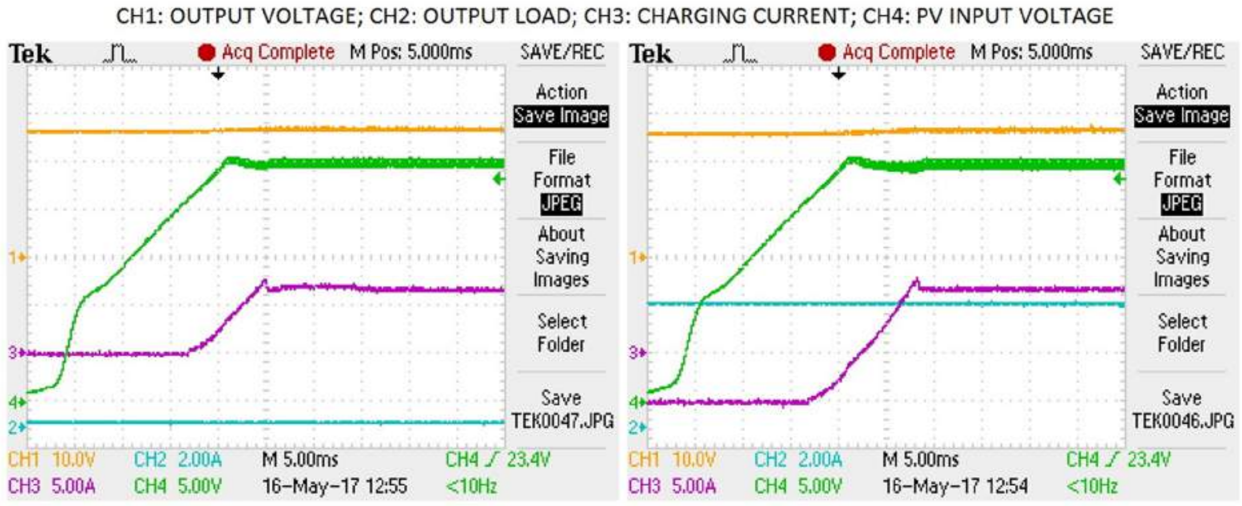
CH1: OUTPUT VOLTAGE; CH2: OUTPUT LOAD; CH3: CHARGING CURRENT; CH4: PV INPUT VOLTAGE

(a) No load at DC-Bus

(b) Load = 5A at DC-Bus

Figure 5-15. Start-up sequences when turning on PV source while a battery is connected to the output, with (a) no load at the dc-bus and (b) load of 5A at the dc-bus

Further tests were made for observing the effect of fluctuation of the input voltage while charging the battery. A load was also connected to the dc-bus at the same time. In both conditions of suddenly changing input voltage from 25 V to 20 V and vice versa, the output load is maintained at the same value while there is a minor change of the battery charging current (see Figure 5-16). Higher voltage ripples at the dc-bus and input sources appear when the input voltage is higher. There is no change in dc-bus voltage value and there are no stability issues after the step changes.

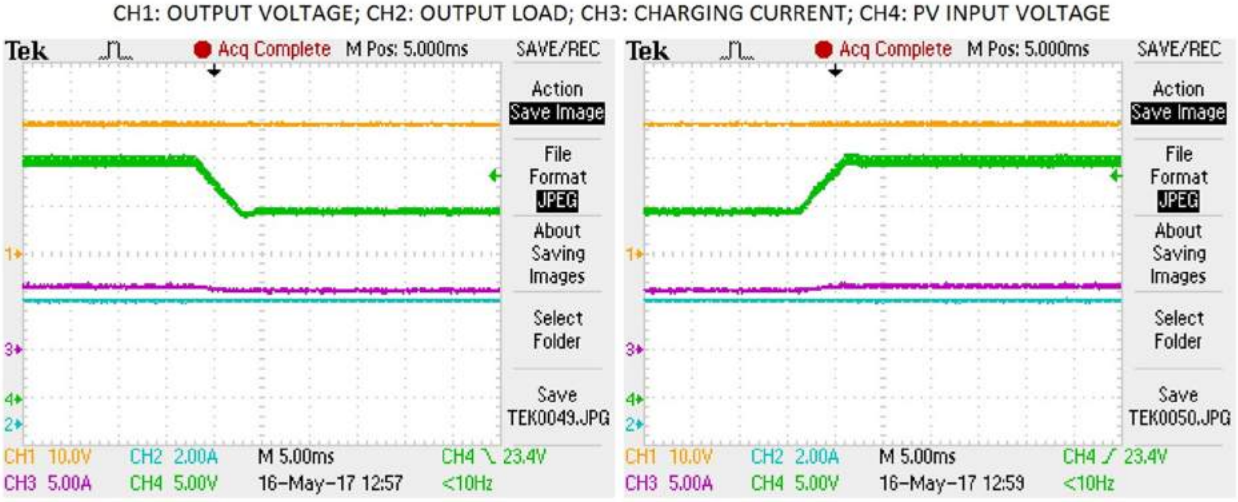

(a) PV voltage changes from 25V to 20V

(b) PV voltage changes from 20V to 25V

Figure 5-16. PV input voltage fluctuations including (a) changes from 25 V to 20 V ad (b) changes from 20 V to 25 V while charging the battery and supplying output load

Similar tests with the input step changes on TB channel were also made to see how the converter interacts with the battery. As there was the same configuration on both input channels, there was no difference between them regarding the results. The converter adapts quickly to the changes of TB input voltage, and the output load switches smoothly between the battery and power from TB input.

5.3.3. Output load response

The converter is designed to have the capability of providing power to dc-bus/load and charging a battery at the same time. Therefore, the effect of fluctuations of output load while charging the battery has also been tested. As shown in Figure 5-17, while the battery is being charged at the constant current stage of 6.8 A, the load on the dc-bus is changed suddenly from 0 A to 5 A and then from 5 A to 0 A. After the changes, the charging current and the output voltage is maintained and is stable at the designed value. The response time is less than 200 µs according to the output conditions. As the power demand of the input changes, there are small variations of the input voltage, where it jumps to a slightly higher level under lighter load conditions and vice versa.

CH1: OUTPUT VOLTAGE; CH2: OUTPUT LOAD; CH3: CHARGING CURRENT; CH4: PV INPUT VOLTAGE

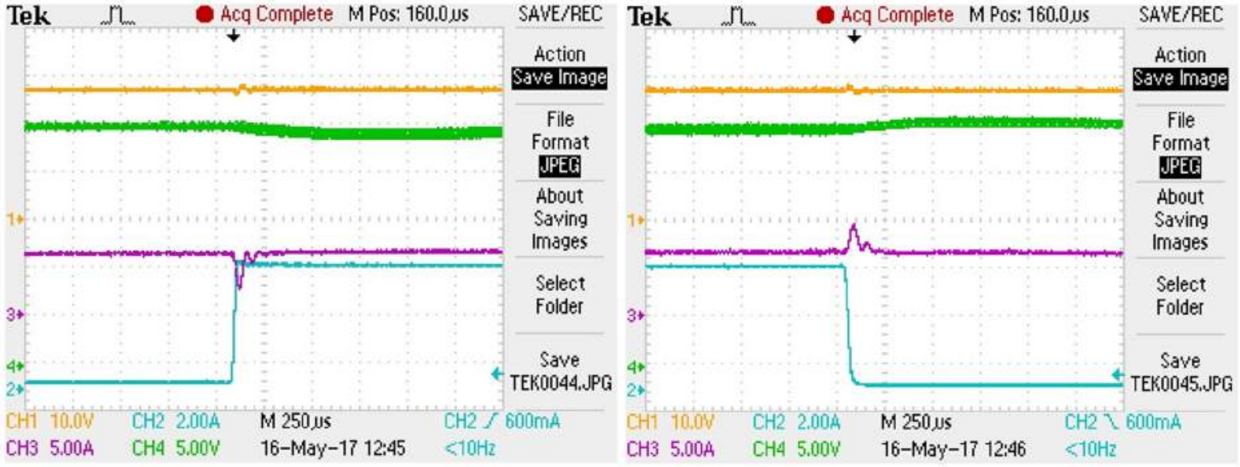

(a) Increasing output load

(a) Decreasing output load

Figure 5-17. Converter responses to the load with (a) step increase from 0 A to 5 A and (b) step decrease from 5 A to 0 A while it's charging the battery

5.3.4. Battery charging profile

Charging measurements were made for the 24 V, 75 AH battery. The constant current charging level was set at 6.8 A. The voltage level will be set at 28.33 V for the constant voltage charge stage, and 26.70 V for float charge. As can be seen from the Figure 5-18, the battery is charged via three stages. Starting with the constant current charging stage at the maximum value of 6.8 A, the battery voltage increases gradually from 23.5 V to 28.3 V in about 5 hours. When the battery voltage reaches 28.3 V, the constant voltage mode (bulk charge) is activated. During this stage, the battery voltage is regulated at 28.3 V and the charging current reduces from 6.8 A to 1 A in the next four hours. The converter changes to float charge mode (regulating the battery voltage at 26.73 V) when charging current drops to below 1 A. In this case, it takes about 12 hours in total to charge the battery fully from its lowest level.

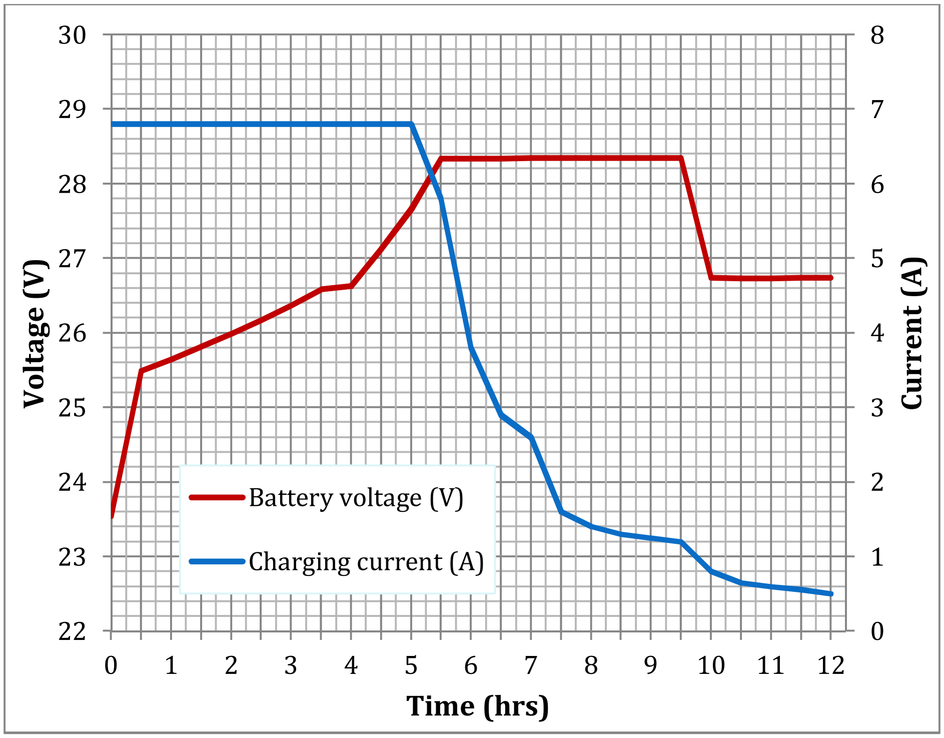

Figure 5-18. Battery charging profile

The converter is shown to perform a charging profile through the 3 specified stages. There were no issues with the battery charging control. Based on the value of battery voltage and the charging current, the charging circuit automatically selects the appropriate charging stage.

5.4. MPPT MODE

The MPPT mode is activated by comparing the required output power of the converter to the input power sources. When the total load from the output of the converter (output load plus battery charging) is higher than the source can supply, the CV loop or CC loop tries to extract as much current as possible from the input sources while maintaining a constant output load current. Based on the amount of dc-bus voltage drop, the MPPT mode is turned on automatically. The response time for reaching the maximum power point varies depending on various parameter conditions. Simplicity and robustness are the main advantages of the P&O algorithm, however, the operating voltage naturally oscillates about the MPP and some of the available power is lost.

Due to the power limitation of TB emulator, all the tests in MPPT mode that related to TB input channel were conducted in a low power range (under 90W of input power). However, the aim of these tests is to confirm the MPPT algorithm of the converter is functioning correctly.

5.4.1. PV input MPPT

Figure 5-19 shows the oscillation of input current and voltage around the maximum input power point created by the MPPT algorithm. In this case, the PV input source is an emulated solar panel (V_{OC}=40 V, I_{SC}=15 A, V_{MP}=24.17 A, I_{MP}=10.38 A). This emulation was realized with the Chroma programmable DC power supply. The yellow line (CH1) is the output load from dc-bus, and the green line (CH4) is charging current for the battery. The oscilloscope channels (CH2: PV input voltage, CH3: PV input current) were set to ac mode so that the fluctuations around the maximum power point were observed. While the output load and battery charging current are maintained at 5 A and 3 A, the input voltage and current are perturbed around a fixed level. The period of each level lasts about 60 ms after a step change. This is quite fast relative to the change of input parameters in the real applications, such as PV panels that become partly covered by cloud or wind turbines experiencing variation the wind speed. This MPPT can be adjusted to a slower response in the firmware; however, keeping this fast response could save some lost power.

Figure 5-19. MPPT mode is operating around the maximum power point for PV input

Figure 5-20 shows input and output states of the converter when the PV channel was at its maximum designed input power. The MPP of the solar input source was set at 1 kW (V_{MP} = 45.75 V and I_{MP} = 22.7 V). The results shows the input voltage (the Light Green trace) was maintained at around 47 V and the input current (the Purple trace) was about 22 A. With this result, it is confirmed that the PV channel is able to track the MPP and convert power at its maximum power rating.

Figure 5-20. MPPT mode of PV channel at the 1 kW MPP

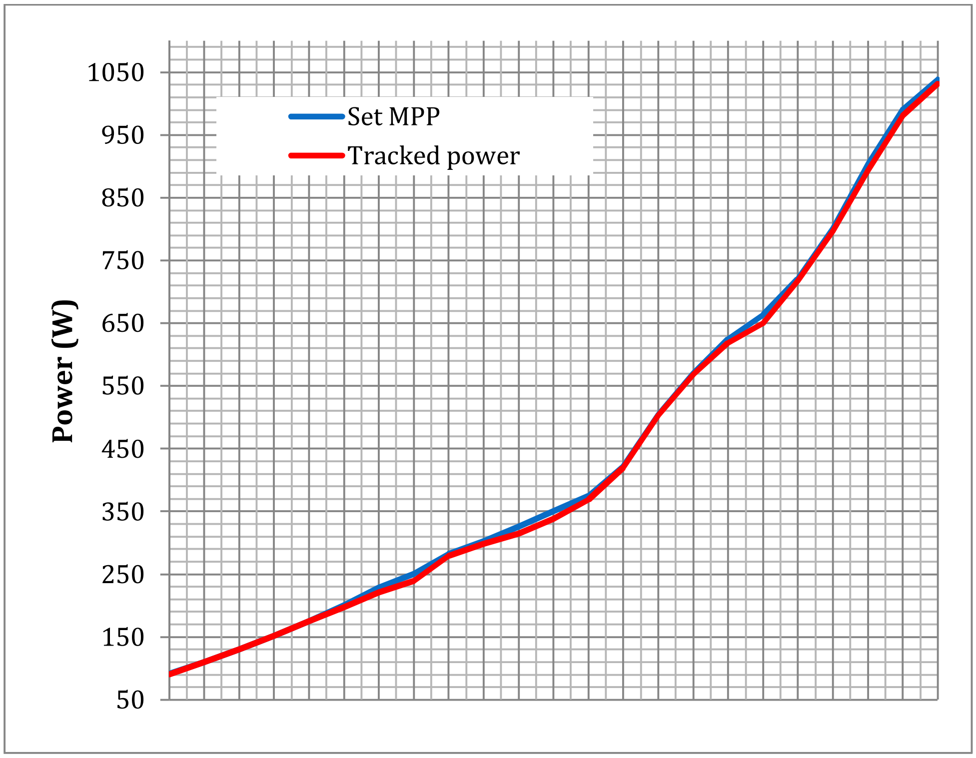

Figure 5-21. Tracked power vs. Set maximum power point of the PV input source

The converter’s response to the changing of maximum power point of the PV source is shown in Figure 5-21 over its possible power range. These MPPs are set by the programmable power supply which emulates a solar panels output. As can be seen from the graph, the tracked power (the Red line) is very close to set MPP value (the Blue line). The biggest difference between the set MPP and tracked power is about 4% (tracked 240 W over 250 W of MPP).

Figure 5-22 shows the results of step changes in the MPP of the PV input. The yellow line (CH1) is the measured load current from the dc-bus, and the green line (CH4) is the battery charging current. For the PV input, CH2 and CH3 are the PV voltage and current, respectively. In the first case (Figure 5-22 (a)), the MPP is reduced from 206 W (V_{MP} = 25.8 V, I_{MP} = 8 A) to 185 W (V_{MP} = 19.35 V, I_{MP} = 9.5 A) while the output is for charging the battery only. There were no stability issues during the transitions. The response time is roughly 100 ms. As the input power decreased, the output power of the converter dropped accordingly. Charging current for the battery reduced from 6.6 A to around 6 A while the load from dc-bus was maintained at 0 A. Turning to the second example, the MPP was increased from 185 W (V_{MP} = 19.35 V, I_{MP} = 9.5 A) to 250 W (V_{MP} = 20 V, I_{MP} = 12.5 A) while the output is simultaneously charging the battery and supplying the load. As can be seen from Figure 5-22 (b), there were no stability issues and there was about 100 ms transient time. The battery charging current jumped from 2 A to 4 A while the load from dc-bus was kept at about 4A. When the converter reaches the MPP, the input voltage and current oscillate around the optimal value due implementation of the MPPT algorithm as described above.

CH1: OUTPUT LOAD, CH2: PV VOLTAGE, CH3: PV CURRENT, CH4: BATTERY CHARGING CURRENT

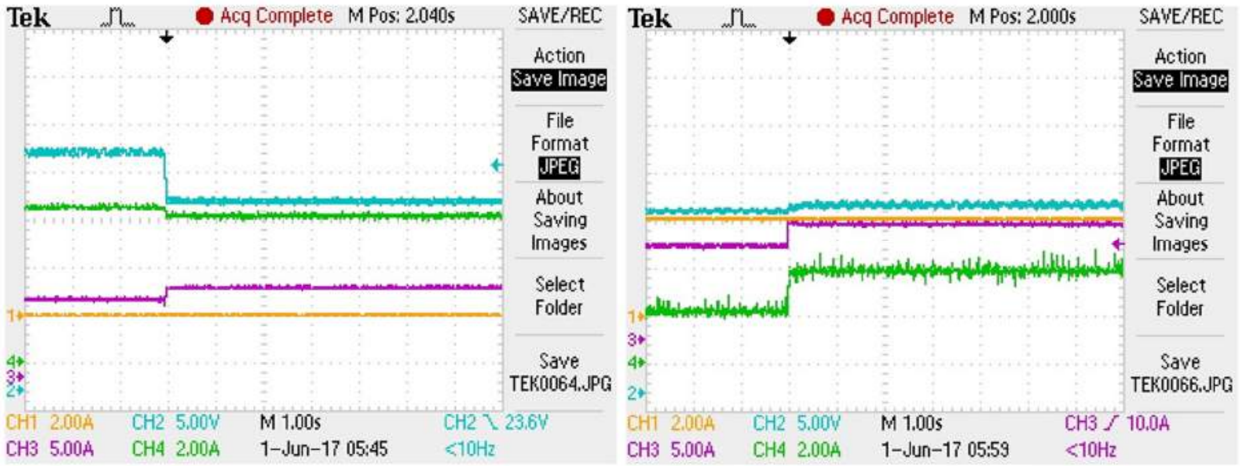

(a) MPP from 206W to 185W

(b) MPP from 185W to 206W

Figure 5-22. Response of the converter when the MPP of the PV input is changed

5.4.2. TB input MPPT

The results of MPPT over the possible power range for the emulated TB input are shown in Figure 5-23. The MPPs are obtained from the turbine speed-power curves (identified in in Figure 5-3), set with the variation of the dc supply voltage to the dc motor in the emulator. Due to the limitation of the turbine emulator, the measurement power was only up to nearly 95 W. The results show that the converter MPPT algorithm follows the MPP in the tests. The nature of P&O MPPT algorithm means there might be some small error inside the converter. It can be seen that the tracked power curve is slightly lower than the MPP in the range. However, these differences are quite small (less than 5 % of the total power). For example, at 100 V and MPP is around 80 W, there is only about 3 W differences between MPP and tracked power.

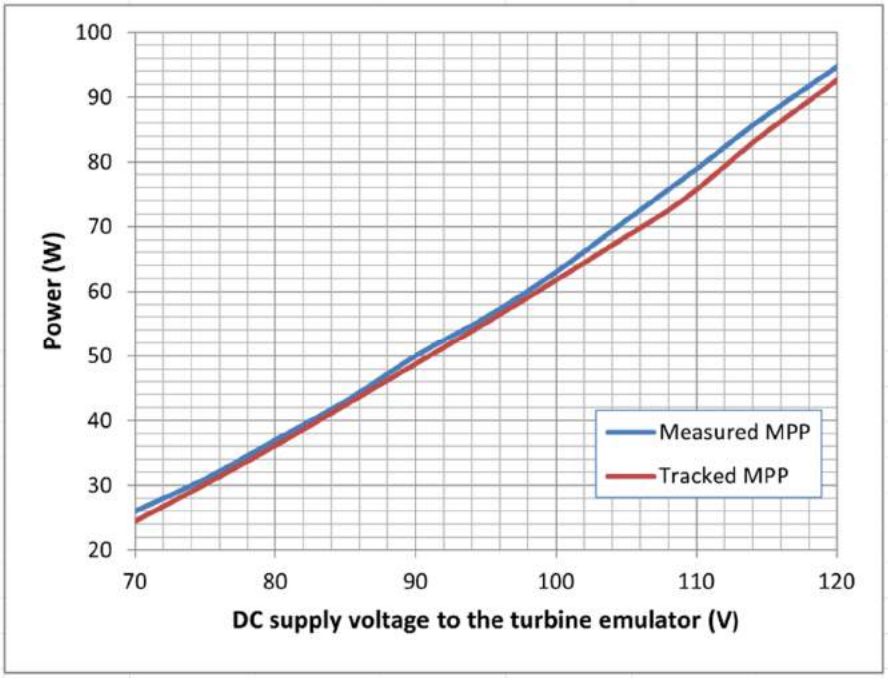

Figure 5-23. Tracked power vs. Set maximum power point of the TB input source

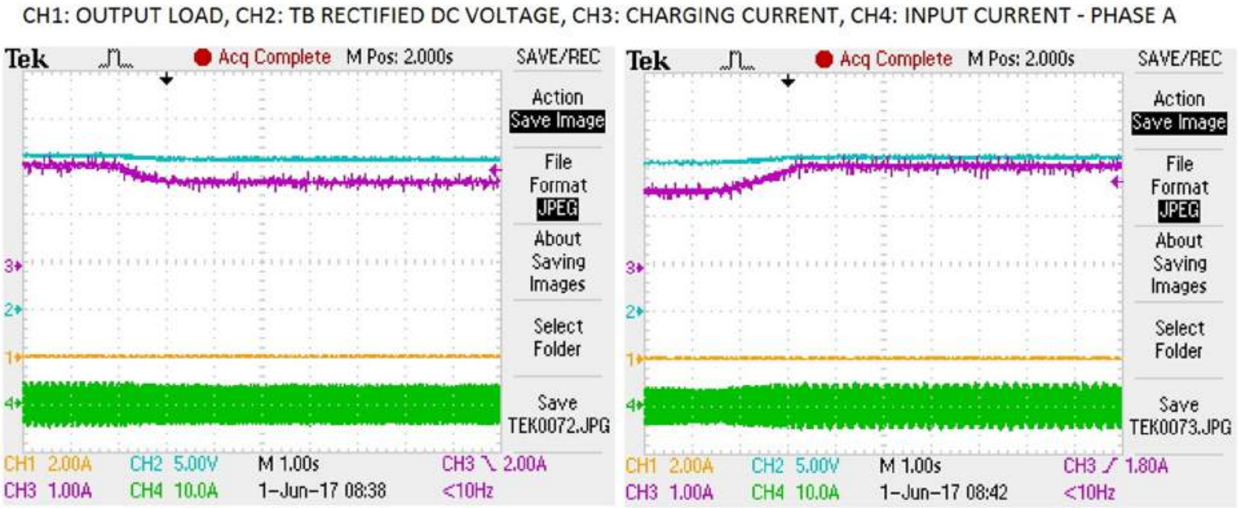
CH1: OUTPUT LOAD, CH2: TB RECTIFIED DC VOLTAGE, CH3: CHARGING CURRENT, CH4: INPUT CURRENT - PHASE A

(a) TB MPP from 63W to 55W

(b) TB MPP from 55W to 63W

Figure 5-24. Changing turbine's operation point

The response of the converter for changes in the turbine's conditions is shown in Figure 5-24. For the first measurement (Figure 5-24 (a)), the maximum power point is shifted from about 63 W to 55 W. The converter detects this change and reduces the input's current to the next MPP (see the small drop in the current value of Phase A – CH4). The DC value of input voltage on the output of the three-phase rectifier is also reduced due to this change (see the Light Blue line, CH2). A corresponding change is also observed on the output side, where the battery charging current – the Purple line CH3 – drops to about 1.75 A from 2 A. These changes take place over roughly 1s. There were no stability issues during the changing of MPP. The response of the converter to the opposite direction of change are also shown in Figure 5-24 (b), where the MPP is increased from 55 W to about 63 W. Similarly to the first example, the converter adapts to the situation in about 1s and there are no operational issues.

5.4.3. Both channels in MPPT mode

PV is maintained, TB varies while charging the battery

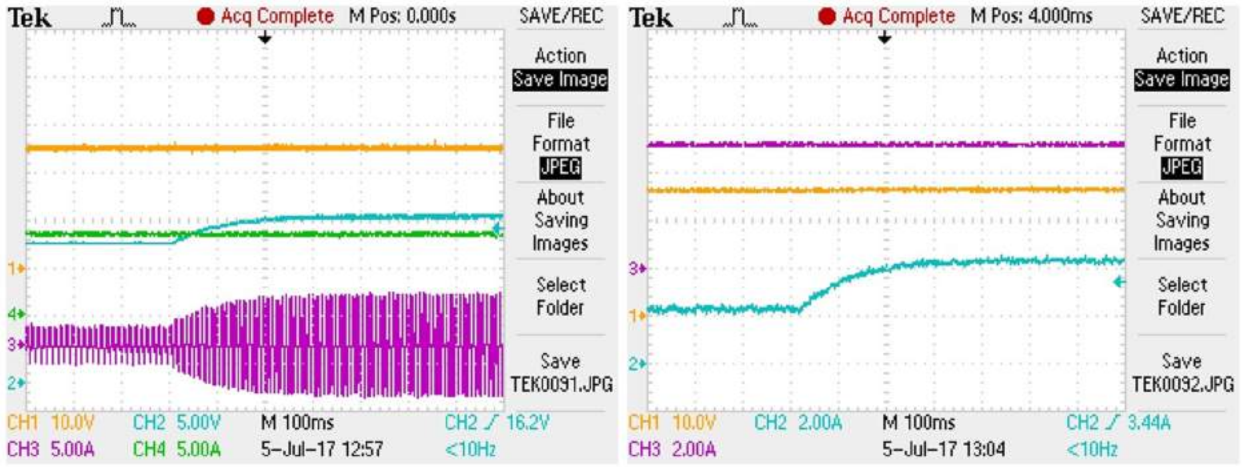

a) INPUTS WAVEFORMS
CH1: PV VOLTAGE, CH2: TB VOLTAGE (RECTIFIED DC)
CH3: TB CURRENT (ON PHASE A), CH4: PV CURRENT

b) OUTPUTS WAVEFORMS
CH1: DC-BUS VOLTAGE, CH2: CURRENT TO BATTERY
CH3: LOAD AT DC-BUS

Figure 5-25. The responses of the converter when the MPP of TB input is moving up (while the MPP of PV input is maintaining, and the battery is charging)

Both input channels are running in MPPT mode when the total combined input power is insufficient to satisfy both the output load and full battery charging current. As can be seen from Figure 5-25, the PV and TB inputs are running in MPPT mode. While the MPP of the PV is set and maintained at 200 W, the tracked power for this source is within 1 W of this value (see the Yellow line at 24.1 V and the Light Blue line at 8.3 A in Figure 5-25(a) for PV input voltage and current, respectively). The load that is taken from the dc-bus is also set to 5 A by the resistive load (see the Purple line - CH3 - on the output waveforms, Figure 5-25(b)). The MPP input of the turbine emulator is stepped from about 18 W to 80 W. The tracked input power is then automatically changed by the converter from 17.8 W to about 75 W for the TB input. The changes on input waveforms of the TB input are also captured in Figure 5-25(a), where the Light Blue trace – CH2 – represents rectified input voltage and the Purple trace – CH3 – represents input current on one phase of the turbine channel. In about 300ms of transient time, the rectified voltage of the TB source increases from about 16 V to 19 V, and the RMS input current increases from 2 A to about 5 A. On the output, during the same period, the battery charging current is increased from about 2.2 A to 4.2 A while the dc-bus voltage and its load are unchanged.

The opposite change in the MPP of the TB input is shown in Figure 5-26. The MPP of the PV input and load on the dc-bus are kept at the same level as with the previous test. The voltage supply to turbine emulator is step reduced and the tracked power reduces from about 75 W to 17.8 W on the TB input, while the tracked power for the PV input is still at 200 W. As can be seen on the inputs waveforms, the PV input voltage and current are maintained while those of the TB channel vary according to the MPP. On the output side, a decrease of the battery charging current from 4.2 A to 2.2 A is recorded.

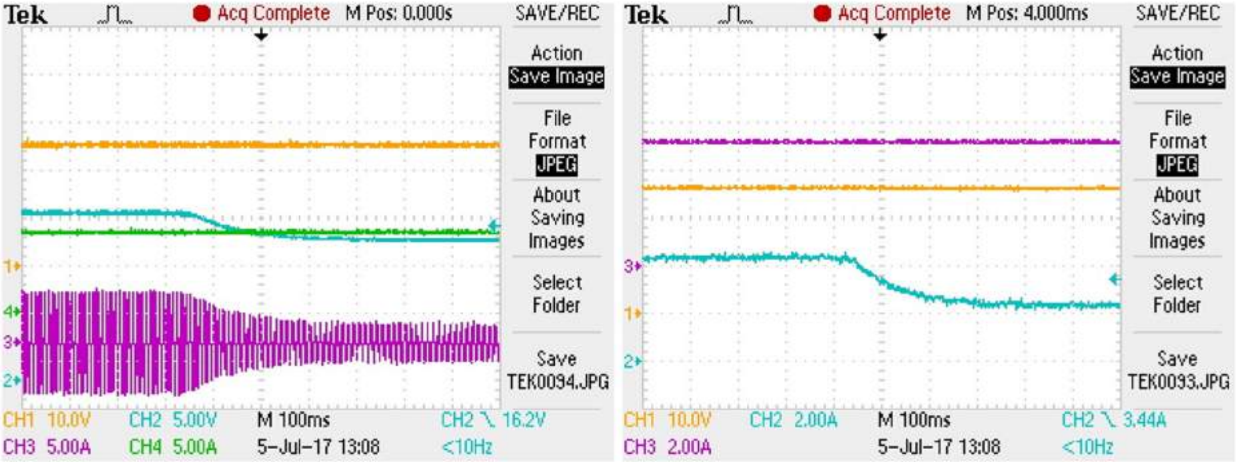

a) INPUTS WAVEFORMS

CH1: PV VOLTAGE, CH2: TB VOLTAGE (RECTIFIED DC)

CH3: TB CURRENT (ON PHASE A), CH4: PV CURRENT

b) OUTPUTS WAVEFORMS

CH1: DC-BUS VOLTAGE, CH2: CURRENT TO BATTERY

CH3: LOAD AT DC-BUS

Figure 5-26. The responses of the converter when the MPP of TB input is moving down (while the MPP of PV input is maintaining, and the battery is charging)

PV is maintained, TB varies while discharging the battery

a) INPUTS WAVEFORMS
CH1: PV VOLTAGE, CH2: TB VOLTAGE (RECTIFIED DC)
CH3: TB CURRENT (ON PHASE A), CH4: PV CURRENT

b) OUTPUTS WAVEFORMS
CH1: DC-BUS VOLTAGE, CH2: CURRENT TO BATTERY
CH3: LOAD AT DC-BUS

Figure 5-27. The responses of the converter when the MPP of TB input is moving up (while the MPP of PV input is maintaining, and the battery is turning from discharging to charging mode)

In this test, both channels are running in MPPT mode while a load of 6 A is taken from the dc-bus. Initially, the MPP for the PV and TB inputs are set at 200 W and 18 W, respectively. During this time, the battery is discharged at about -1 A (discharge identified by a negative current value) as the combined total input power is not enough to meet the load requirements alone (see Figure 5-27(b)). The MPP of the TB input is then increased to 80 W. The converter adjusts the TB input voltage and current accordingly in about 300 ms while it is still keeping the same tracked power level on the PV channel. Following these changes, the battery charging current is increased from -1 A through 0 A to 1.2 A (see the Light Blue trace – CH2, Figure 5-27(b)). The transition from discharging to charging of the battery has taken place in this short period without any disturbance of the converter's operation due to the change of the TB input.

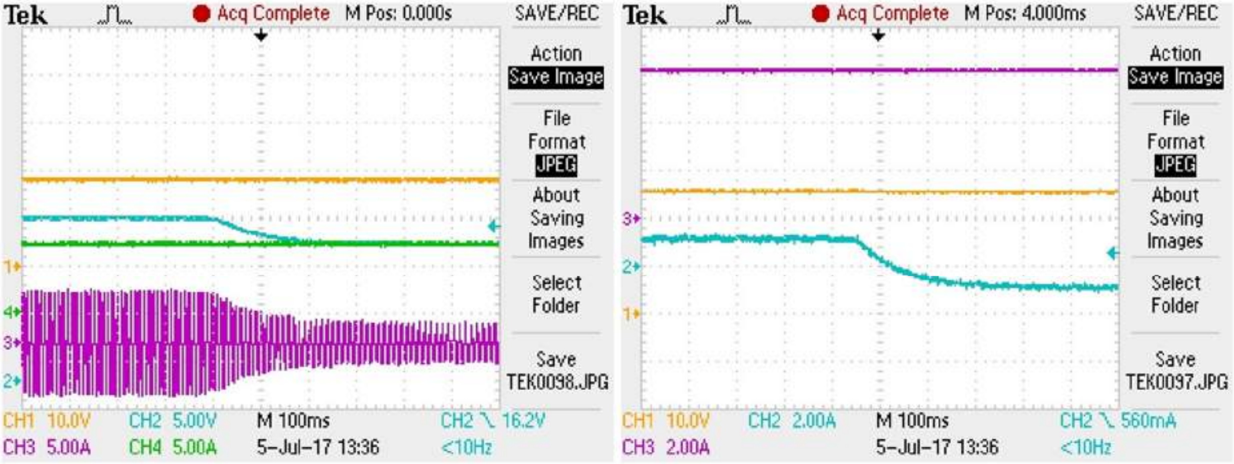

a) INPUTS WAVEFORMS
CH1: PV VOLTAGE, CH2: TB VOLTAGE (RECTIFIED DC)
CH3: TB CURRENT (ON PHASE A), CH4: PV CURRENT

b) OUTPUTS WAVEFORMS
CH1: DC-BUS VOLTAGE, CH2: CURRENT TO BATTERY
CH3: LOAD AT DC-BUS

Figure 5-28. The responses of the converter when the MPP of TB input is moving down (while the MPP of PV input is maintaining, and the battery is turning to discharging mode)

For the opposite change of the turbine's MPP, from 80 W back to 18 W, the converter adjusts its input current and voltage on the TB channel according to the new MPP (See inputs waveforms of both channels in Figure 5-28(a)). There is no abnormal behavior on these main signals while the battery changes from charge mode to discharge mode (see Figure 5-28(b)).

As a result, during MPPT mode on both input channels and with the TB input varying, the converter followed the MPP on the TB channel while it kept tracking the MPP of the PV input. The difference of input power is reflected on the battery charging current. Depending on the load level on the dc-bus, the battery can swap smoothly between discharging and charging mode during the changes of the TB input.

TB is maintained, PV varies while charging the battery

In this group of tests, the TB input channel was always running at about 60 W (tracked). The output load from dc-bus is set by an electronics load and is also kept at a constant level. By varying the MPP of the PV input, the reaction of converter was recorded, depending on the operation modes of the battery and the amount of load from the dc-bus.

Firstly, the MPP of the PV input source was varied from 207 W to 317 W while the TB input remains constant, and the load from dc-bus is kept at 5 A. As shown in Figure 5-29(a), the converter increases the PV input current and voltage according to the change of MPP on the PV channel while there is no change on TB channel. Due to the increase of the total input power, the battery charging current rose from 3.8 A to around 6.5 A. This current rise takes place in about 10 ms on both input and output signals. The tracked MPP is shifted from 206 W to 314 W on the

PV input. There is a very small (operationally insignificant) rise on dc-bus voltage, with no signs of abnormal reaction in the main signals of the converter.

Secondly, the MPP of PV input is reduced from 317 W back to 207 W. As can be seen from Figure 5-30, the input signals from the PV channel are changed according to the movement of MPP. The battery charging current also dropped to just under 3.85 A. Similar to the previous upward movement of the PV's MPP, the converter's main signals are stable.

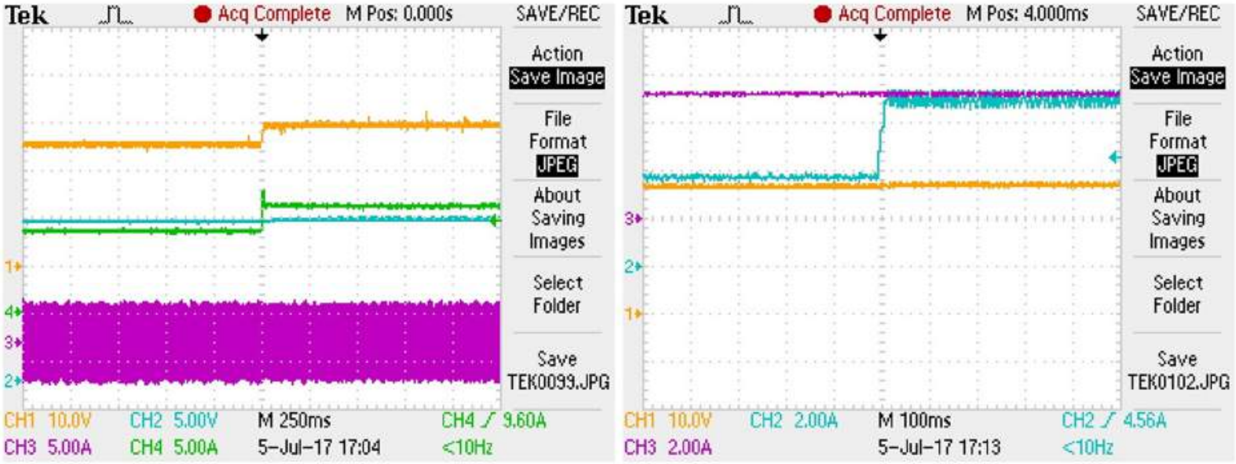

a) INPUTS WAVEFORMS
CH1: PV VOLTAGE, CH2: TB VOLTAGE (RECTIFIED DC)
CH3: TB CURRENT (ON PHASE A), CH4: PV CURRENT

b) OUTPUTS WAVEFORMS
CH1: DC-BUS VOLTAGE, CH2: CURRENT TO BATTERY
CH3: LOAD AT DC-BUS

Figure 5-29. The responses of the converter when the MPP of PV input is moving up (while the MPP of TB input is maintaining, and the battery is charging)

It was shown that the converter adjusts the PV channel to follow the MPP of that input source while it keeps the tracked value of MPP on the unchanging TB input. The changing amount of total input power is reflected in the changing battery charging current.

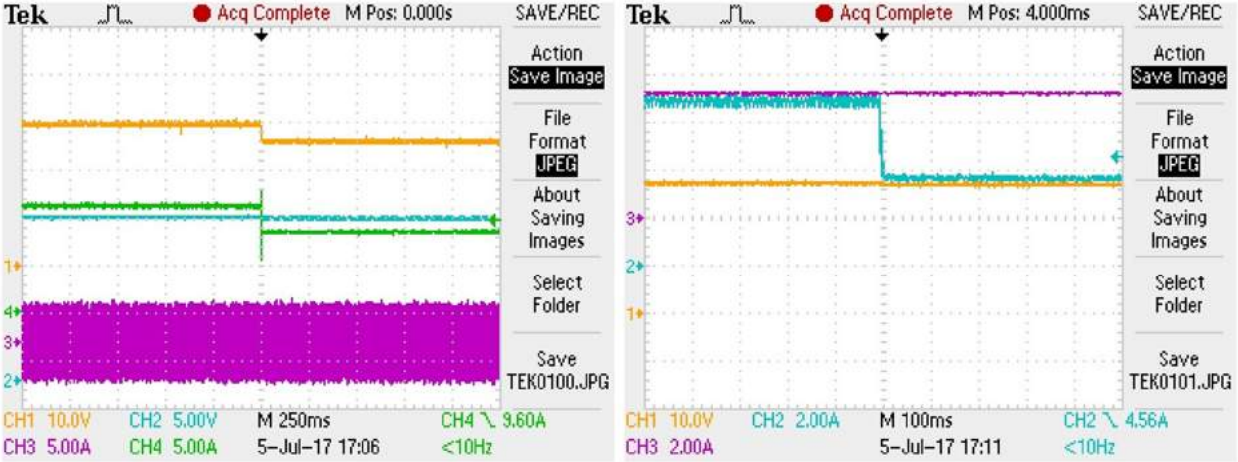

a) INPUTS WAVEFORMS
CH1: PV VOLTAGE, CH2: TB VOLTAGE (RECTIFIED DC)
CH3: TB CURRENT (ON PHASE A), CH4: PV CURRENT

b) OUTPUTS WAVEFORMS
CH1: DC-BUS VOLTAGE, CH2: CURRENT TO BATTERY
CH3: LOAD AT DC-BUS

Figure 5-30. The responses of the converter when the MPP of PV input is moving down (while the MPP of TB input is maintaining, and the battery is charging)

TB is maintained, PV varies while discharging the battery

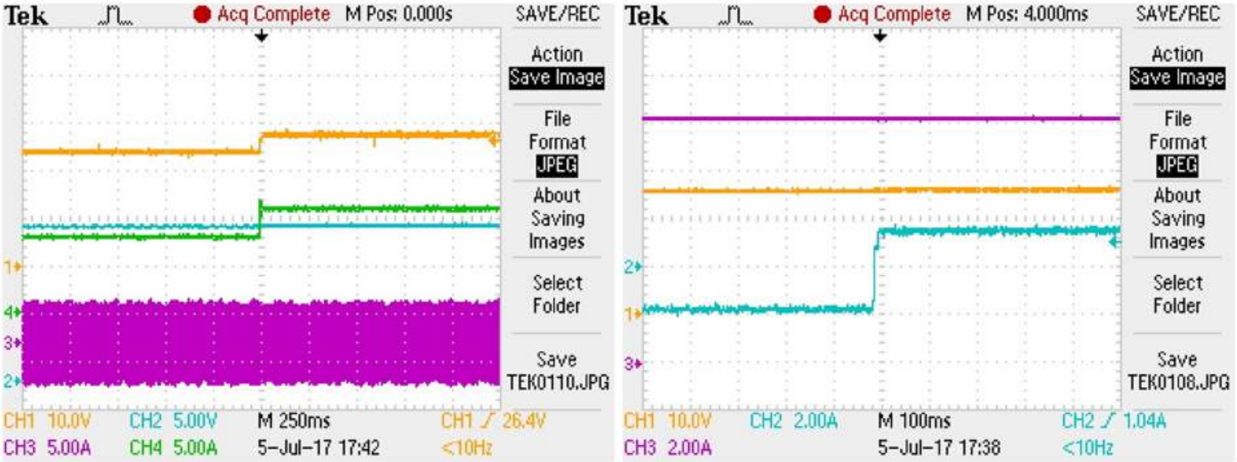

a) INPUTS WAVEFORMS
CH1: PV VOLTAGE, CH2: TB VOLTAGE (RECTIFIED DC)
CH3: TB CURRENT (ON PHASE A), CH4: PV CURRENT

b) OUTPUTS WAVEFORMS
CH1: DC-BUS VOLTAGE, CH2: CURRENT TO BATTERY
CH3: LOAD AT DC-BUS

Figure 5-31. The responses of the converter when the MPP of PV input is moving up (while the MPP of TB input is maintaining, and the battery is turning from discharging to charging mode)

For this set of tests the load from dc-bus was increased to a level higher than the combined input sources could supply, therefore, the battery was discharging to compensate for this power shortfall. The MPPT mode was still running on both channels in this case. Again, these tests were conducted by moving the MPP of the PV input while the TB input was held constant.

The MPP of the PV channel was initially increased from 207 W to 317 W. Figure 5-31 shows the reaction of the main input and output signal waveforms of the converter. The input signals follow the MPP of each power source as designed, maintaining the TB input values and adjusting the PV input values to the new level. On the output side, the battery shifted smoothly from discharging mode (-2 A) to charging mode (1.6 A) in a short period of time (less than 20 ms). In the meantime, the dc-bus voltage and its load are unchanged, staying at 26 V and 10 A, respectively.

When the PV’s MPP was reduced, the converter’s main signals changed in the appropriate directions (see Figure 5-32). There was no abnormal reaction on those signals. The PV input was reset to the lower MPP of 207 W from 317 W. As the signals of the PV source moved to the new MPP, the battery changed from charging mode to discharging mode.

To conclude, due to the presence of the battery, there was no disruption to the load on the dc-bus. The battery either discharged to compensate for the lack of power when the total input power is insufficient, or was charged when the total input power was higher than the load. In this situation, both inputs were running in MPPT mode. If the PV input varies its MPP, the battery transitions easily between charging and discharging mode.

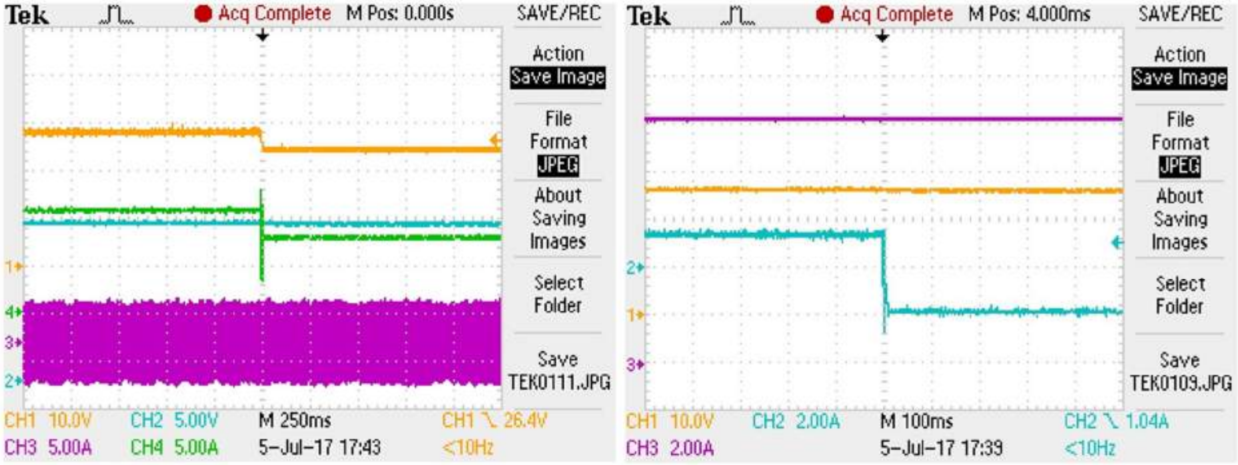

a) INPUTS WAVEFORMS
CH1: PV VOLTAGE, CH2: TB VOLTAGE (RECTIFIED DC)
CH3: TB CURRENT (ON PHASE A), CH4: PV CURRENT

b) OUTPUTS WAVEFORMS
CH1: DC-BUS VOLTAGE, CH2: CURRENT TO BATTERY
CH3: LOAD AT DC-BUS

Figure 5-32. The responses of the converter when the MPP of PV input is moving down (while the MPP of TB input is maintaining, and the battery is turning from charging to discharging mode)

Output load response when both input channels are in MPPT mode

For this set of tests, both input sources were set at a level such that the converter operated in MPPT mode. The TB emulator was running at a MPP of 18 W and the PV input was set at a MPP of 207 W. The load from dc-bus was step-changed in this case. As can be seen from Figure 5-33, the inputs signals from both channels are unchanged when the load from dc-bus rises rapidly from 5 A to 10 A. The total input power is unchanged as the converter is tracking its unmoved MPP input sources. On the other hand, the battery changed quickly from charging mode to discharging mode as the total input power becomes lower than the increased load requirements. There is a slight drop in dc-bus voltage after the change.

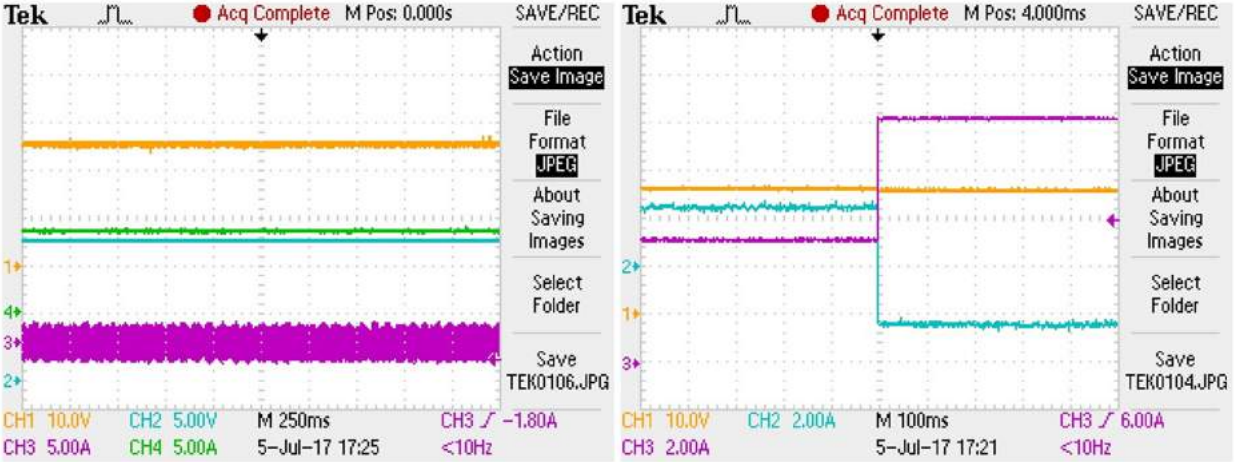

a) INPUTS WAVEFORMS
CH1: PV VOLTAGE, CH2: TB VOLTAGE (RECTIFIED DC)
CH3: TB CURRENT (ON PHASE A), CH4: PV CURRENT

b) OUTPUTS WAVEFORMS
CH1: DC-BUS VOLTAGE, CH2: CURRENT TO BATTERY
CH3: LOAD AT DC-BUS

Figure 5-33. Output load response of the converter during MPPT mode (the dc-bus load is rose rapidly from 5 A to 10 A)

a) INPUTS WAVEFORMS
CH1: PV VOLTAGE, CH2: TB VOLTAGE (RECTIFIED DC)
CH3: TB CURRENT (ON PHASE A), CH4: PV CURRENT

b) OUTPUTS WAVEFORMS
CH1: DC-BUS VOLTAGE, CH2: CURRENT TO BATTERY
CH3: LOAD AT DC-BUS

Figure 5-34. Output load response of the converter during MPPT mode (the dc-bus load is reduced rapidly from 10 A to 5 A)

For the opposite direction of load change, the dc-bus load decreases from 10 A to 5 A (see Figure 5-34). In this case, there was also no change on the input side of the converter when the MPP of both sources were kept constant. The battery then moved back to charging mode from discharging. A minor rise in the dc-bus voltage appears. Again, there was no abnormal reaction of the converter.

To sum up, during MPPT mode on both inputs, there were no significant observed changes to the input signals when the output load is varied. Depending on the total amount of available input power, the battery can transition between either charging or discharging mode.

5.5. TRANSITING BETWEEN OPERATION MODES

The previous results confirm that the converter operates appropriately in MPPT, CV, and CC mode. In the real applications, however, there will be some transient time between these operation modes. For example, during the battery charging procedure, the converter will switch from MPPT mode to CC mode or CV if the input sources can provide more power than the load and the battery need together. Depending on the battery state of charge and the amount of load on the dc-bus, either the CC mode or CV mode is activated. The following detailed tests concentrate on the converter response at the transitions between these operational modes.

5.5.1. MPPT and CC mode

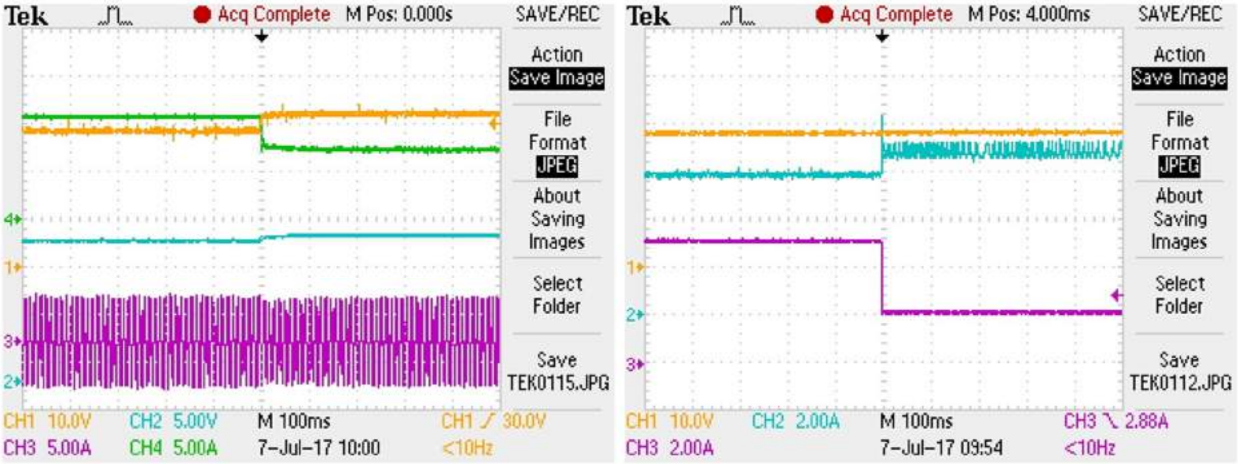

a) INPUTS WAVEFORMS
CH1: PV VOLTAGE, CH2: TB VOLTAGE (RECTIFIED DC)
CH3: TB CURRENT (ON PHASE A), CH4: PV CURRENT

b) OUTPUTS WAVEFORMS
CH1: DC-BUS VOLTAGE, CH2: CURRENT TO BATTERY
CH3: LOAD AT DC-BUS

Figure 5-35. MPPT mode to CC mode (when the load from the dc-bus step-decreases)

In the tests of the transition between MPPT and CC mode (constant current battery charging), the MPP for the PV and TB inputs were set at 287 W and 65W, respectively. The load on the dc-bus was varied to change the converter's operation mode as the total available input power becomes higher than output power demand.

As shown in Figure 5-35(a) and (b), on the left-hand side of the oscilloscope capture, the converter is running in MPPT mode, where the tracked power of the PV source is 284 W and the TB input is 63 W. The battery is being charged by a current of 6 A while the dc-bus is supplying a load of 5 A (set by the electronic resistive load). Meanwhile, the voltage value on dc-bus and the battery is at 26.8 V. By step reducing the load on the dc-bus to 2 A, the measured power from the input sources falls to 222 W and 62 W for the PV and TB sources respectively. The change of input voltage and current for each source is also shown in Figure 5-35(a), where both voltage amplitudes increase and both current values decrease. On the output side, as the availability of power, the charging current to the battery increase and peak to about 8.4 A at the moment of load changing (see Figure 5-35(b)). After the short transient peak, the charging current is stable around the constant charging current value of 6.5 A. The observed increased battery charge current fluctuation once in CC mode is due to the stored energy in the output inductor and the transient between two control loops. There is a slight increase in the voltage of dc-bus.

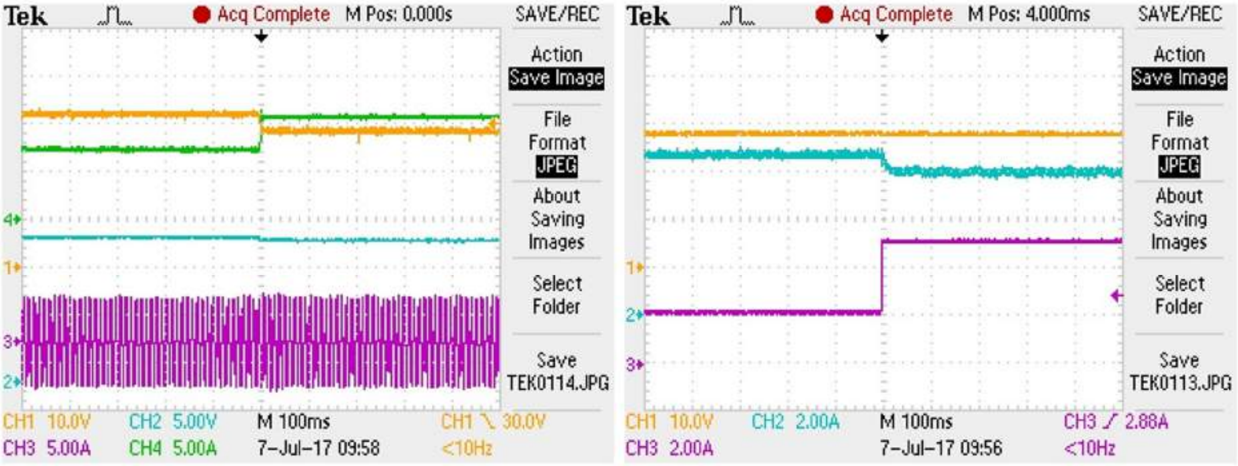

a) INPUTS WAVEFORMS
CH1: PV VOLTAGE, CH2: TB VOLTAGE (RECTIFIED DC)
CH3: TB CURRENT (ON PHASE A), CH4: PV CURRENT

b) OUTPUTS WAVEFORMS
CH1: DC-BUS VOLTAGE, CH2: CURRENT TO BATTERY
CH3: LOAD AT DC-BUS

Figure 5-36. CC mode to MPPT mode (when the load from the dc-bus increases rapidly)

The load on the dc-bus was then increased back to 5 A to force the converter back into MPPT mode. As can be seen from Figure 5-36(a), the converter alters its input voltage and current on each channel to satisfy the MPP value (283 W and 62 W for the PV and TB inputs, respectively). The battery charging current is then decreased from 6.5 A to around 6 A.

In both instances of transiting from MPPT mode to CC mode and vice versa, the response of converter has been shown to be fast and smooth. The converter switches between these modes in around 10ms, and there is no abnormal behavior on the main signals.

5.5.2. MPPT and CV mode

For these tests the converter was set initially running in MPPT mode, where the MPP for the PV source is 287 W and the TB source is 65 W, and the load on the dc-bus is 5 A while the battery is being charged at 6 A. The battery is then disconnected from the battery port, which means there is no required charging current. As shown in Figure 5-37, the dc-bus voltage jumped up to the stable value of 26.7 V from 25.6 V while the load on the dc-bus remained at 5 A. A spike of about 29 V can be seen on the dc-bus right after disconnecting the battery, however, this output is then regulated at the desired value of 26.72 V. As the converter reduces the current from both inputs for the CV mode (regulating the output voltage), the increase of the input sources voltage is observed. Measured input powers from these sources after the battery was disconnected are 100 W and 62 W for the PV and TB channels, respectively. The transient time for transition from MPPT to CV mode is around 20ms.

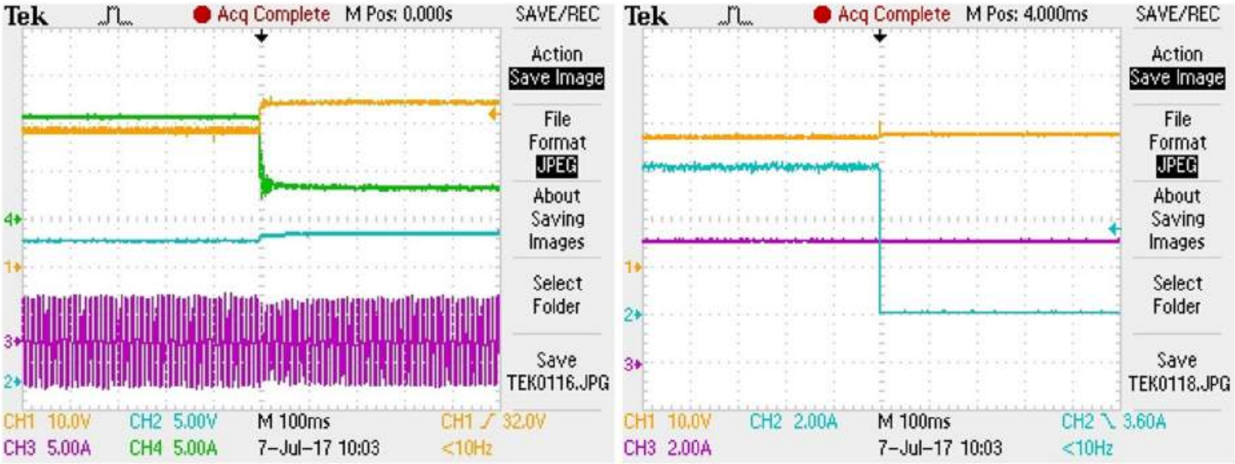

a) INPUTS WAVEFORMS
CH1: PV VOLTAGE, CH2: TB VOLTAGE (RECTIFIED DC)
CH3: TB CURRENT (ON PHASE A), CH4: PV CURRENT

b) OUTPUTS WAVEFORMS
CH1: DC-BUS VOLTAGE, CH2: CURRENT TO BATTERY
CH3: LOAD AT DC-BUS

Figure 5-37. MPPT to CV mode (when the battery is disconnected)

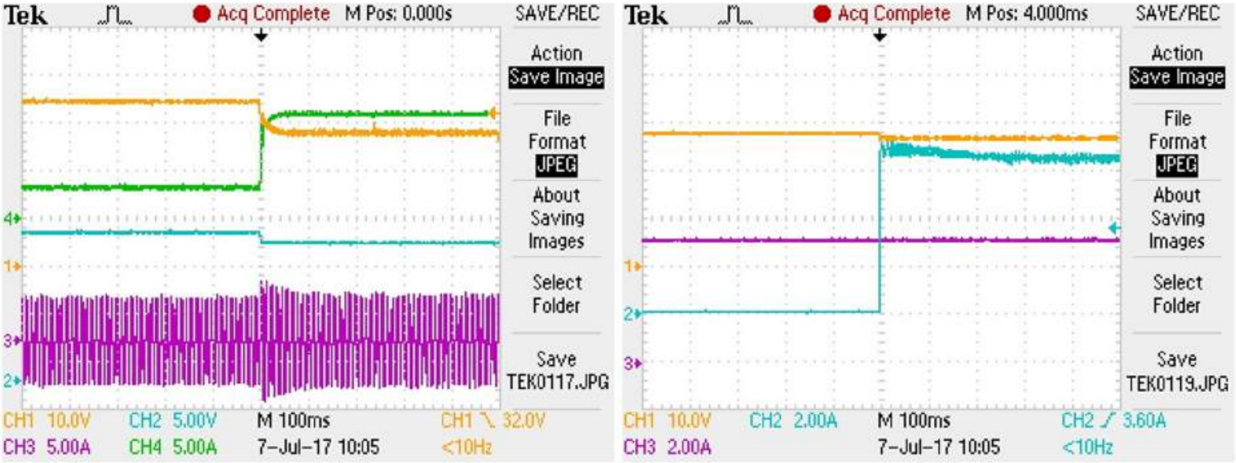

a) INPUTS WAVEFORMS
CH1: PV VOLTAGE, CH2: TB VOLTAGE (RECTIFIED DC)
CH3: TB CURRENT (ON PHASE A), CH4: PV CURRENT

b) OUTPUTS WAVEFORMS
CH1: DC-BUS VOLTAGE, CH2: CURRENT TO BATTERY
CH3: LOAD AT DC-BUS

Figure 5-38. CV to MPPT mode (when the battery is connected)

On the second test, the converter was initially running in CV mode when there is no connected battery. The output voltage is regulated at the default value (26.72 V). Although the MPP of the PV and TB sources were set at 287 W and 65 W respectively, the measured power for these inputs were 100 W and 61 W, respectively. The battery was then connected to the battery port of the converter. In response to the increased requirement of output current for charging the battery, the converter draws more power from its inputs. However, the total amount of total input power is insufficient to charge the battery at its set constant current. As can be seen from Figure 5-38, therefore, the converter switches to MPPT mode. The input currents from both channels are increased by the converter to reach the MPPs in about 50 ms. Meanwhile, the input voltages also dropped when transitioning to the MPPs. On the output, the charging current to the battery increases quickly to about 7 A in less than 10 ms, and then this value decreases gradually to the stable level at about 6.5 A in the next 200 ms. While the electronic load is kept at 5 A, a drop of the dc-bus voltage from 26.72 V to 25.5 V is recorded when the battery is connected.

With the test representing the worst case scenario of connecting/disconnecting the battery, the response of the converter was appropriate. On these events, the converter switches reliably between MPPT and CV mode without any issues.

5.5.3. CC and CV mode

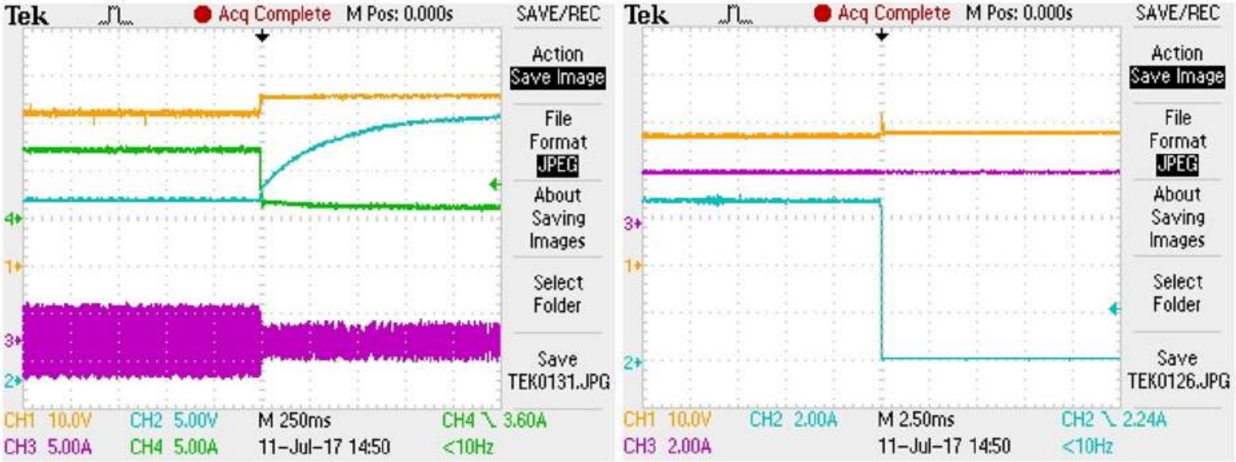

a) INPUTS WAVEFORMS
CH1: PV VOLTAGE, CH2: TB VOLTAGE (RECTIFIED DC)
CH3: TB CURRENT (ON PHASE A), CH4: PV CURRENT

b) OUTPUTS WAVEFORMS
CH1: DC-BUS VOLTAGE, CH2: CURRENT TO BATTERY
CH3: LOAD AT DC-BUS

Figure 5-39. CC to CV mode (when the battery is disconnected)

For real application, the transitioning from CC to CV mode takes place in the battery charging process only. These events will occur slowly when the battery reaches its constant voltage threshold and then the charging current will reduce gradually while charging. It is quite hard to capture this transition event in normal application operation. However, to demonstrate these transitions of the converter between CC and CV mode, the worst case scenario of disconnecting/connecting the battery from/onto the converter is used (something that could also conceivably happen in actual operation).

For the first test, the converter runs at constant current charging mode for the battery while a load of 2 A is being supplied by the dc-bus. The MPP of input sources is set at 287 W and 65 W for the PV and TB sources, respectively. As the total output power is lower than the available power from the input sources, the converter is only taking 214 W from the PV input and 61 W from the TB input. As shown in Figure 5-39, when the battery is disconnected, the dc-bus voltage jumps from 25.6 V up to 26.7 V. There is a short transient peak voltage of 30 V of about 250 ns duration. At the same time, the battery charge current drops from 6.5 A to 0 A while the load on the dc-bus is maintained. At the input side, the current decreases and the voltage increases in both channels. The rate of change of input current and voltage of the TB channel appears to be slower than those of the PV channel (about 25 ms and 1 s, respectively). The input power value after the change is 38 W and 31 W for the PV and TB inputs, respectively.

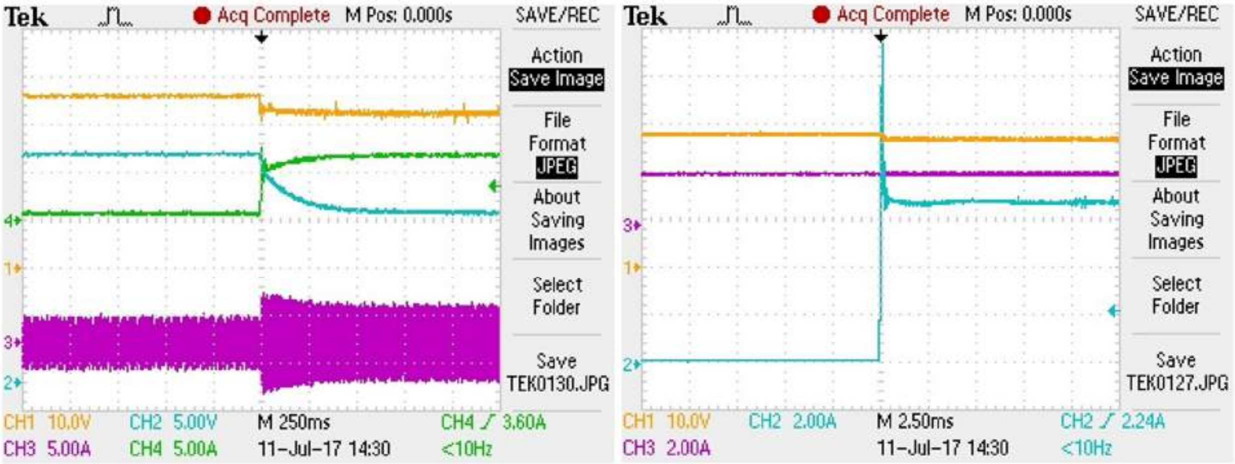

a) INPUTS WAVEFORMS
CH1: PV VOLTAGE, CH2: TB VOLTAGE (RECTIFIED DC)
CH3: TB CURRENT (ON PHASE A), CH4: PV CURRENT

b) OUTPUTS WAVEFORMS
CH1: DC-BUS VOLTAGE, CH2: CURRENT TO BATTERY
CH3: LOAD AT DC-BUS

Figure 5-40. CV to CC mode (when the battery is connected)

In the opposite case, the battery is connected to the converter while it is regulating the dc-bus voltage at 26.72 V (see Figure 5-40). The electronic load on the dc-bus is kept at 2 A. Before the battery connection, although the MPP is set at 287 W and 65 W, for the PV and TB sources respectively, the converter is only taking 20.5 W from the PV source and 50.5 W from TB source, respectively. Immediately after the battery connection, the charging current jumps to the constant current charging level of 6.5 A, and the dc-bus voltage drops to 25.6 V. There is a significant (but short) spike on the charging current to the battery, which reaches nearly 14 A during that transient time. After about 250 ns, the battery charging current is regulated at its desired value of 6.5 A. Following the increase of the converter power demand, input voltages and currents also change to their respective levels (giving 206 W and 62 W of input power from the PV and TB sources respectively).

These tests show that the converter switches appropriately between CC and CV mode in the worst case scenario of having the battery either connected or disconnected from the output of the converter. However, in real applications, the battery is rarely unplugged or plugged into the converter while it is running. Therefore, it is reasonable to conclude that the converter will transition properly between CV and CC mode under all normal operating conditions.

5.6. PROTECTION FUNCTIONS

The previous tests show that the converter operates properly in all conditions and there is no unstable behavior. This indicates that it is likely all the equipped protection blocks are working. The converter has been put into extreme conditions to test and confirm these functional protection blocks.

UVLO (Under-voltage lockout): This block shuts down the converter when the input voltage is not high enough for proper operation. Each input voltage is swept slowly from 0 V, the converter has been designed to turn on at 16.6 V for the PV source and 16.2 V for the TB source. When slowly reducing the input voltage from normal operation condition, measurements show the converter turns off at 15.9 V and 15.3 V for the PV and TB input, respectively. As the resistor pairs of UVLO setting level in TB channel have been changed for its low input voltage range of the turbine emulator, there are differences from the UVLO value of TB channel to those of PV channel.

OVP (Over-voltage protection): This function includes high input supply voltage and high output voltage. The converter shuts down its corresponding channel when the input voltage on each source exceeds 64 V, and turns that channel back on when the input voltage drops to below 62.8 V. If the output voltage (dc-bus) is higher than 30.2 V, the protection circuit will send a signal to turn off all switching transistors and force a full-bridge controller restart.

To test the battery over discharge protection function, a 24 V, 75 Ah Lead-acid battery was connected to the battery port and then discharged via the dc-bus by a resistive load. When the battery voltage is higher than 20.66 V, the dc-bus and the battery are connected normally, and the load resistance can be varied freely by the programmable electronic load. As the battery continues to discharge, its voltage drops. The protection circuit was observed to activate and disconnects the battery from dc-bus when the battery voltage is lower than 20.66 V. When the battery recovers its voltage, the battery and dc-bus were seen to reconnect at 20.85 V.

Each full-bridge controller has an integrated cycle-by-cycle current limit comparator to protect the converter. Additionally, when the controller detects an overcurrent occurring continuously, it will jump into hiccup mode to prevent the possible destruction of the converter. To confirm this function, shorting of the output circuit (dc-bus) to ground was carried out. As can be seen from Figure 5-41(a), the dc-bus was tied to ground while the PV source was supplying 2 A to the load. The output current increased rapidly to more than 50 A and the output voltage dropped to nearly 10 V. The input current also increased rapidly. After about 6ms, a shutdown occurs and the PWM pulses to the switching transistors cease, and therefore the output current falls to 0 A. The shutdown pulse lasts 10 ms and then the controller generates PWM signals again to bring up the output voltage. In the next 8 ms, however, the current is still above the limiting value and the controller turns back to the shutdown pulse mode. This loop continues until the short circuit is removed from the output. There was no damage or any issues for the converter after the test. The TB channel was also tested in a similar way. The dc-bus is shorted circuit when the TB emulator is running at a MPP of 65W and supplying 1 A to the output electronic load (see Figure 5-41(b)). Similarly to the PV channel test, the controller jumps to hiccup mode until the output is removed from the short circuit. There was no destruction or impairment to the converter for this test as well.

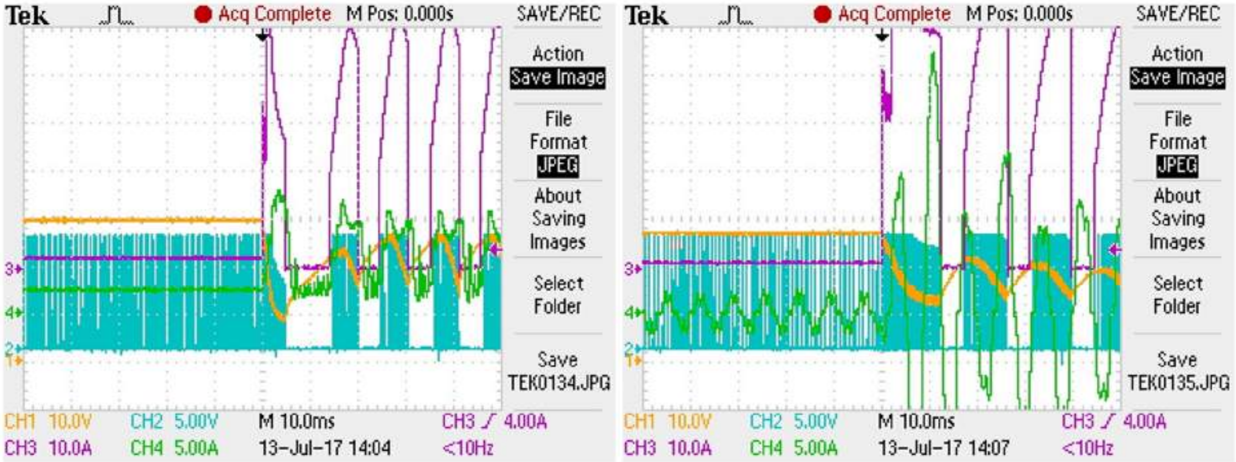

a) PV INPUT
CH1: OUTPUT VOLTAGE (DC-BUS), CH2: PWM SIGNAL,
CH3: OUTPUT CURRENT, CH4: INPUT CURRENT

b) TURBINE INPUT
CH1: OUTPUT VOLTAGE (DC-BUS), CH2: PWM SIGNAL,
CH3: OUTPUT CURRENT, CH4: INPUT CURRENT

Figure 5-41. Current limit functional test results (response of the converter due to the dc-bus being short circuited)

5.7. WORKING TEMPERATURE

Similar to many other high power converters, a certain amount of heat is generated while this converter is operating. Therefore, this heat needs to be dissipated properly in order to keep all components in their safe working temperature range. There are four heat sinks used in the converter, which are mounted on the main hotspots (primary switches, and secondary rectifying diodes of each channel). A small fan (24 V, 0.15 A) is also mounted on the board to generate a strong airflow for better heat dissipation at higher power conversion states. This fan is supplied directly from the dc-bus. Ideally, these heat sinks and the fan will keep the temperature of the converter as close as possible to room temperature. In the first design, the temperature profile can be calculated or simulated by appropriate design tools. However, the converter needs to be verified by a temperature profile measurement when it is fully physically formed. Depending on the test outcomes, the converter might need to be adjusted, such as to add more heat sink material and realigning of power devices.

As can be seen in Figure 5-42, there are some hotspots that appear when the input power is only from PV source and the output load is 15 A. The temperature on the activated channel side is higher than that of the unpowered side. The highest temperature spot is 59 ^{o}C at the gate driver ICs, mounted on the bottom side of the PCB. The second hotspot is on the input current sensing resistor, which reaches a temperature of 45.5 ^{o}C. The output inductor is also a noticeable hotspot. The temperature on the main power devices is in the normal operation range with the supporting of heat sink elements.

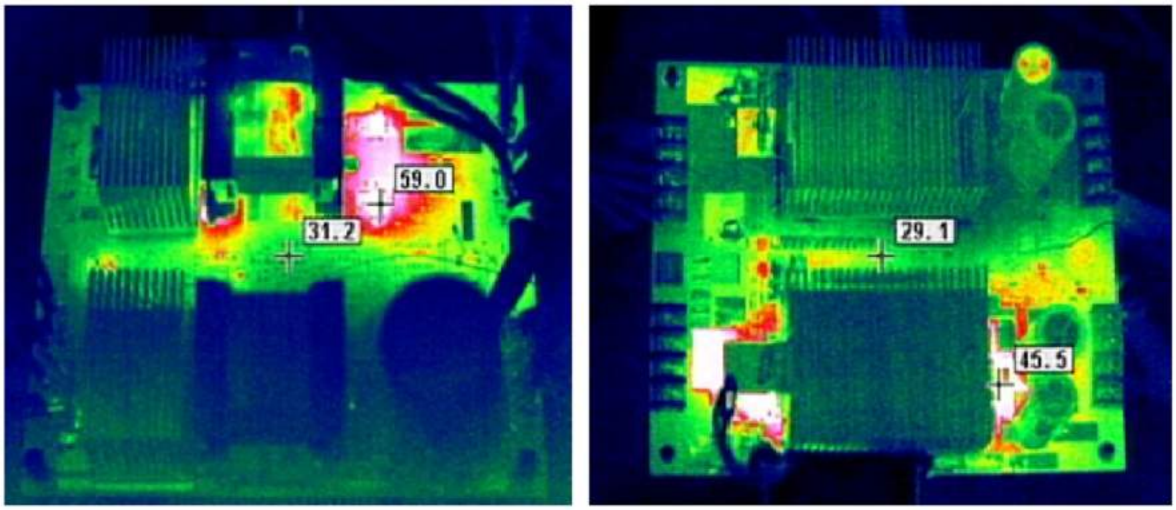

(a) Bottom side (b) Top side

Figure 5-42. Temperature profile of the converter (PV activated, output load = 15A)

In the case of only the TB channel being powered and the converter providing 15A to the output load, the temperature hot-spots appear on the TB channel only. As can be seen from Figure 5-43, the temperature is in the normal range for components that have heat sinks mounted. Similar to the PV channel, hotspots can be seen at the gate driver ICs, current sensing resistor and output inductor. The highest temperature is on the gate driver ICs, which reach 68.3 ^{o}C. A new high-temperature spot for the TB channel is at the input rectifier diodes. As no heat sink is mounted on this area, the temperature of the TB rectifier area rises to around 50 ^{o}C.

When both channels are sharing the power to source an output load of 15 A, a drop in temperature of the hot spots in each channel is recorded. In the TB channel, for example, a reduction of about 8 ^{o}C and 15 ^{o}C is observed on the gate driver ICs and input rectifier, respectively.

For better performance and reliability, the converter needs to have more heat sinks or other cooling methods for reducing its operational temperature. For example, heat sinks could be added on the input rectifier diodes and gate driver ICs. If there is a possibility of design revision, the current sensing resistors can be reduced in resistance value. There should also be good control and calculation on the thickness, width and the length of the copper traces from input capacitors to switching nodes.

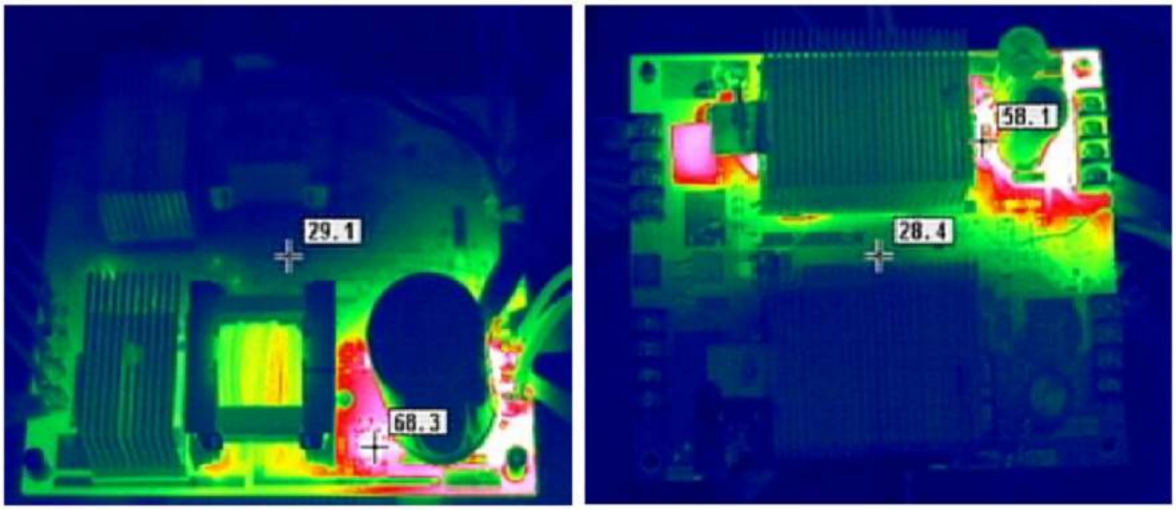

(a) Bottom side (b) Top side

Figure 5-43. Temperature profile of the converter (TB is activated, output load = 15 A)

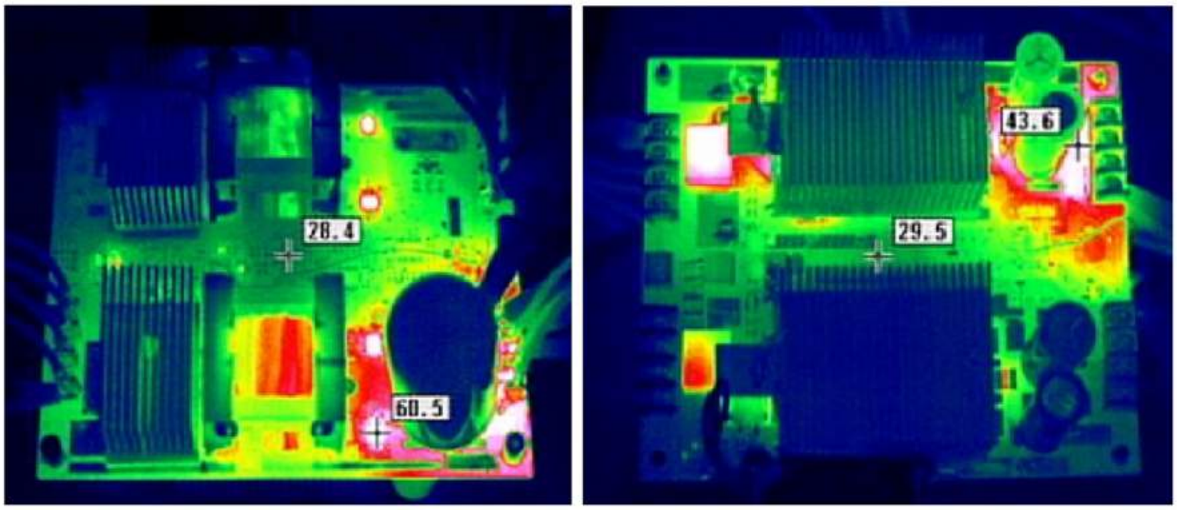

(a) Bottom side (b) Top side

Figure 5-44. Temperature profile of the converter (Both channels are activated, output load = 15 A)

5.8. MAXIMUM INPUT POWER CAPABILITY

The converter appears to be operating normally in all expected steady and dynamic states. Due to the mentioned heat dissipation issue and the limitation of input power sources, the maximum power capability of this converter has not been tested. That is the condition that both inputs are supplying the designed maximum input power (1 kW on each).

For a single input source situation, the PV channel has been tested to its power capacity of 1 kW (see Figure 5-20 and Figure 5-21). Regarding the TB channel, the turbine emulator was not suitable for the demanding of power higher than 100 W. It was also not possible to test this channel at high input power because the power limitation of the available 3-phase ac power supply. As shown in Figure 5-45, the highest available input power that has been tested on the TB input was about 400 W. Before the input power supply shutdown, the TB channel was generating 26.72 V and providing about 12.5 A load at the dc-bus. Turning to the design of the converter, the only difference between the TB channel and PV channel is the addition of the 3-phase rectifier. From the dc voltage output of the rectifier to output of the converter, the configuration and design are the same for both channels. As such, it is reasonable to expect that the TB channel can achieve a similar power rating to that of PV channel.

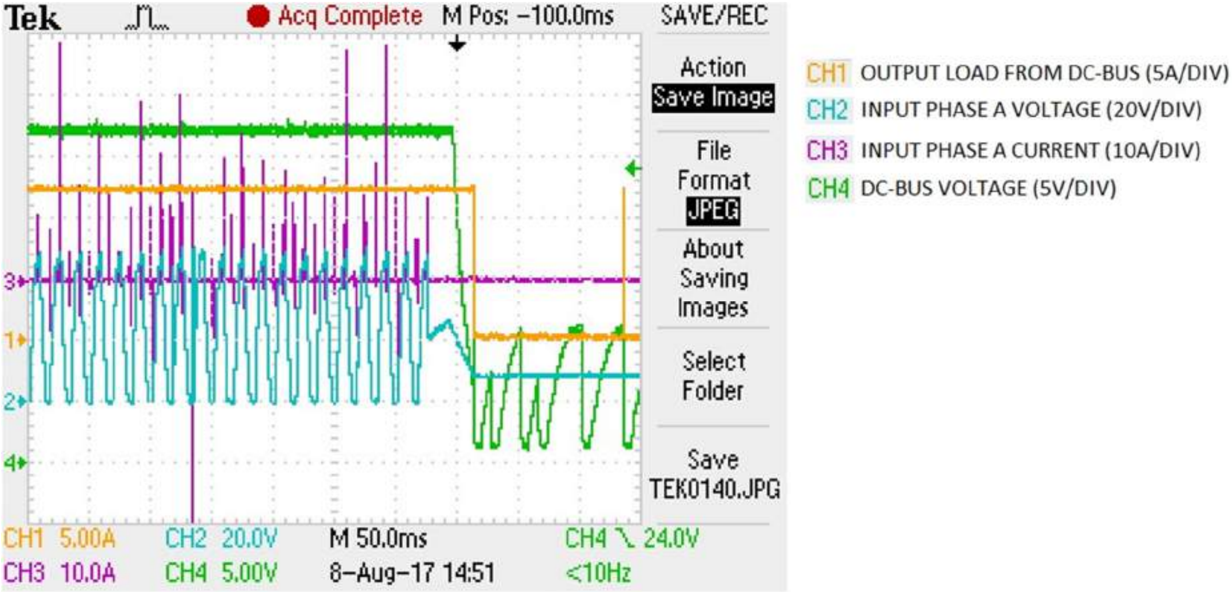

Figure 5-45. The 3-phase ac power supply shutdown when the converter is consuming about 400 W of power on the TB input

In the previous tests of two inputs simultaneously running, the maximum power of the PV source at the converter input was 650 W (see Figure 5-11) and the maximum power of the TB channel was 330 W (see Figure 5-12 - due to the limitation of the 3-phase ac power supply). Because the ratio of power from each input to the output is highly dependent on the value of those input voltages (same PWM duty cycle control for both channels), the power flow of each channel when the converter is running in the CC or CV mode are mostly imbalanced. Therefore, it is not easy to test the total maximum power rating in the case of the converter taking 1 kW input power from each source simultaneously to the output with ordinary power supplies in CV mode. The proper way is to test these parameters in MPPT mode, where the MPP is set at 1 kW for both sources. Again, this test is limited by the turbine emulator capability.

The converter was then tested with as high power as possible on both channels in the CC mode by the power supplies available. The total maximum input power reached about 1.45 kW (see Figure 5-46). The traces shows the output power is about 1.3 kW (the output current is about 50 A – Yellow trace, and output voltage is 26.7 V – Green trace), the input power for the PV channel is around 1 kW (49 V – the Light Blue trace, and 20 A – the Purple trace), and the TB input supplied the rest amount of input power. However, this test was only stable for around several minutes after the converter had jumped to these conditions. When the converter was run for a longer period, the heat sink elements used appeared to be insufficient. The rising temperature of the system leads to a gradual drop in the output voltage. As a result, the conversion quality is reduced, including efficiency and the amount of power. The temperature shut down protection was expected to activate, however it did not do so under these conditions. This was because the temperature of the system was not reaching the shutdown level. The temperature shut down blocks are integrated with the full-bridge controllers and the temperature thresholds are set at 160 ^{o}C [59]. The controllers are also not located nearby the hottest areas (the power switches, the gate drivers and the current sensing resistors).

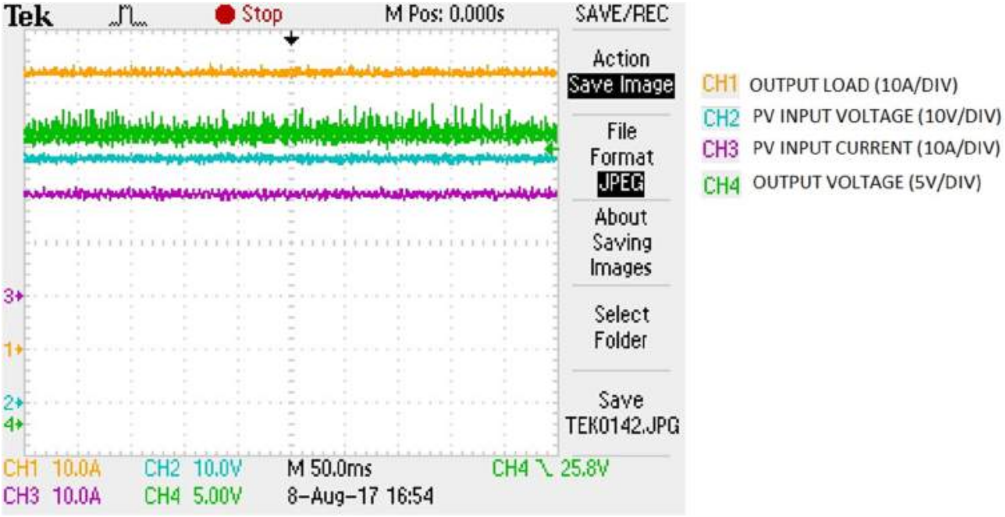

Figure 5-46. Waveforms of the converter when reaching the highest total power capability of the power supplies for both input sources

In short, the converter was tested at the maximum input power of 1 kW and 400 W on the PV and TB channel, respectively. The total of 1.4 kW input power was also tested in the case of both inputs sourcing power at the same time. The limitation of the turbine emulator and the power supply has constrained the chance to confirm the maximum power rating of the converter. With proper adjustments on the heat sink elements, there is confidence that the converter power capability can meet the design specifications.

CHAPTER 6 CONCLUSIONS AND FUTURE WORK

6.1. CONCLUSIONS

A low-cost MPPT multiple-input power converter for home applications in isolated areas has been proposed, designed, fabricated, and tested. Designed to be capable of delivery of up to 2 kW of total power from two input sources, the converter is constructed of a small size 4-layer PCB and components chosen for as low as possible cost. By combining analogue and digital control techniques into one novel interfacing circuit design, the converter is able to operate in three modes, including MPPT for all inputs sources, constant output voltage, and constant output current. The dynamic responses of the converter between input/output changes and between operation modes are appropriate, and there is no abnormal functioning during these transients. Being equipped with all the needed protection schemes, the converter can work alone or with a battery to store any excess energy for later use. Battery charging control, and battery discharging control with over charge and over discharge protection is integrated into this converter.

The block diagram of the converter was proposed first in terms of power conversion capacity, utilities, feasibility and cost. The non-isolated full-bridge topology is used for both input sources as this topology can convert a high amount of power with less stress on switching devices and the transformer. Instead of an advanced microcontroller, the integrated full-bridge controller is selected for high switching frequency, reliable operation, and fast response. The P&O algorithm of MPPT for both input channels is implemented by a small microcontroller, which allows for cost and programming effort reduction. A novel interfacing circuit is used for sharing the power flow between input sources to the output, and integrating different operation modes to the converter. The interface circuit allows three main control loops to work together in the converter without any disruption, which naturally activates the first-met-condition mode.

Main control loops and circuits of the converter were analysed mathematically. After that, details of the functional circuits were calculated and designed. Those circuits and main control loops were then simulated using TINA. The simulation results provided confidence that the circuit designs and overall converter would work as intended. The design of the transformer was confirmed by EPCOS Magnetic Design in terms of flux density and working temperature. Besides analogue circuitry, the configuration and implementation of the MPPT block was performed by using various tools from the microprocessor manufacturer. Once all the functions and specifications were completed, the full schematic of the converter was then moved to the physical design environment.

By using the Altium software package, the PCB of the converter was designed in 2-layer and 4-layer form. For cost and performance analysis, comparison between these versions was made for the final selection. The 4-layer PCB is selected for the converter as it has better characteristics than those of the 2-layer, such as lower cost, better heat dissipation, lower noise and potential of higher power conversion efficiency. The design of mounted heat sink elements also took place in this step.

The operations of the converter were tested in the laboratory environment with emulated power sources for the PV panel and turbine. With all scenarios of input variations and output conditions that might occur in real applications, the test results show the matching between converter's design and actual performance. The converter can work either with a single input or with both inputs simultaneously. The MPPT function is working properly and has a sufficiently fast response to the changes in both input channels. This mode is activated when the output power demand from both the output load and battery charging load is higher than the total available power from the inputs. When the total out power demand on the output is less than available source power, depending on battery charging state, the converter automatically switches to constant voltage output or constant current output. The transition between these modes occurs smoothly and quickly.

Among each operation mode, the response of the converter to the variation of input or output parameters was tested. The results show fast and accurate reactions of the converter. These include output load transient, input voltage transient, MPPT of varying input power, connection/disconnection of the battery, and turning on/off input sources. There are no significant additional stresses on components or jumping to abnormal operation stages. The protection schemes appear to work properly, such as UVLO, OVP, current limit, and battery over discharge protection.

With the wide range of input voltage for both inputs (from 16 V to 60 V) and the output voltage set to around 27 V, the converter can work in different conversion modes on each input channel, for example, step-up or step-down for both the PV and TB inputs. In the total of four combination modes, the power conversion efficiency ranges from about 85 % to 92 %. The highest measured efficiency is 95.3 % when the PV channel is in step-up mode and the TB channel in step-down mode when the total input power is around 400 W. The distribution of power flow from each channel to output is also shown in these tests. Depending on the input voltage of each source and the difference between them, the amount of power from an individual source will vary accordingly.

The converter can work with a lead-acid battery for storing energy while the output load on the dc-bus is lower than the available power from the combined input sources. Functioning with 3-stage battery charging for the best care of the battery, no external battery charger is required. The overall system can use the charged battery to compensate the output power demand while the input energy is not enough to supply the output load. Users are able to select different battery capacity settings, which in turn sets the maximum charging current for a battery up to the rating level of the switches used in the converter. This selection feature ensures safe and economical charging of the battery and makes the converter more flexible for use in isolated areas.

The operating temperature of the converter was observed and analysed. Although heat sinks and a forced air flow have been mounted onto the converter, the heat profiles show the temperature at some spots on the converter board are quite high. These could lead to the malfunction of components or the reduction of working hours. Some solutions have been proposed to address this issue, for example, addition of more heat sink material on those observed problem spots.

By choosing reasonable components in terms of cost comparison during the design, the components and standard material costs are just above $ 55 (excluding heat sink components). The PCB cost was about $ 3 per unit. For the final number of the converters cost, the addition of manufacture expense should be taken into account. However, with the total components/materials cost of around $ 60, the converter is indeed expected to be a low-cost product that is suitable for a single home application.

6.2. FUTURE WORK

Although the converter that has been designed and built appears to work properly in its application with all needed functions for an off-grid single home, there is some more work needed to be done before it can be commercialised.

Firstly, some adjustments need to be made to address the temperature issue. As such, increased space for observed hotspots and mounting proper heat sinks on them, and/or reduce the value of/eliminate the current sensing resistors.

Secondly, a proper turbine emulator needs to be established with at least of 1 kW power capacity for further testing on the MPPT and power capacity of the TB channel. The confirmation of total maximum power conversion of the converter should be also conducted, where both inputs are forced to run in MPPT mode and at the highest possible MPP of each source.

Thirdly, field testing with real input power sources should be made, along with different battery sizes to connect to the converter. This testing will ensure the converter can work under all expected operational ranges in isolated areas, where there is unlikely to be any technical support. The next step from here is to conduct more tests and carry out required adjustments for EMC.

Finally, some small adjustments to the design could be made for the flexible uses of the converter. For example, adding a 3-phase rectifier to the PV input channel and a dc power connector at the output of the rectifier in the TB channel could be made. Therefore, the converter could then be used for 2 PV sources, or 2 wind/micro hydro turbine sources, in addition to the combination of PV/Turbine sources.

REFERENCES

1. International Energy Agency, Organization for Economic Cooperation and Development (OECD) Staff and IEA, *World Energy Outlook 2016*. 2016. DOI: 10.1787/weo-2016-en.
2. V. G. García and M. M. Bartolomé, "Rural electrification systems based on renewable energy: The social dimensions of an innovative technology," *Technology in Society*, vol. 32, (4), pp. 303-311, 2010.
3. F. S. Javadi et al, "Global policy of rural electrification," *Renewable and Sustainable Energy Reviews*, vol. 19, pp. 402-416, 2013.
4. P. Mulder, J. Tembe, "Rural electrification in an imperfect world: a case study from Mozambique", *Energy Policy*, 36 (2008), pp. 2785-2794
5. B.J. Ruijven, J. Schers, D.P. Vuuren, "Model-based scenarios for rural electrification in developing countries", *Energy*, 38 (2012), pp. 386-397
6. R. Spalding-Fecher, "Health benefits of electrification in developing countries: a quantitative assessment in South Africa", *Energy for Sustainable Development*, 9 (2005), pp. 53-62
7. C.T. Gaunt, "Meeting electrification's social objectives in South Africa, and implications for developing countries", *Energy Policy*, 33 (2005), pp. 1309-1317
8. D.F. Barnes, S.R. Khandker, H.A. Samad, "Energy poverty in rural Bangladesh", Energy Policy", 39 (2011), pp. 894-904
9. A. Yadoo, H. Cruickshank, "The role for low carbon electrification technologies in poverty reduction and climate change strategies: a focus on renewable energy mini-grids with case studies in Nepal, Peru and Kenya", *Energy Policy*, 42 (2012), pp. 591-602
10. M. Fadaeenejad et al, "Assessment of hybrid renewable power sources for rural electrification in Malaysia," *Renewable and Sustainable Energy Reviews*, vol. 30, pp. 299-305, 2014.
11. JL Bernal-Agustín, R. Dufo-López, "Simulation and optimization of stand-alone hybrid renewable energy systems", *Renewable Sustainable Energy Rev*, 13 (2009), pp. 2111-2118
12. N. Phuangpornpitak, S. Kumar, "PV hybrid systems for rural electrification in Thailand", *Renewable and Sustainable Energy Reviews*, 11 (2007), pp. 1530-1543
13. M.G. Pereira, M.A.V. Freitas, N.F. da Silva, "Rural electrification and energy poverty: empirical evidences from Brazil", *Renewable and Sustainable Energy Reviews*, 14 (2010), pp. 1229-1240
14. Rieche, K., Corvarubias, A. and Martinot, E. (2000) "Expanding Electricity Access to Remote Areas: Off-Grid Rural Electrification in Developing Countries", *WorldPower 2000*, London, Isherwood Production, http://www.martinot.info/Reiche_et_al_WP2000.pdf
15. D. C. Huynh and M. W. Dunnigan, "Development and Comparison of an Improved Incremental Conductance Algorithm for Tracking the MPP of a Solar PV Panel," *IEEE Transactions on Sustainable Energy*, vol. 7, (4), pp. 1421-1429, 2016.
16. G. M. Masters, "Renewable and Efficient Electric Power Systems," 2004. pp. 385–604.

17. H. M. Kojabadi, L. Chang and T. Boutot, "Development of a novel wind turbine simulator for wind energy conversion systems using an inverter-controlled induction motor," *IEEE Transactions on Energy Conversion*, vol. 19, (3), pp. 547-552, 2004.
18. A. Date and A. Akbarzadeh, "Design and cost analysis of low head simple reaction hydro turbine for remote area power supply," *Renewable Energy*, vol. 34, (*2*), pp. 409-415, 2009.
19. “Switching regulator”, *Application note*, Texas Instruments, 2012
20. Chi Kin Taffy Wong, “A multiple-input single-output DC/DC converter for DC house project”, *ME thesis*, California Polytechnic State University, October 2011.
21. Lalit Kumar, S. J., “Multiple-input DC/DC converter topology for hybrid energy system, Department of Electrical Engineering”, *MANIT*, Bhopal, India, 2013
22. Chih-Lung Shen, Yong-Xian Ko, “Hybrid-input power supply with PFC (power factor corrector) and MPPT (maximum power point tracking) features for battery charging and HB-LED driving,” *Energy 72 (2014)* 501e509
23. Jianwu Zeng, Wei Qiao, Lian Qu, Yanping Jiao, “An Isolated Multiport DC–DC Converter for Simultaneous Power Management of Multiple Different Renewable Energy Sources*”, University of Nebraska-Lincoln*, 2014
24. Y. L. Juan and H. Y. Yang, “Hybrid Power System with A Two-Input Power Converter”, *WSEAS Transaction on Circuits and Systems*, May 2013
25. Shahab Poshtkouhi, Olivier Trescases, “Multi-input Single-inductor DC/DC Converter for MPPT in Parallel-Connected Photovoltaic Applications*”, 2011*
26. Chih-Lung Shen and Shih-Hsueh Yang, “Multi-Input Converter with MPPT Feature for Wind-PV Power Generation System”, *International Journal of Photo-energy*, Volume2013, Article ID 129254
27. S.Ramya, T.Manokaran, **“**A Novel Multi Input DC/DC Converter for Integrated Wind”, *PV Renewable Energy Generated System, International Journal of Engineering Research and Development*, Volume 4, Issue 4 (October 2012), PP. 62-68
28. Andres Lopez-Aranguren Oliver, “MPPT Wind and Photovoltaic using multiple inputs DC/DC converter”, *ME Thesis, Aalborg University*, June 1, 2014
29. O. Erdinc and M. Uzunoglu, "Optimum design of hybrid renewable energy systems: Overview of different approaches," *Renewable and Sustainable Energy Reviews, vol. 16*, (3), pp. 1412-1425, 2012.
30. J. P. Barton and D. G. Infield, "Energy storage and its use with intermittent renewable energy," *IEEE Transactions on Energy Conversion, vol. 19*, (2), pp. 441-448, 2004.
31. E. Fertig et al, "Optimal investment timing and capacity choice for pumped hydropower storage," *Energy Systems, vol. 5*, (2), pp. 285-306, 2014;2013.
32. E. Jannelli et al, "A small-scale CAES (compressed air energy storage) system for stand-alone renewable energy power plant for a radio base station: A sizing-design methodology," *Energy, vol. 78*, pp. 313-322, 2014.
33. N. C. Nair and N. Garimella, "Battery energy storage systems: Assessment for small-scale renewable energy integration," Energy & Buildings, vol. 42, (11), pp. 2124-2130, 2010.

34. V. Kokaew, S. M. Sharkh and M. Moshrefi-Torbati, "Maximum Power Point Tracking of a Small-Scale Compressed Air Energy Storage System," *IEEE Transactions on Industrial Electronics, vol. 63,* (2), pp. 985-994, 2016.
35. R. D. L. Vollaro et al, "Energy and Thermodynamical Study of a Small Innovative Compressed Air Energy Storage System (micro-CAES)," Energy Procedia, vol. 82, pp. 645-651, 2015.
36. D. Villela et al, "Compressed-air energy storage systems for stand-alone off-grid photovoltaic modules," *in 2010*, . DOI: 10.1109/PVSC.2010.5614596.
37. P. Kubalik et al, "Suitable energy storage in off-grid systems," 2014, DOI: 10.1109/EEEIC.2014.6835891.
38. H. Abu-Rub, Power Electronics for Renewable Energy Systems, Transportation and Industrial Applications. (1st ed.) 2014.
39. G. N. Prodromidis and F. A. Coutelieris, "Innovative Energy Storage for Off-Grid RES-Based Power Systems: Integration of Flywheels with Hydrogen Utilization in Fuel Cells," *Journal of Energy Engineering*, vol. 140, (4), pp. 4014006, 2014.
40. M. Budt et al, "A review on compressed air energy storage: Basic principles, past milestones and recent developments," *Applied Energy, vol. 170*, pp. 250, 2016.
41. L. Wuidart, "Topologies for switched mode power supply", *Application Note AN513/0393*, St Microelectronics, 1999
42. BoB Bell and Ajay Hari, "Topology Key to Power Density in Isolated DC/DC Converters", *Power Electronics Technology*, February 2011
43. J. Liu et al, "A Digital Current Control of Quasi-Z-Source Inverter With Battery," *IEEE Transactions on Industrial Informatics*, vol. 9, (2), pp. 928-937, 2013.
44. P. Fang Zheng, "Z-source inverter," *IEEE Trans. Ind. Appl*., vol. 39, no. 2, pp. 504–510, Mar./Apr. 2003.
45. V. P.Galigekere andM. K. Kazimierczuk, "Analysis of PWMZ-source DC/DC converter in ccm for steady state," *IEEE Trans. Circuits Syst. I, Reg. Papers*, vol. 59, no. 4, pp. 854–863, Apr. 2012.
46. D. Cao and F. Z. Peng, "A family of Z-source and quasi-Z-source DC/DC converters," *in Proc. IEEE Appl. Power Electron. Conf.*, Feb. 2009, pp. 1097–1101.
47. D. Vinnikov and I. Roasto, "Quasi-Z-source-based isolated DC/DC converters for distributed power generation*," IEEE Trans. Ind. Electron*., vol. 58, no. 1, pp. 192–201, Jan. 2011.
48. M. K. Nguyen, Q. D. Phan, V. N. Nguyen, Y. C. Lim, and J. K. Park, "Trans-Z-source-based isolated DC/DC converters," *in Proc. IEEE Int. Symp. Ind. Electron*., May 2013, pp. 1–6.
49. H. Lee, H.-G. Kim, and H. Cha, "Parallel operation of trans-Z-source network full bridge DC/DC converter for wide input voltage range," *Proc. IEEE Int. Power Electron. Energy Motion Control Conf.*, Jun. 2012, pp. 1707–1712.
50. I. Roasto, D. Vinnikov, J. Zakis, and O. Husev, "New shoot-through control methods for qZSI-based DC/DC converters," *IEEE Trans. Ind. Informat.,* vol. 9, no. 2, pp. 640–647, May 2013.
51. Y. P. Siwakoti and G. Town, "Improved modulation technique for voltage fed quasi-Z-source DC/DC converters," *in Proc. IEEE Appl. Power Electron. Conf. Expo*., Mar. 2014, pp. 1973–1978.

52. B. Zhao et al., “Switched Z-source isolated bidirectional DC/DC converter and its phase-shifting shoot-through bivariate coordinated control strategy,” *IEEE Trans. Ind. Electron.*, vol. 59, no. 12, pp. 4657–4670, Dec. 2012.
53. D. Vinnikov et al., “CCM and DCM operation analysis of cascaded quasi-Z-source inverter,” *IEEE Int. Symp. Ind. Electron. (ISIE)*, 2011, pp. 159–164.
54. Z. Miao et al., “Switched inductor Z-source inverter,” *IEEE Trans. Power Electron.*, vol. 25, no. 8, pp. 2150–2158, Aug. 2010.
55. Q. Wei et al., “Trans-Z-source inverters,” *IEEE Trans. Power Electron.*, vol. 26, no. 12, pp. 3453–3463, Dec. 2011.
56. M. Shen, A. Joseph, J. Wang, F.Z. Peng, D.J. Adams, “Comparison of Traditional Inverters and Z-Source Inverter for Fuel Cell Vehicles”, *IEEE Transactions on Power Electronics*, 22(4), pp. 1453–1463, July 2007.
57. Shamim Choudhury, “Digitally Controlled HV Solar MPPT DC/DC Converter Using C2000™ Piccolo™ Microcontroller”, *Application Report*, Texas Instruments, May 2013
58. Abu-Qahouq, Jaber A.; Wen, Yangyang; Yao, Liangbin; Shoubaki, Ehab; Batarseh, Issa; Potter, Geof, “Digital controller for an isolated half-bridge DC/DC converter”, *Applied Power Electronics Conference and Exposition*, 2005. APEC 2005.
59. “LM5045 Datasheet”, *Texas Instruments*
60. J. Surya Kumari, Ch. Sai Babu, A. Kamalakar Babu, “Design and Analysis of P&O and IP&O MPPT Techniques for Photovoltaic System”, *International Journal of Modern Engineering Research (IJMER)*, Vol.2, Issue.4, July-Aug. 2012 pp-2174-2180
61. C. Hua, C. Shen, “Comparative study of Peak Power Tracking Techniques for Solar Storage Systems”, *IEEE Applied Power Electronics Conference and Exposition Proceedings*, Vol 2, pp. 679-683, Feb. 1998.
62. D. P. Hohm, M. E. Ropp, “Comparative Study of Maximum Power Point Tracking Algorithms Using an Experimental, Programmable, Maximum Power Point Tracking Test Bed”, *Photovoltaic Specialists Conference*, 2000, pp. 1699-1702
63. A. Arti, SP. Umayal, “MPPT Based Photovoltaic High Intensity Discharge Street Lighting System Using Fuzzy Logic Controller”, *International Journal of Emerging Technology and Advanced Engineering*, Volume 3, Issue 5, May 2013
64. Il-Song Kim and Myung-Joong You, “Single-loop maximum power point tracker with fast settling time”, *The 30th Annual Conference of the IEEE Industrial Electronics Society*, Busan, Korea, November 2 - 6, 2004
65. Trishan Esram, Jonathan W. Kimball, Philip T. Krein, Patrick L. Chapman, and Pallab Midya, “Dynamic Maximum Power Point Tracking of Photovoltaic Arrays Using Ripple Correlation Control”, *IEEE Transactions on Power Electronics*, Vol. 21, No. 5, SEPTEMBER 2006
66. Xiaoguo Liang, Gnanavel Jayakanthan, Meng Wang, “Design Considerations for Narrow Vdc based Power Delivery Architecture in Mobile Computing System”, *Proc. Applied Power Electronics Conference and Exposition (APEC),* Palm Springs, CA, 2010, pp. 794–800

67. Wang Li, Michael Day, “Solar charging solution provides narrow voltage DC/DC system bus for multicell battery applications”, *Analog Applications Journal*, Texas Instruments Incorporated, 2011
68. K 8012, “Lead Acid Battery Charger”, *User's manual*, Velleman, Belgium
69. AND8490/D, “Theory and Applications of the NCP1294, Switching Controller, and Associated Circuits for Lead Acid Battery Charging from a Solar Panel with Maximum Peak Power Tracking (MPPT)”, *Application Note*, ON Semiconductor, September, 2015 − Rev. 2
70. Henry A. Catherino, Fred F. Feres, Francisco Trinidad, “Sulfation in lead–acid batteries”, *Journal of Power Sources 129* (2004) 113–120
71. Carmen Parisi, “Multiphase Buck Design From Start to Finish (Part 1)”, *Application Report*, Texas Instruments, SLVA882, April 2017.
72. Christian Andersson, "Design of a 2.5kW DC/DC Fullbridge Converter", *Master of Science Thesis, CHALMERS UNIVERSITY OF TECHNOLOGY*, Göteborg, Sweden, 2011
73. Jaya Kaviya.V, Manjula Devi .K, "Full-Bridge phase shifted on-chip DC-DC converter for Point-of-load voltage regulation", *International Journal of Advanced Research in Electronics and Communication Engineering (IJARECE)*, Volume 3, Issue 3, March 2014
74. Pressman, A.I. 1998, “Switching power supply design”, *2nd edn, McGraw-Hill*, New York.
75. Maniktala Sanjaya, “Switching power supplies A to Z”, *Elsevier/Newnes*, 2006, pp. 297-301
76. Christophe Vaucourt, "Choosing Inductors and Capacitors for DC/DC Converters", *Application Report, Texas Instruments*, SLVA157 – February 2004
77. F. Martinez, L. Herrero and S. de Pablo, "Open loop wind turbine emulator," *Renewable Energy*, vol. 63, pp. 212-221, 2014.
78. M. Shen, A. Joseph, J.Wang, F. Z. Peng, and D. J. Adams, “Comparison of traditional inverters and Z-source inverter,” *in Proc. IEEE Power Electron. Spec. Conf.,* Jun. 2005, pp. 1692–1698.
79. B. Farhangi and S. Farhangi, “Comparison of Z-source and boostbuck inverter topologies as a single phase transformer-less photovoltaic grid-connected power conditioner,” *in Proc. IEEE Power Electron. Spec. Conf.*, Jun. 2006, pp. 1–6.
80. X. P. Fang, J. M. Cui, J. Liu, and M. Y. Cao, “Detail research on the traditional inverter and Z-source inverter,” *in Proc. Int. Conf. Appl. Supercond. Electromagn. Devices*, Dec. 2011, pp. 318–321.
81. J. Li, J. Liu, and L. Zeng, “Comparison of Z-source inverter and traditional two-stage boost-buck inverter in grid-tied renewable energy generation,” *in Proc. IEEE 6th Int. Power Electron. Motion Control Conf.,* May 2009, pp. 1493–1497.
82. W. T. Franke, M. Mohr, and F. W. Fuchs, “Comparison of a Z-source inverter and a voltage-source inverter linked with a DC/DC-boost-converter for wind turbines concerning their efficiency and installed semiconductor power,” *in Proc. IEEE Power Electron. Spec. Conf.*, Jun. 2008, pp. 1814– 1820.
83. C. R. Swartz, Vicor, “High-Performance ZVS Buck Regulator Removes Barriers to Increased Power Throughput in Wide Input Range Point-Of-Load Applications”, August 2012.

84. T.-C. Yu, C.-C. Liu, Y.-B. Lin, C.-H. Chen & Y.-C. Liou, “A study of photovoltaic systems with a variable step size P&O MPPT algorithm”, *Proceedings of the 4th International Conference on Green Building*, Materials and Civil Engineering (GBMCE 2014)
85. J Riche, “High-temperature power supply design”
86. Yao-Ming Chen, Y.-C. L. and Lin, S.-H, “Double-input PWM DC/DC converter for high/low voltage sources”, *Power Electronics Applied Research Laboratory Department of Electrical Engineering*, National Chung Cheng University, 2013

APPENDICES

Appendix A. SPICE model of LM5045

```
.SUBCKT LM5045 UVLO OVP RAMP CS SLOPE COMP REF RT RD1 RD2 RES SS SSSR SSOFF HS2
HO2 BST2 SR2 LO2 VCC LO1 SR1 BST1 HO1 HS1 VIN
Ccomp1          COMP 0 1p IC=0
Ccounter1       BUFFER1 0 10n IC=0
Ccounter2       BUFFER2 0 10n IC=0
Ccounter3       HICCUPCOMPLETE 0 400p IC=0
Ccounter4       COUNTER9 0 4p IC=0
Ccounter5       COUNTER10 0 4p IC=0
Ccs1       CSINT 0 4p IC=0
Ccs2       ILIM 0 100p IC=0
Cdd1        DELAYDRVA 0 40p IC=0
Cdd2        DELAYDRVB 0 40p IC=0
Cdr10        LO1 0 4p IC=0
Cdr11        SR1 0 4p IC=0
Cdr12        SR2 0 4p IC=0
Cdr13        DR8 0 4p IC=0
Cdr14        HO2 HS2 4p IC=0
Cdr15        LO2 0 4p IC=0
Cdr16        DR7 0 4p IC=0
Cdr5       DR5 0 4p IC=0
Cdr6       DR6 0 4p IC=0
Cdr7       DR9 0 4p IC=0
Cdr8       DR10 0 4p IC=0
Cdr9       HO1 HS1 4p IC=0
Cisr1       ISR1 0 4p IC=0
Cisr2       NSRSIGNAL 0 4p IC=0
Cisr3       ISR 0 24.5p IC=0
Cleb1        LEB1 0 4p IC=0
Cleb2        LEB6 0 4p IC=0
Cleb3        LEB8 0 8p IC=0
Cmsk1         MSK2 0 4p IC=0
Cmsk2         MSK3 0 4p IC=0
Cosc1        CLK 0 5p IC=5
Cosc2        OSC2 0 5p IC=5
Cov1        OVPOUT 0 4p IC=0
Cpwm1         PWM2 0 4p IC=0
Cpwm2         PWM4 0 4p IC=0
Cram1         RAM2LEB 0 4p IC=0
Cram2         RAM5 0 4p IC=0
Cres2        RES2 0 400p IC=0
Cres3        AT2V2 0 40p IC=5
Cres4        AT4V2 0 40p IC=0
Cres5        AT0P1V2 0 40p IC=0
```

```
Cres6        HICCUPSTART 0 40p IC=0
Cres7        RES10 0 20p IC=0
Cres8        RES9 0 20p IC=0
Cres9        RES4 0 20p IC=0
Cslope1        IOUTSLOPE 0 5p IC=0
Css10        SS6 0 4p IC=0
Css11        SS5 0 4p IC=0
Css5        SS 0 4p IC=0
Css7        SS2 0 4p IC=0
Css9        RSTOUT 0 4p IC=0
Csssr1        SSSR 0 4p IC=0
Csssr2        SSSR2 0 4p IC=0
Csssr3        SSSR4 0 4p IC=0
Csssr4        SSSR5 0 4p IC=0
Csssssr1        SOFTSTOPSSSR 0 4p IC=0
Cstate1        STATER 0 4p IC=0
Cstate2        STATES 0 4p IC=0
Ctc1        TC2 0 4p IC=0
Ctc10        TC24 0 4p IC=0
Ctc11        TC27 0 4p IC=0
Ctc12        TC30 0 4p IC=0
Ctc2        TC4 0 4p IC=0
Ctc3        TC7 0 4p IC=0
Ctc4        TC9 0 4p IC=0
Ctc5        TC12 0 4p IC=0
Ctc6        TC14 0 4p IC=0
Ctc7        TC17 0 4p IC=0
Ctc8        TC19 0 4p IC=0
Ctc9        TC22 0 4p IC=0
Cuvc3        UVC2 0 4p IC=0
Cuvc4        VCCLOW 0 4p IC=0
Cuvi1        SD 0 4p IC=0
Cuvi2        UVLO_LT2 0 4p IC=0
Cuvi3        RD2 0 4p IC=0
Cuvi4        RD1 0 4p IC=0
Cuvr1        UVR2 0 4p IC=0
Cuvr2        VREFLOW 0 4p IC=5
Cuvr3        UVR6 0 8p IC=0
Cvcc1        VCC3 0 3p IC=0
Cvcc2        VCC4 0 4p IC=0
Cvcc3        VCC5 0 4p IC=0
Cvcc4        VCC6 0 4p IC=0
Cvcc5        VCC7 0 4p IC=0
Cvccboost        VCCBOOST 0 4p IC=0
Cvccboost_vcc        BOOST1R8 0 4p IC=0
Cvccint1        0 VCCINT 10p IC=0
Cvref1        VREF3 0 3p IC=0
Cvref2        REF 0 4p IC=0
```

```
Dvcc1        VCCD1 VIN DNOM
Dvcc2        VCC VCCD1 DNOM
Dvref1        REF VCC DNOM
Ecomp1        COMP4 0 VALUE { V(SS) }
Ecounter1        COUNTER8 0 VALUE { if((V(at2V1)>(V(at2V2)+0.1)) & V(VREFuv)<=2.5 &
V(VCCuv)<=2.5, 5, 0) }
Ecounter2        COUNTER11 0 VALUE { if((V(at4V1)>(V(at4V2)+0.1)) & V(VREFuv)<=2.5 &
V(VCCuv)<=2.5, 5, 0) }
Ecounter3        COUNTER2 0 COUNTER1 0 1
Ecounter4        COUNTER5 0 COUNTER4 0 1
Edff1        DFF2 0 VALUE { if(V(NCLK)>2.5,V(NPH),0) }
Edff2        DFF3 0 VALUE { if(V(NCLK)>2.5,V(PH),0) }
Edff3        DFF6 0 VALUE { if(V(CLK)>2.5,V(DFF4),0) }
Edff4        DFF7 0 VALUE { if(V(CLK)>2.5,V(DFF5),0) }
Edrv10        SR2SIG 0 VALUE { if(V(SR2IN)>2.5 & V(NSRSIGNAL)<=2.5 & V(VCClow)<=2.5 &
V(RSTout)<=2.5,5,0) }
Edrv5        DRVHO1SIG 0 VALUE { if(V(HO1IN)>2.5 & V(VCCLOW)<=2.5 & V(RSTout)<=2.5 &
(V(BST1)-V(HS1))>4.7,5,0) }
Edrv6        DRVLO1SIG 0 VALUE { if(V(LO1IN)>2.5 & V(VCCLOW)<=2.5 & V(RSTout)<=2.5,5,0) }
Edrv7        DRVHO2SIG 0 VALUE { if(V(HO2IN)>2.5 & V(VCCLOW)<=2.5 & V(RSTout)<=2.5 &
(V(BST2)-V(HS2))>4.7,5,0) }
Edrv8        DRVLO2SIG 0 VALUE { if(V(LO2IN)>2.5 & V(VCCLOW)<=2.5 & V(RSTout)<=2.5,5,0) }
Edrv9        SR1SIG 0 VALUE { if(V(SR1IN)>2.5 & V(NSRSIGNAL)<=2.5 & V(VCClow)<=2.5 &
V(RSTout)<=2.5,5,0) }
Eisr1        ISR3 0 VALUE { if(V(ISR)>V(SSSR),5,0) }
Eisr2        ISR2 0 VALUE { if(V(CLK)>2.5 | V(state) <2.5,5,0) }
Eleb1        LEB2 0 VALUE { if(V(LEB3)>2.5 | V(LEB4)>2.5,5,0)  }
Eleb2        LEB5 0 LEB6 0 1
Emsk1        MSK4 0 VALUE { if(V(CLK)<=2.5 & V(PWM)<=2.5,5,0) }
Emsk2        MSK5 0 VALUE { if(V(PWM)>2.5 & V(CLK)<=2.5,5,0) }
Eosc1        OSC1 0 VALUE { if(V(OSC2)>cos(2*3.14*50E-9/(2/(6.25E9*I(VRT))+110E-9)),5,0) }
Eosc2        OSC3 0 VALUE { if(V(VREFuv)<=2.5 & V(VCCuv)<=2.5 &
V(FAULT)<=2.5,sin(2*3.141592*TIME*I(VRT)/100E-12/2),0) }
Eosc3        NCLK 0 VALUE { {5-V(CLK)} }
Eov1        OV1 0 VALUE { if(V(OVP)>1.25,5,0) }
Epwm1        PWM1 0 VALUE { if(V(RSTOUT)>2.5 | V(CLK)>0.5, 5, 0) }
Epwm2        PWM3 0 VALUE { if((V(ILIM)>2.5 | V(comp2PWM)<=V(RAMPint)) &
V(comp2pwm)>0, 5, 0) }
Eram        RAMPINT 0 RAMP 0 1
Eram1        RAM3 0 VALUE { if(V(PWM)>4.5 | V(CLK)>2.5 | V(RSTout)>2.5, 5, 0) }
Eram2        RAM6 0 VALUE { if(V(VCCUV)>2.5 | V(VREFUV)>2.5 | V(COMPi)<=1, 5, 0) }
Eres1        RES3 0 VALUE { if(V(CLK)>(V(osc1)+0.1), 5, 0) }
Eres2        RES7 0 VALUE { if((V(CLK)< (V(osc1)-0.1)) & V(RES6)<=2.5, 5, 0) }
Eres3        RES8 0 VALUE { if((V(CLK)< (V(osc1)-0.1)) & V(RES6)>2.5, 5, 0) }
Eres4        AT4V1 0 VALUE { if(V(RES)>4, 5, 0) }
Eres5        AT2V1 0 VALUE { if(V(RES)<=2 | V(nFAULT)>2.5, 5, 0) }
Eres6        AT0P1V1 0 VALUE { if(V(RES)<0.1, 5, 0) }
Eres7        AT1V1 0 VALUE { if(V(RES)>1, 5, 0) }
```

```
Eres8        COUNTER7 0 VALUE { if(V(BUFFER2)>15.5 & V(at2V1)<=(V(at2V2)+0.1), 5, 0) }
Eres9        RESDISCHARGE 0 VALUE { if(V(VCCuv)>2.5 | V(VREFuv)>2.5 | V(HiccupComplete)>2.5,
10, 0) }
Ess1        SSDISCHARGE 0 VALUE { if(V(VCCuv)>2.5 | V(VREFuv)>2.5 | V(SS4)<=2.5, 5, 0) }
Ess2        SS9 0 VALUE { if((V(SSSR)<1 & V(SoftStopSSSR)>2.5) | ((V(SoftStopSSSR)>2.5 &
V(SSoff)>2.8) | V(VCCuv)>2.5 |
+V(VREFuv)>2.5 | V(OVPout)>2.5), 5, 0) }
Ess3        SS8 0 VALUE { if(V(SS)<=0.2, 5, 0) }
Ess4        RSTOUT1 0 VALUE { if(V(SS6)>2.5 | V(SS4)<=2.5, 5, 0) }
Esssr1        SSSR7 0 VALUE { if(V(STATE)<=2.5, 5, 0) }
Esssr2        SSSR8 0 VALUE { if(V(SSSR)<=0.2, 5, 0) }
Essssr1        SSSSSR1 0 VALUE { if(V(FAULT)>2.5 | V(UVLO_lt2)>2.5, 5, 0) }
Estate1        STATER1 0 VALUE { if(V(SS5)>2.5 |V(SS)<=0.2, 5, 0) }
Estate2        STATES1 0 VALUE { if(V(VCCuv)<=2.5 & V(VREFuv)<=2.5 & V(OVPout)<=2.5 &
(V(SSoff)<=2.75 |
+V(SoftStopSSSR)<=2.5) & (V(SoftStopSSSR)<=2.5 & V(SS)>2 & V(COMPi)>1.0 ), 5, 0) }
Etc10        TC23 0 VALUE { if(V(comp2pwm)>0 & (V(PH)>2.5 | V(MskPWM)>2.5) &
(V(delayDRVB)>0.5 & V(delayDRVB)<=2.5),5,0) }
Etc11        TC26 0 VALUE { if(V(RSTout)>2.5 | (V(PH)>2.5 & V(MskPWM)<=2.5),5,0) }
Etc12        TC28 0 VALUE { if(V(comp2pwm)>0 & (V(PH)<=2.5 | V(MskPWM)>2.5) &
(V(delayDRVA)>0.5 & V(delayDRVA)<=2.5),5,0) }
Etc2        TC3 0 VALUE { if(V(comp2pwm)>0 & V(PH)>2.5 & V(MskPWM)<=2.5 &
(V(delayDRVA)>2.5& V(delayDRVA)<=4.5),5,0) }
Etc4        TC8 0 VALUE { if(V(comp2pwm)>0 & V(PH)<=2.5 & V(MskPWM)<=2.5 &
(V(delayDRVB)>2.5& V(delayDRVB)<=4.5),5,0) }
Etc9        TC21 0 VALUE { if(V(RSTout)>2.5 | (V(PH)<=2.5 & V(MskPWM)<=2.5),5,0) }
Euvc1        UVC3 0 VALUE { if(V(VCC)>V(VCCREGPT),5,0) }
Euvc2        UVC5 0 VALUE { if(V(VCC)<6.3,5,0) }
Euvi1        UVI1 0 VALUE { if(V(UVLO)<0.4,5,0) }
Euvi2        UVI2 0 VALUE { if(V(UVLO)>1.25,0,5) }
Euvr1        UVR3 0 VALUE { if(V(UVR6)>V(REFREGPT),5,0) }
Euvr2        UVR5 0 VALUE { if(V(UVR6)<4.3,5,0) }
Ev15        V5V 0 VALUE { if(V(VIN)>13,5,0) }
Evcc_boost        VCC8 0 VALUE { IF(V(VCCBOOST)>2.5, 1.8, 0) }
Evcc1        VCC1 BOOST1R8 TABLE { V(VIN, 0) } ( (0,0)(2.8,0)(10.5,7.8) )
Evcc2        VCC2 0 VALUE { IF(V(SD)>2.5, 0, V(VCC1)) }
Evccboost        BOOST1 0 VALUE { if(V(STATE)<=2.5 | V(SSSR)<1 ,5,0) }
Evref1        VREF1 0 TABLE { V(VCC) } ( (0,0) (2, 0) (3.2,3) (5.2,5) )
Evref2        VREF2 0 VALUE { IF( V(SD)>2.5, 0, V(VREF1)) }
Evrt1        VRT1 0 TABLE { V(REF,0) } ( (0,0) (2,2) )
Gdt1        0 RD1 TABLE { V(V5V, 0) } ( (0,1E-6)(5,40E-6) )
Gdt2        0 RD2 TABLE { V(V5V, 0) } ( (0,1E-6)(5,40E-6) )
Ggateloss        VIN 0 VALUE { I(VVCC) }
Gisr1        0 ISR VALUE { if(V(ISR1)>2.5,1,0) }
Givcc1        VCC7 0 TABLE { V(VCC) } ( (0,0) (10,0.0046)  )
Govhys1        0 OVP VALUE { if(V(OVPOUT)>2.5, 20E-6, 0) }
Gres1        0 RES VALUE {if(V(FAULT)>2.5,if(V(p10u_hiccup)>4.5,10E-6,if(V(n5u_hiccup)>4.5,-5E-
6,0)),if(V(p30u)>4.5,
```

```
+30E-6,if(V(n5u)>4.5,-5E-6,0))) }
Gslope1        0 IOUTSLOPE1 VALUE { if(V(CLK)<=2.5 & V(VREFuv)<=2.5 & V(VCCuv)<=2.5,
I(VRT)/20,0) }
Gslope2        0 SLOPE VALUE { if(V(VREFuv)<=2.5 & V(VCCuv)<=2.5, V(IOUTSLOPE)/20000,0) }
Gss1        0 SS VALUE { if(V(VREFuv)<=2.5,20E-6,0) }
Gsssr1        0 SSSR VALUE { if(V(VREFuv)<=2.5,20E-6,0) }
Gsssr2        SSSR 0 VALUE {if(V(SoftStopSSSR)>2.5,if(V(state)>2.5,65E-6,if(V(FAULT)>2.5,125E-
6,0)),0) }
Guvihys1        UVLO 0 VALUE { if(V(UVLO_LT2)>2.5, 20E-6, 0) }
Gvcc1        0 VCC4 TABLE { V(VCC3, VCC4) } ( (-1.4, -1)(0,0)(0.3,0.052) )
Gvref1        VCC REF TABLE { V(VREF3, REF) } ( (-0.7,-1)(0,0)(0.15,0.015) )
Q_Qcomp1        COMP COMP COMP2 NOMNPN
Qcomp2        COMPI COMP COMP3 NOMNPN
Rcomp1        REF COMPI  5k
Rcomp2        COMP2 0  200
Rcomp3        COMP3 0  200
Rcomp4        COMP5 COMP2PWM  24k
Rcomp5        COMP2PWM 0  24k
Rcounter1        HICCUPCOMPLETE COUNTER7  500
Rcounter2        BUFFER2 COUNTER3  1
Rcounter3        BUFFER1 COUNTER6  1
Rcounter4        COUNTER9 HICCUPCOMPLETE  500
Rcounter5        COUNTER10 HICCUPCOMPLETE  500
Rcounter6        COUNTER6 0  10Meg
Rcounter7        BUFFER2 0  10Meg
Rcs1        CS2 CS  18
Rcs2        CS CSINT  2k
Rcs3        CS1 ILIM  500
Rdr10        DRVHO2SIG DR7  500
Rdr5        DRVHO1SIG DR5  500
Rdr6        DRVLO1SIG DR6  500
Rdr7        SR1SIG DR9  500
Rdr8        SR2SIG DR10  500
Rdr9        DRVLO2SIG DR8  500
Rdt1dummy        RD1 0  10E6
Rdt2dummy        RD2 0  10E6
RdumRT        RT 0  10E6
RdumSlope1        IOUTSLOPE 0  10E6
RdumSlope2        SLOPE 0  10E6
Risr1        ISR1 ISR2  500
Risr2        ISR3 NSRSIGNAL  500
Rleb1        LEB1 LEB2  500
Rleb2        LEB3 0  1
Rleb3        LEB6 LEB4  500
Rleb4        LEB8 LEB9  500
Rmsk1        MSK2 MSK4  500
Rmsk2        MSK3 MSK5  500
Rosc1        CLK OSC1  500
```

```
Rosc2        OSC2 OSC3  500
Rov1        OVPOUT OV1  2500k
Rovdummy        0 OVP  10Meg
Rpwm1        PWM2 PWM1  1000
Rpwm2        PWM4 PWM3  500
Rram1        RAM1 RAMP  5.5
Rram2        RAM2LEB RAM3  500
Rram3        RAM4 RAMP  1k
Rram4        RAM5 RAM6  500
Rres1        RES1 RES  30
Rres2        RES2 RESDISCHARGE  500
Rres3        AT4V1 AT4V2  500
Rres4        AT2V1 AT2V2  500
Rres5        AT0P1V1 AT0P1V2  500
Rres6        AT1V1 HICCUPSTART  500
Rres7        RES8 RES10  500
Rres8        RES7 RES9  500
Rres9        RES3 RES4  500
Rss10        SS6 SS8  500
Rss11        SS5 SS9  500
Rss12 SSOFF 0 200E3
Rss7        SS1 SS  200
Rss8        SS2 SSDISCHARGE  500
Rss9        RSTOUT RSTOUT1  500
Rsssr1        SSSR1 SSSR  200
Rsssr2        SSSR2 SSSR3  500
Rsssr3        SSSR4 SSSR7  500
Rsssr4        SSSR5 SSSR8  500
Rsssssr1        SOFTSTOPSSSR SSSSSR1  500
Rstate1        STATER STATER1  500
Rstate2        STATES STATES1  500
Rtc1        TC1 TC2  500
Rtc10        TC23 TC24  500
Rtc11        TC26 TC27  500
Rtc12        TC28 TC30  500
Rtc2        TC3 TC4  500
Rtc3        TC6 TC7  500
Rtc4        TC8 TC9  500
Rtc5        TC11 TC12  500
Rtc6        TC13 TC14  500
Rtc7        TC16 TC17  500
Rtc8        TC18 TC19  500
Rtc9        TC21 TC22  500
Ruvc3        UVC2 UVC3  1.5k
Ruvc4        VCCLOW UVC5  1.5k
Ruvi1        SD UVI1  500
Ruvi2        UVLO_LT2 UVI2  2500k
Ruvidummy        0 UVLO  10Meg
```

```
Ruvr1        UVR2 UVR3  500
Ruvr2        VREFLOW UVR5  500
Ruvr3        UVR6 REF  500
Rvcc1        VCC2 VCC3  1
Rvcc2        VCCREGPT VCC3  200
Rvcc3        0 VCC4  5k
Rvcc4        VCC7 VCC  1
Rvcc5        0 VCCREGPT  1.8k
Rvccboost        BOOST1 VCCBOOST  500
Rvccboost_vcc        VCC8 BOOST1R8  500
Rvccint1        VCC6 VCCINT  100m
Rvccint2        VCCINT VCC  10m
Rvindummy1        VIN 0  333k
Rvref1        VREF2 VREF3  1
Rvref2        REFREGPT VREF3  500
Rvref3        0 REF  5k
Rvref4        0 REFREGPT  4.5k
Tleb        LEB3 0 LEB5 0 Z0=1 TD=40n
Xdff1        DFF2 DFF3 DFF4 DFF5 rsff5k
Xdff2        DFF6 DFF7 PH NPH rsff5k
Xleb1        RAM2LEB LEB8 leb7 LEB4 rsff5k
Xmsk1        MSK2 MSK3 MskPWM msk1 rsff5k
Xpwm1        PWM2 PWM4 PWM pwm5 rsff5k
Xres1        RES4 ILIM RES6 res5 rsff5k
Xres2        RES9 RES10 p30u n5u rsff5k
Xres3        AT4V2 AT2V2 p10u_hiccup n5u_hiccup rsff5k
Xres4        AT0P1V2 HICCUPSTART FAULT nFAULT rsff5k
Xss1        SS6 SS5 ss7 SS4 rsff5k
Xsssr1        SSSR4 SSSR5 sssr6 SSSR3 rsff5k
Xstate        STATER STATES STATE statenq rsff5k
Xtc1        TC2 TC4 HO1IN tc5 rsff5k
Xtc2        TC7 TC9 LO1IN tc10 rsff5k
Xtc3        TC12 TC14 HO2IN tc15 rsff5k
Xtc4        TC17 TC19 LO2IN tc20 rsff5k
Xtc5        TC22 TC24 SR1IN tc25 rsff5k
Xtc6        TC27 TC30 SR2IN tc29 rsff5k
Xuvc1        UVC2 VCCLOW VCCUV uvc1 rsff5k
Xuvr1        UVR2 VREFLOW VREFUV uvr1 rsff5k
V1        V5V_0P2 V5V 0.2
V1V5        COMPI COMP5 1
Vcounter1        COUNTER1 BUFFER1 1
Vcounter2        COUNTER4 BUFFER2 1
VRT        VRT1 RT 0
VVCC        VCC4 VCC5 0

*S5K
Scs1    CS2 0 LEB1 0 S5K
Sram1    RAM1 0 RAM2LEB 0 S5K
```

```
Sram2    RAM4 0 RAM5 0 S5K
Sres1    RES1 0 RES2 0 S5K
Sslope1    IOUTSLOPE 0 CLK 0 S5K
Sss1    SS1 0 SS2 0 S5K
Ssssr1    SSSR1 0 SSSR2 0 S5K

*SCLAMP
Scompdiode1    COMPI COMP4 COMPI COMP4 SWCLAMP
Scounterdiode1    COUNTER2 COUNTER3 COUNTER8 0 SWCLAMP
Scounterdiode2    COUNTER5 COUNTER6 COUNTER11 0 SWCLAMP
Scounterdiode3    BUFFER1 0 COUNTER9 0 SWCLAMP
Scounterdiode4    BUFFER2 0 COUNTER10 0 SWCLAMP
Scounterdiode5    COUNTER7 HICCUPCOMPLETE COUNTER7 HICCUPCOMPLETE SWCLAMP
Scsdiode1    CS1 ILIM CS1 ILIM SWCLAMP
Scsdiode2    ILIM V5V ILIM V5V SWCLAMP
Sdd1    DELAYDRVA V5V DELAYDRVA V5V SWCLAMP
Sdd2    0 DELAYDRVA 0 DELAYDRVA SWCLAMP
Sdd3    DELAYDRVB V5V DELAYDRVB V5V SWCLAMP
Sdd4    0 DELAYDRVB 0 DELAYDRVB SWCLAMP
Sdiode_vcc1    VCC5 VCC6 VCC5 VCC6 SWCLAMP
Sissdiode1    ISR V5V ISR V5V SWCLAMP
Sresdiode1    RES V5V RES V5V SWCLAMP
Sresdiode2    0 RES 0 RES SWCLAMP
Sresdiode3    RESDISCHARGE RES2 RESDISCHARGE RES2 SWCLAMP
Sresdiode4    RES7 RES9 RES7 RES9 SWCLAMP
Sresdiode5    RES8 RES10 RES8 RES10 SWCLAMP
Sresdiode6    RES3 RES4 RES3 RES4 SWCLAMP
Sslope2    0 ISR 0 ISR SWCLAMP
Sssdiode1    SS V5V SS V5V SWCLAMP
Sssdiode2    0 SS 0 SS SWCLAMP
Ssssrdiode1    SSSR V5V_0P2 SSSR V5V_0P2 SWCLAMP
Ssssrdiode2    0 SSSR 0 SSSR SWCLAMP
Suvi1    0 UVLO 0 UVLO SWCLAMP

*DRIVER
Sdriver1   BST1 HO1  DR5 0 SdriverT
Sdriver11    BST2 HO2 DR7 0 SdriverT
Sdriver3    VCC LO1 DR6 0 SdriverT
Sdriver9   VCC LO2  DR8 0 SdriverT
Sdriver2    HO1 HS1 DR5 0 SdriverB
Sdriver12    HO2 HS2 DR7 0 SdriverB
Sdriver4   LO1 0  DR6 0 SdriverB
Sdriver10    LO2 0 DR8 0 SdriverB
Sdriver5   REF SR1  DR9 0 SdriverSRT
Sdriver7   REF SR2  DR10 0 SdriverSRT
Sdriver6   SR1 0  DR9 0 SdriverSRB
Sdriver8   SR2 0  DR10 0 SdriverSRB
```

```
*Rgiga
Rgiga1 LEB1 0 1G
Rgiga2 RAM2LEB 0 1G
Rgiga3 RAM5 0 1G
Rgiga4 RES2 0 1G
Rgiga5 CLK 0 1G
Rgiga6 SS2 0 1G
Rgiga7 SSSR2 0 1G
Rgiga8 COMPI COMP4 1G
Rgiga9 COUNTER8 0 1G
Rgiga10 COUNTER11 0 1G
Rgiga11 COUNTER9 0 1G
Rgiga12 COUNTER10 0 1G
Rgiga13 COUNTER7 HICCUPCOMPLETE 1G
Rgiga14 CS1 ILIM 1G
Rgiga15 ILIM V5V 1G
Rgiga16 DELAYDRVA V5V 1G
Rgiga17 0 DELAYDRVA 1G
Rgiga18 DELAYDRVB V5V 1G
Rgiga19 0 DELAYDRVB 1G
Rgiga20 VCC5 VCC6 1G
Rgiga21 ISR V5V 1G
Rgiga22 RES V5V 1G
Rgiga23 0 RES 1G
Rgiga24 RESDISCHARGE RES2 1G
Rgiga25 RES7 RES9 1G
Rgiga26 RES8 RES10 1G
Rgiga27 RES3 RES4 1G
Rgiga28 0 ISR 1G
Rgiga29 SS V5V 1G
Rgiga30 0 SS 1G
Rgiga31 SSSR V5V_0P2 1G
Rgiga32 0 SSSR 1G
Rgiga33 0 UVLO 1G
Rgiga34 DR5 0 1G
Rgiga35 DR7 0 1G
Rgiga36 DR6 0 1G
Rgiga37 DR8 0 1G
Rgiga38 DR9 0 1G
Rgiga39 DR10 0 1G

*Fslope IOUTSLOPE1 IOUTSLOPE ISR 0 Fslope
Fslope ISR 0 VFslope 10
VFslope IOUTSLOPE1 IOUTSLOPE 0V

*45
Ecs2        CS1 0 VALUE { if(V(CSINT)>0.75 & (V(LO1)>2 | V(LO2)>2),5,0) }
Eleb3         LEB9 0 VALUE { if(V(LO1)>2 | V(LO2)>2, 5, 0) }
```

```
Etc1        TC1 0 VALUE { if(V(RSTout)>2.5 | (V(ILIM)>0.5 | (V(PH)<=2.5 | V(MskPWM)>2.5)),5,0) }
Etc3        TC6 0 VALUE { if(V(RSTout)>2.5 | (V(ILIM)>0.5 | (V(PH)>2.5 | V(MskPWM)>2.5)),5,0)  }
Etc5        TC11 0 VALUE { if(V(RSTout)>2.5 | (V(ILIM)>0.5 | (V(PH)>2.5 | V(MskPWM)>2.5)),5,0)  }
Etc6        TC13 0 VALUE { if(V(comp2pwm)>0 & V(PH)<=2.5 & V(MskPWM)<=2.5 &
(V(delayDRVB)>2.5& V(delayDRVB)<=4.5),5,0) }
Etc7        TC16 0 VALUE { if(V(RSTout)>2.5 | (V(ILIM)>0.5 | (V(PH)<=2.5 | V(MskPWM)>2.5)),5,0)
}
Etc8        TC18 0 VALUE { if(V(comp2pwm)>0 & V(PH)>2.5 & V(MskPWM)<=2.5 &
(V(delayDRVA)>2.5& V(delayDRVA)<=4.5),5,0) }

Gdd1        0 DELAYDRVA VALUE { if((V(MskPWM)<=2.5 & V(PH)>2.5) & V(VREFUV)<=2.5,1333E-
6/V(RD1),-1333E-6/V(RD2)) }
Gdd2        0 DELAYDRVB VALUE { if((V(MskPWM)<=2.5 & V(PH)<=2.5) & V(VREFUV)<=2.5,1333E-
6/V(RD1),-1333E-6/V(RD2)) }

*subckt
.MODEL Dnom D IS=100n RS=30m CJO=10p VJ=0.5 EG=0.6
.MODEL S5K VSWITCH RON=1 ROFF=100E6 VON=1V VOFF=0.0V
.MODEL SWCLAMP VSWITCH RON=0.001 ROFF=100E6 VON=10m VOFF=0
.MODEL SdriverT VSWITCH RON=2.7 ROFF=1E6 VON=2.6V VOFF=2.4V
.MODEL SdriverB VSWITCH RON=1E6 ROFF=1.6 VON=2.6V VOFF=2.4V
.MODEL SdriverSRT VSWITCH RON=17 ROFF=1E6 VON=2.6V VOFF=2.4V
.MODEL SdriverSRB VSWITCH RON=1E6 ROFF=5 VON=2.6V VOFF=2.4V
.MODEL NOMNPN NPN RB=350 RC=600 RE=20
.ENDS LM5045

* RSFF
.SUBCKT RSFF5K R S Q NQ
Eff1 PSTATE 0 VALUE { if(V(R)>2.5 & V(S)<=2.5,0,if(V(R)<=2.5 & V(S)>2.5,5,2.5)) }
Rff1 STATE PSTATE 500
Cff1 STATE 0  9p IC=0
Eff2 PQ 0 VALUE {if(V(STATE)>=4.5,5,if(V(STATE)<=0.5,0,if(V(FFMEM)>2.5,5,0))) }
Rff2 Q PQ  500
Cff2 Q 0  12p IC=0
Eff3 PNQ 0 VALUE {if(V(STATE)>=4.5,0,if(V(STATE)<=0.5,5,if(V(FFMEM)>2.5,0,5))) }
Rff3 NQ PNQ  500
Cff3 NQ 0  12p IC=0
Sff4 V5V FFMEM Q 0 SFF
Rff4 Q 0 1G
Sff5 FFMEM 0 NQ 0 SFF
Rff5 NQ 0 1G
Cff6 FFMEM 0  3p IC=0
Vff7 V5V 0 5
.MODEL SFF VSWITCH RON=500 ROFF=100MEG VON=4.5V VOFF=0.5V
.ENDS RSFF5K
```

Appendix B. SPICE model of LM324

```
.SUBCKT LM324    1 2 3 4 5
 C1   11 12 5.544E-12
 C2    6  7 20.00E-12
 DC    5 53 DX
 DE   54  5 DX
 DLP  90 91 DX
 DLN  92 90 DX
 DP    4  3 DX
 EGND 99  0 POLY(2) (3,0) (4,0) 0 .5 .5
 FB    7 99 POLY(5) VB VC VE VLP VLN 0 15.91E6 -20E6 20E6 20E6 -20E6
 GA    6  0 11 12 125.7E-6
 GCM   0  6 10 99 7.067E-9
 IEE   3 10 DC 10.04E-6
 HLIM 90  0 VLIM 1K
 Q1   11  2 13 QX
 Q2   12  1 14 QX
 R2    6  9 100.0E3
 RC1   4 11 7.957E3
 RC2   4 12 7.957E3
 RE1  13 10 2.773E3
 RE2  14 10 2.773E3
 REE  10 99 19.92E6
 RO1   8  5 50
 RO2   7 99 50
 RP    3  4 30.31E3
 VB    9  0 DC 0
 VC 3 53 DC 2.100
 VE   54  4 DC .6
 VLIM  7  8 DC 0
 VLP  91  0 DC 40
 VLN   0 92 DC 40
.MODEL DX D(IS=800.0E-18)
.MODEL QX PNP(IS=800.0E-18 BF=250)
.ENDS
```

Appendix C. SPICE model of the transformer

```
.Subckt transformer V_IN1 V_IN2 V_OUT11 V_OUT12
*PARAMS:  Np=2 RSp=0.000103499 LIp=9.6799e-009 Ns1=3 RSs1=0.000250695 Gap = 0
L_LP NLP V_IN2 2
R_RP NRP NLP 0.000103499
L_Leak V_IN1 NRP 9.6799e-009
L_LS1 NLS1 V_OUT12 3
R_RS1 NLS1 V_OUT11 0.000250695
K_K2 L_LP L_LS1  1.0 core_model_K1
.model core_model_K1 AKO:core_model  CORE (GAP=0)
```

```
.model core_model CORE (LEVEL = 3 OD = 10.7 ID = 0 AREA = 0.831 GAP = 0 Br = 900 Bm = 4600
Hc = 0.2)
.END transformer
```

Appendix D. SPICE model of BCM62

```
.SUBCKT BCM62B 1 2 3 4
Q1 2 1 3 TR1
Q2 1 1 4 TR1
.MODEL TR1 PNP
+ IS = 2.014E-14 NF = 0.9974 ISE = 6.578E-15
+ NE = 1.45 BF = 315.3 IKF = 0.079 VAF = 39.15
+ NR = 0.9952 ISC = 1.633E-14 NC = 1.15 BR = 8.68 IKR = 0.09
+ VAR = 9.5 RB = 10 IRB = 5E-06 RBM = 5E-06 RE = 0.663 RC = 0.718
+ XTB = 0 EG = 1.11 XTI = 3 CJE = 1.135E-11 VJE = 0.7071 MJE = 0.3808
+ TF = 6.546E-10 XTF = 5.387 VTF = 6.245 ITF = 0.2108 PTF = 0
+ CJC = 6.395E-12 VJC = 0.4951 MJC = 0.44 XCJC = 0.6288
+ TR = 5.5E-08 CJS = 0 VJS = 0.75 MJS = 0.333 FC = 0.9059
.END BCM62B
```

Appendix E. SPICE model of LM5110A

```
.SUBCKT LM5110  IN_A IN_B nSHDN IN_REF VCC OUT_A OUT_B VEE
M_M3         N14549193 N14549039 OUT_B OUT_B PMOS01
R_R2        N14500477 N14500503  35
C_C9        N14549193 N14549039  30p
V_V8        N14550180 0 0.4V
V_V6        N14537650 0 0.4V
I_I1       VCC NSHDN DC 18uA
V_V1        N14529231 IN_REF 3.015V
R_R4        VCC N14500507  0.02
X_U2        N14549539 N14549349 DELAY PARAMS:  RINP=1K DELAY=18n
V_V2        N145291613 0 0.23V
C_C4        VEE OUT_A  10pF
C_C10        OUT_B N14548987  10p
R_R5        N14500679 VEE  0.02
E_E1        N14500445 OUT_A VALUE { IF(V(N14500841, 0) > 0.5, 5, -5) }
R_R3        N14548981 N14548987  40
C_C11        OUT_B VCC  10pF
E_E2        OUT_A N14500477 VALUE { IF(V(N14500841, 0) > 0.5, -5, 5) }
R_R7        VCC N14549043  0.02
R_R6        N14549013 N14549039  35
X_U9        NSHDN N14529337 N145292673 NSHDN_OUT COMPHYS_BASIC_GEN PARAMS:
+  VDD=1 VSS=0 VTHRESH=0.5
M_M1         N14500507 N14500451 OUT_A OUT_A NMOS01
X_U12        UVLO NSHDN_OUT IN_INTB N14549539 AND3_BASIC_GEN PARAMS: VDD=1
+  VSS=0 VTHRESH=500E-3
```

```
R_R8         N14549193 VEE  0.02
V_V3         N14529337 IN_REF 1.55
C_C1         N14500451 N14500507  30p
C_C7         VEE OUT_B  10pF
C_C6         OUT_A N14500503  10p
V_V4         N145292673 0 0.0825V
X_U16         UVLO NSHDN_OUT IN_INTA N14565482 AND3_BASIC_GEN PARAMS: VDD=1
+  VSS=0 VTHRESH=500E-3
M_M2         N14500679 N14500503 OUT_A OUT_A PMOS01
E_E3         N14548981 OUT_B VALUE { IF(V(N14549349, 0) > 0.5, 5, -5) }
E_E4         OUT_B N14549013 VALUE { IF(V(N14549349, 0) > 0.5, -5, 5) }
C_C2         N14500679 N14500503  30p
X_U1         N14565482 N14500841 DELAY PARAMS:  RINP=1K DELAY=18n
X_U13         IN_B N14550160 N14550180 IN_INTB COMPHYS_BASIC_GEN PARAMS: VDD=5
+  VSS=0 VTHRESH=0.5
X_U11         IN_A N14537630 N14537650 IN_INTA COMPHYS_BASIC_GEN PARAMS: VDD=5
+  VSS=0 VTHRESH=0.5
C_C12         OUT_B N14549039  10p
M_M4         N14549043 N14548987 OUT_B OUT_B NMOS01
C_C3         OUT_A N14500451  10p
R_R1         N14500445 N14500451  40
C_C8         N14548987 N14549043  30p
V_V7         N14550160 IN_REF 1.75V
V_V5         N14537630 IN_REF 1.75V
X_U8         VCC N14529231 N145291613 UVLO COMPHYS_BASIC_GEN PARAMS: VDD=1
+  VSS=0 VTHRESH=0.5
C_C5         OUT_A VCC  10pF
.ENDS LM5110
*$
.model NMOS01 NMOS
+ VTO     = 2
+ KP      = 0.66
+ LAMBDA  = 0.001
*$
.model PMOS01 PMOS
+ VTO     = -2
+ KP      = 1.1
+ LAMBDA  = 0.001
*$
.SUBCKT DELAY INP OUT PARAMS: RINP = 1k DELAY = 10n
R1 INP 101 {RINP}
C1 101 102 { 1.4427 * DELAY / RINP }
E1 102   0 OUT   0 0.5
E2 OUT   0 VALUE {IF(V(101) > 0.5, 1, 0)}
.ENDS DELAY
*$
.SUBCKT COMPHYS_BASIC_GEN INP INM HYS OUT PARAMS: VDD=1 VSS=0 VTHRESH=0.5
EIN INP1 INM1 INP INM 1
```

```
EHYS INP1 INP2 VALUE { IF( V(1) > {VTHRESH},-V(HYS),0) }
EOUT OUT 0 VALUE { IF( V(INP2)>V(INM1), {VDD} ,{VSS}) }
R1 OUT 1 1
C1 1 0 5n
RINP1 INP1 0 1K
.ENDS COMPHYS_BASIC_GEN
*$
.SUBCKT AND3_BASIC_GEN A B C Y PARAMS: VDD=1 VSS=0 VTHRESH=0.5
E_ABMGATE    YINT 0 VALUE {{IF(V(A) > {VTHRESH}  &
+ V(B) > {VTHRESH} &
+ V(C) > {VTHRESH},{VDD},{VSS})}}
RINT YINT Y 1
CINT Y 0 1n
.ENDS AND3_BASIC_GEN
```

Appendix F. SPICE model of the current sense amplifier (ZXCT1009)

```
.SUBCKT ZXCT1009F 1 2 3
*CONNECTION:
*Pins 1.Load 2.Vin 3.Iout
*
I1 4 3 4uA
R6 4 3 20E6
R1 2 4 Rmod1 1
Q1 4 5 3 LargeN
C1 5 11 3E-9
R5 11 3 10
R2 5 6 10E3
D1 6 8 Dmod
R3 7 6 1
V2 8 3 10
E1 7 3 4 9 1000
V1 10 1 100e-3
I2 9 10 100E-3
R4 9 10 Rmod2 1
.MODEL Dmod D IS=1E-15 BV=20 IBV=1E-3
.MODEL LargeN NPN IS=3.8E-16 BF=220 NK=.75 IKF=17e-3 VAF=60
+ ISE=1.8E-16 NE=1.4 BR=.7 IKR=3e-2 VAR=7 ISC=5E-12 NC=1.321 RB=300
+ RE=19.7 RC=63.4 CJC=51E-12 MJC=.42 VJC=.595 CJE=.21E-12 MJE=.33
+ VJE=.7 TF=1.5E-10 TR=6E-9 XTF=0.3 VTF=6 ITF=5E-5 XTB=1.17 XTI=5.4
+ KF=2E-13 AF=1.4
.MODEL Rmod1 RES (R=99.5 TC1=1E-3 TC2=1E-5)
.MODEL Rmod2 RES (R=1)
.ENDS ZXCT1009F
```

Appendix G. Converter build-in material list

#	Designator	Description	Comment	Quantity	Price/Unit	Total cost
1	C3, C4, C5, C6, C11, C12, C13, C62, C63, C64, C83, C84	CAP 10µF ±10% 35V X7R	10uF	12	0.15102	1.81224
2	C7, C68	CAP ALUM 1000UF 20% 100V RADIAL	1000 uF	2	1.27664	2.55328
3	C8, C14, C15, C48, C67, C72, C73	3.3µF ±10% 100V X7S Ceramic	3.3 uF	7	0.21	1.47
4	C9, C10, C18, C19, C31, C33, C35, C36, C39, C41, C42, C50, C65, C66, C70, C71, C85, C86	1000pF ±10% 16V X7R Ceramic	1nF	18	0.01012	0.18216
5	C16, C43, C47, C56	CAP CER 100PF 50V NP0 0805	100pF	4	0.00874	0.03496
6	C17, C20, C21, C27, C28, C44, C69, C74, C75, C80, C81	1µF 50V Ceramic Capacitor X7R 0805	1uF	11	0.00874	0.09614
7	C22, C45, C76	6800pF ±10% 50V X7R Ceramic Capacitor	6.8nF	3	0.0138	0.0414
8	C23, C58, C77	0.022µF ±10% 10V X7R Ceramic	0.022uF	3	0.0432	0.1296
9	C25, C79	0.047µF ±10% 10V X7R Ceramic	0.047uF	2	0.0324	0.0648
10	C26	470pF ±10% 16V X7R Ceramic Capacitor	470pF	1	0.028	0.028
11	C30, C34	680pF ±5% 50V C0G, NP0 Ceramic Capacitor	680pF	2	0.01935	0.0387
12	C32, C40, C49, C57, C59	2200pF ±10% 25V X7R Ceramic Capacitor	2.2nF	5	0.04625	0.23125
13	C46	0.22µF 100V Ceramic Capacitor X7R 0805	0.22uF	1	0.054	0.054
14	C51, C52, C53, C54	CAP CER 0.1UF 10V X7R 0805	0.1uF	4	0.0324	0.1296
15	C55	CAP CER 6.8UF 25V JB 1206	6.8uF	1	0.192	0.192
16	D1, D5, D8, D11, D21, D26, D30, D35	DIODE SCHOTTKY 150V 40A	V40PW15C	8	0.4557	3.6456
17	D2, D3, D15, D16, D22	DIODE ZENER 4.7V 200MW	DZ2J047M0L	5	0.01728	0.0864
18	D4, D50	DIODE ZENNER 12V	12V	2	0.02372	0.04744
19	D6, D12, D17, D18, D19, D20, D27, D36	DIODE SCHOTTKY 100V 1A SOD123H	SCHOTTKY 100V 1A	8	0.0961	0.7688
20	D7, D9, D10, D13, D14, D29, D31, D34, D39, D44	DIODE SCHOTTKY 20V 1A SOD123H	20V 1A	10	0.041	0.41
21	D23, D24, D25, D28, D32, D33, D37, D38, D40, D41, D42, D43	DIODE SCHOTTKY 100V 15A TO277-3	FSV15100V	12	0.28796	3.45552
22	L1, L3	FIXED IND 850NH 40A 0.87 MOHM	850nH 40A 0.87mOhm	2	1.512	3.024
23	L2	100µH Shielded Inductor 1.2A	Inductor 100uH	1	0.6	0.6
24	R1, R3, R81	1 mOhm ±1% 4W	0.001	3	0.3825	1.1475
25	R4, R83	RES SMD 56K OHM 1% 1/8W 0805	56k	2	0.0019	0.0038
26	R5, R26	RES SMD 2.2K OHM 5% 1/8W 0805	2.2k	2	0.00247	0.00494
27	R7, R12, R30, R33, R36, R37, R42, R43, R45, R54, R60, R79, R85, R90, R102, R103, R106, R107, R108	RES SMD 5% 1/8W 0805	10k	19	0.00213	0.04047

28	R9, R22, R87	RES SMD 5% 1/8W 0805	82k	3	0.0019	0.0057
29	R13, R72, R91	RES SMD 3.74K OHM 1% 1/8W 0805	3.74k	3	0.0019	0.0057
30	R14, R20, R34, R41, R92, R95, R104, R105	RES SMD 5% 1/8W 0805	10	8	0.00247	0.01976
31	R15	RES SMD 5% 1/8W 0805	8.2k	1	0.0019	0.0019
32	R16, R93	RES SMD 560 OHM 1% 1/8W 0805	560	2	0.00266	0.00532
33	R17, R94	RES SMD 560 OHM 1% 1/8W 0805	30	2	0.00266	0.00532
34	R18	RES SMD 9.76K OHM 1% 1/8W 0805	9.76k	1	0.00247	0.00247
35	R19	RES SMD 36.5K OHM 1% 1/8W 0805	36k	1	0.00266	0.00266
36	R21, R96	RES SMD 1.2K OHM 1% 1/8W 0805	1.2k	2	0.00247	0.00494
37	R25, R99	RES SMD 16.9K OHM 1% 1/8W 0805	16.9k	2	0.00266	0.00532
38	R28	RES SMD 150K OHM 5% 1/8W 0805	47k	1	0.0019	0.0019
39	R29, R101	RES SMD 27K OHM 5% 1/8W 0805	27k	2	0.0019	0.0038
40	R31, R51, R53, R58, R71, R75, R78	RES SMD 1K OHM 1% 1/8W 0805	1k 1%	7	0.00247	0.01729
41	R32, R55, R56, R70, R73, R74, R77	RES SMD 4.87K OHM 1% 1/8W 0805	4.87k	7	0.00266	0.01862
42	R35	RES SMD 4.3K OHM 1% 1/8W 0805	4.3k	1	0.00247	0.00247
43	R38, R46, R48, R49, R52, R59, R64, R66, R67, R80, R109	RES SMD 5% 1/8W 0805	1k	11	0.0019	0.0209
44	R39	RES SMD 8.66K OHM 1% 1/8W 0805	8.66k 1%	1	0.00266	0.00266
45	R40	RES SMD 15K OHM 1% 1/8W 0805	15k	1	0.00247	0.00247
46	R44	RES SMD 4.87K OHM 1% 1/8W 0805	4.87k 1%	1	0.00266	0.00266
47	R47	RES SMD 1K OHM 1% 1/8W 0805	2k 1%	1	0.00266	0.00266
48	R50, R61	RES SMD 33K OHM 5% 1/8W 0805	33k	2	0.0019	0.0038
49	R57, R65	RES SMD 6.8K OHM 5% 1/8W 0805	6.8k	2	0.0019	0.0038
50	R62, R63	RES SMD 5% 1/8W 0805	13k	2	0.0019	0.0038
51	R68	RES SMD 5% 1/8W 0805	3.3k	1	0.0019	0.0019
52	R69	RES SMD 5% 1/8W 0805	120k	1	0.0019	0.0019
53	R76	RES SMD 11K OHM 1% 1/8W 0805	11k 1%	1	0.00247	0.00247
54	R110	RES SMD 1K OHM 1% 1/8W 0805	0 Ohm	1	0.00247	0.00247
55	T1	MOSFET P-CH 40V 110A D2PAK	SUM110P04-05-E3	1	2.144	2.144
56	T2, T3, T7, T8, T17, T18, T19, T20, T27, T28, T32, T33, T38, T39, T40, T41	MOSFET N-CH 80V 100A TDSON-8	BSC057N08	16	0.532	8.512
57	T4, T10, T29	IC CURRENT MONITOR 1% SOT23-3	ZXCT1009FTA	3	0.4464	1.3392
58	T9, T12, T34	TRANS PNP 80V 0.5A SC70-3	MMSTA56-7-F	3	0.0948	0.2844
59	T11, T35	Transformer	Transformer	2	2.5	5
60	T15, T16, T22, T25, T26, T42	TRANS NPN 45V 0.1A SOT23	BC847	6	0.0164	0.0984

61	T21	TRANS PNP 45V 0.1A SOT23	BC857	1	0.0155	0.0155
62	T23, T24	IC REG LDO 5V 0.5A SOT223	UA78M05	2	0.264	0.528
63	Term1, Term2, Term3, Term4	4 pins 20A 150V Barrier Block Connector, Screws with Captive Plate	Barrier Block 4P	4	0.84548	3.38192
64	U2, U5, U18, U21	IC DVR HALF-BRIDGE HV 8-SOIC	LM5100	4	1.395	5.58
65	U3, U19	IC CTLR FULL BRIDGE PWM 28-TSSOP	LM5045MHX/NOPB	2	2	4
66	U6, U10, U15	IC OPAMP GP 1.3MHZ RRO 14SO	LMV324	3	0.0166	0.0498
67	U7	SWITCH SPST GOLD 3 SEC 50V	SWITCH SPST	1	0.42294	0.42294
68	U8, U9, U13, U14, U16	TRANS PNP DBL 45V 100MA SOT143B	BCM62B	5	0.14023	0.70115
69	U11	Microchip 8 bit microprocessor	PIC16F1769 I/SS	1	1.15	1.15
70	U12	Buck Switching Regulator Adjustable 1A 8-75V	LM5010	1	1.609	1.609
Total cost						**55.26357**

Appendix H. The design of 2-layer PCB

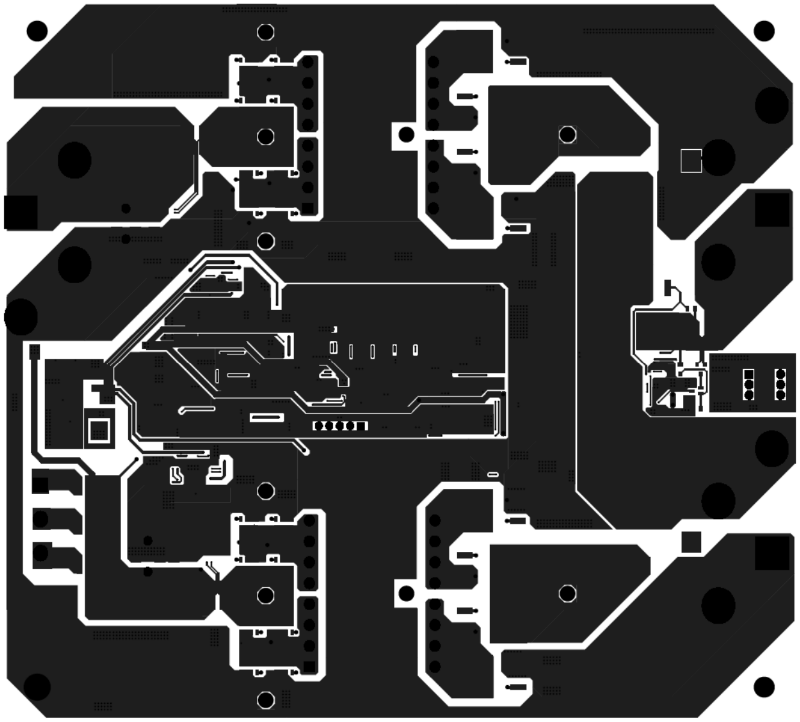

Figure 6-1. 2-layer PCB (Top copper layer)

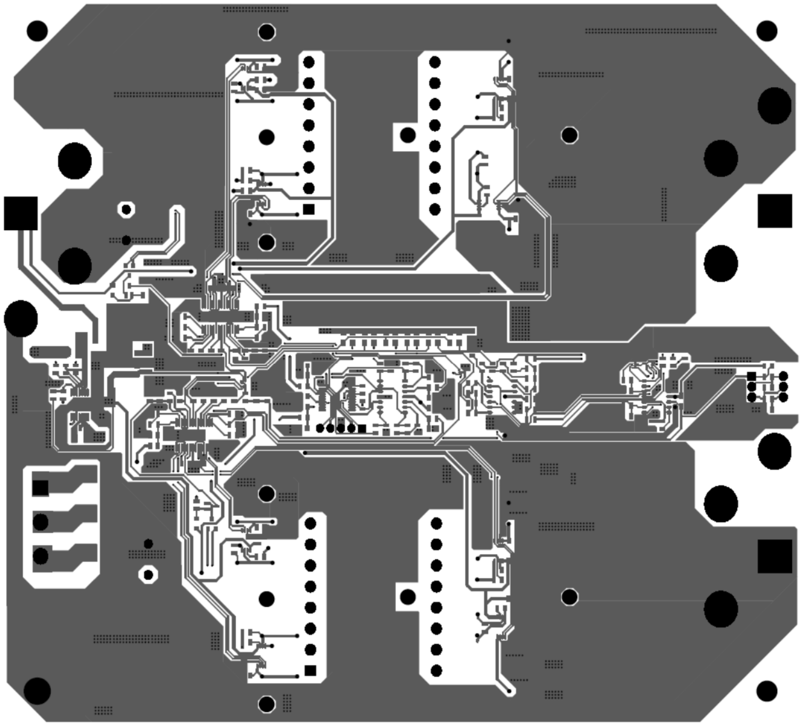

Figure 6-2. 2-layer PCB (Bottom copper layer)

Appendix I. MPPT coding for the microcontroller

```
#include "mcc_generated_files/mcc.h"
#define step = 0x02;
unsigned int PV_Outcurrent, cnt;
unsigned int TB_Outcurrent, ipv3, itb3;
unsigned int steppv, steptb, vpv0, vtb0, vpv1, vpv2, vpv3, vtb1, vtb2,
vtb3, ipv0, itb0, ipv1, ipv2, itb1, itb2, fb, startmppt;
unsigned long int Ppv0, Ppv1, Ptb0, Ptb1;

void main(void) {
    // initialize the device
    SYSTEM_Initialize();
    TMR3_Initialize();
    startmppt = 0;
    PV_Outcurrent = 0x0100;
    TB_Outcurrent = 0x0100;
    DAC1_Load10bitInputData(PV_Outcurrent);
    DAC2_Load10bitInputData(TB_Outcurrent);
    PIR4bits.TMR3IF = 0;
    TMR3H = 0x00;
    TMR3L = 0x00;
    T3CONbits.TMR3ON = 1;
    while (1) {
        if (PIR4bits.TMR3IF = 1) //measure feedback voltage every
32.768ms as timer3 over float
        {
```

```
            vpv0 = ADC_GetConversion(channel_AN3); //reading PV
voltage
            ipv0 = ADC_GetConversion(channel_AN5); //input current
from PV
            vtb0 = ADC_GetConversion(channel_AN2); //reading turbine
voltage
            itb0 = ADC_GetConversion(channel_AN4); //input current
from turbine
            Ppv0 = vpv0*ipv0; //input power from solar panel
            Ptb0 = vtb0*itb0;
            fb = ADC_GetConversion(channel_AN9); //reading feedback
voltage
            steppv = 0x01;
            steptb = 0x01;
            startmppt = 0x00;

            while (fb < 0x01FA) // check output power is lower than
input (CC&CV feedback loop @ maximum capacity) for MPPT
            {
                if (!startmppt) {
                    PV_Outcurrent = PV_Outcurrent - step;
                    TB_Outcurrent = TB_Outcurrent - step;
                    startmppt ^= 1;
                }

                if (ipv0 <= 0x0020) {
                    PV_Outcurrent = 0x01F0;
                    steppv = 0x00;
                }
                if (itb0 <= 0x0020) {
                    TB_Outcurrent = 0x01F0;
                    steptb = 0x00;
                }

                DAC1_Load10bitInputData(PV_Outcurrent); //set level
for input current from solar panel
                DAC2_Load10bitInputData(TB_Outcurrent); //set level
for input current from turbine
                cnt = 6000; //Delay 200ms (all tested at 50ms))
                while (--cnt != 0) {
                }

                vpv1 = ADC_GetConversion(channel_AN3); //reading PV
voltage
                ipv1 = ADC_GetConversion(channel_AN5); //input current
PV
                vtb1 = ADC_GetConversion(channel_AN2); //reading
turbine voltage
                itb1 = ADC_GetConversion(channel_AN4); //input current
from turbine
                //cnt = 120; //Delay 200us
                //while (--cnt != 0) {
```

```
        // }
        vpv2 = ADC_GetConversion(channel_AN3); //reading PV
voltage
        ipv2 = ADC_GetConversion(channel_AN5); //input current
PV
        vtb2 = ADC_GetConversion(channel_AN2); //reading
turbine voltage
        itb2 = ADC_GetConversion(channel_AN4); //input current
from turbine
        //cnt = 120; //Delay 200us
        //while (--cnt != 0) {
        // }
        vpv3 = ADC_GetConversion(channel_AN3); //reading PV
voltage
        ipv3 = ADC_GetConversion(channel_AN5); //input current
PV
        vtb3 = ADC_GetConversion(channel_AN2); //reading
turbine voltage
        itb3 = ADC_GetConversion(channel_AN4); //input current
from turbine

        Ppv1 = ((vpv1 * ipv1)+(vpv2 * ipv2)+(vpv3 * ipv3)) /
3; //input power from solar panel
        Ptb1 = ((vtb1 * itb1)+(vtb2 * itb2)+(vtb3 * itb3)) /
3; //input power from turbine

        if (vpv1 > 0x00FF) {
          //Tracking maximum input power for solar panel
          if (Ppv1 < Ppv0) steppv ^= 1;
          if ((steppv)&&(PV_Outcurrent > 0x0010))
PV_Outcurrent = PV_Outcurrent - step;
          if ((!steppv)&&(PV_Outcurrent < 0x03FF))
PV_Outcurrent = PV_Outcurrent + step;

        }
        if (vtb1 > 0x00AF) {
          //Tracking maximum input power for turbine
          if (Ptb1 < Ptb0) steptb ^= 1;
          if ((steptb)&&(TB_Outcurrent > 0x0010))
TB_Outcurrent = TB_Outcurrent - step;
          if ((!steptb)&&(TB_Outcurrent < 0x03FF))
TB_Outcurrent = TB_Outcurrent + step;
        }
        vpv1 = 0;
        ipv1 = 0;
        vpv2 = 0;
        ipv2 = 0;
        vpv3 = 0;
        ipv3 = 0;
        Ppv0 = Ppv1;
        vtb1 = 0;
        itb1 = 0;
```

```
                vtb2 = 0;
                itb2 = 0;
                vtb3 = 0;
                itb3 = 0;
                Ptb0 = Ptb1;
                fb = ADC_GetConversion(channel_AN9); //reading
feedback voltage

                asm("clrwdt");
            }
            // Clear the TMR3 interrupt flag
            PIR4bits.TMR3IF = 0;
            //set initial value of timer3 to count
            TMR3H = 0x00;
            TMR3L = 0x00;
            // Start the Timer3
            T3CONbits.TMR3ON = 1;
            asm("clrwdt");
        }
    }
}
```